

DYNAMICS OF ENERGY TRANSFER IN LARGE ALUMINUM  
NANOPARTICLES: SIZE AND SURFACE DEPENDENT  
PHOTORESPONSES OF SOLUTION PROCESSED PARTICLES

By  
Kenneth James Smith

A dissertation submitted to Johns Hopkins University in conformity  
with the requirements for the degree of Doctor of Philosophy

Baltimore, Maryland  
January 2020

# Abstract

Novel realizations of metal nanoparticles (NPs) are of continuing interest due to their unique optical properties and potential applications in optoelectronics, sensing, and catalysis. The unique and customizable optical properties of these particles make them ideally suited to act as light harvesters across the energy spectrum. Unlike bulk materials it is possible to modify metallic NP's absorption characteristics simply by adjusting their size, shape, and medium in which they reside. Aluminum is an inexpensive earth-abundant plasmonic material and a promising alternative to noble metals for applications requiring UV sensitivity and scalability. The plasmon resonance of bulk aluminum metal falls in the ultraviolet, but the LSPRs of aluminum NPs have been tuned successfully to the visible and NIR

In this work, time-resolved ultrafast broadband transient absorption spectroscopy has been used to study the relaxation dynamics associated with photoexcitation of plasmonic aluminum NP's. Our Lab reported the first photophysical characterization of energy-transfer dynamics in large (100 nm diameter) plasmonic aluminum nanoparticles suspended in liquid isopropanol. Using a two-interface model, we find that a rapid thermal energy transfer from particle to solvent is accounted for by the presence of a compact ~4 nm native oxide layer on the aluminum nanoparticles. Size-dependent phonon "breathing"/vibrational modes are also observed as oscillations in total cross-section. We find that both the oscillation frequency and damping rate increase as the diameter of the particles decreases. Due to their rapid cooling, these particles are expected to be rather robust and could be utilized as an effective tool to engineer heat transfer rates from large particles to the surrounding medium.

Advisor:            Dr. Arthur E. Bragg

Thesis Committee:

Dr. Paul Dagdigian

Dr. Tyrel McQueen

# Acknowledgments

First and foremost, I would like to acknowledge my PhD advisor Art Bragg for being a truly exceptional scientist and mentor. His commitment to the growth and education of his students is second to none, which is evident by his willingness to spend long hours with them in ‘the trenches’ problem solving or answering questions. He always tries to make time when a student comes to him, sometimes even to his own disadvantage. I must also acknowledge Tim Magnanelli who is another individual that will put someone else’s needs above his own. Our laser system is rather daunting when first joining the lab and Tim was always willing to spend time answering the simple questions about the laser.

Last and certainly not least I have to acknowledge my mother who passed away while I was doing my research at Johns Hopkins. She always encouraged me to find my own path and insisted that I should do anything as long as it made me happy. Without all the sacrifices she made while I was growing up, I never could have gotten where I am now.

# Table of Contents

Abstract.....	ii
Acknowledgments.....	iv
Table of Contents.....	v
List of Tables.....	vii
List of Figures.....	ix
Chapter 1: Introduction.....	1
1.0 Overview.....	1
1.1 Photocatalysis.....	2
1.2 Photophysics of Plasmonic Nanoparticles.....	5
1.3 Plasmon Enhanced Photocatalysis.....	11
1.4 Aluminum for Plasmonics.....	14
1.5 Thesis Layout.....	16
1.6 References.....	17
Chapter 2: Experimental Methods.....	20
2.0 Overview.....	20
2.1 Description of the Laser Sources.....	20
2.2 Experimental Setup.....	23
2.3 Steady State Spectroscopies.....	25
2.4 Introduction to Transient Absorption Spectroscopy.....	26
2.5 Data Acquisition and Analysis.....	29
2.6 References.....	32

Chapter 3: Dynamics of Energy Transfer in Large Plasmonic Aluminum	
Nanoparticles.....	<b>33</b>
3.0 Abstract.....	<b>33</b>
3.1 Introduction.....	<b>34</b>
3.2 Results and Discussion.....	<b>36</b>
3.3 Conclusions.....	<b>51</b>
3.4 Methods.....	<b>52</b>
3.5 References.....	<b>56</b>
Chapter 4: Size and Surface-Dependent Photoresponses of Solution-Processed	
Aluminum Nanoparticles .....	<b>62</b>
4.0 Abstract.....	<b>62</b>
4.1 Introduction.....	<b>63</b>
4.2 Results and Discussion.....	<b>67</b>
4.3 Conclusions.....	<b>79</b>
4.4 Methods.....	<b>80</b>
4.5 References.....	<b>85</b>
Chapter 5: Exciton Diffusion in Poly(thiophene-methannulene) Characterized by	
Singlet-Singlet Annihilation Method.....	<b>89</b>
5.0 Introduction.....	<b>89</b>
5.1 Experimental Methods.....	<b>93</b>
5.2 Modeling Procedure .....	<b>96</b>
5.3 Results and Discussion.....	<b>99</b>
5.4 Conclusion.....	<b>101</b>

5.5 References.....	<b>102</b>
Appendix I: Supporting Information for Chapter 3.....	<b>103</b>
Appendix II: Supporting Information for Chapter 4.....	<b>117</b>
Appendix III: Curriculum Vitae.....	<b>127</b>

# List of Tables

<b>Table 3.1:</b> Time constants obtained by fitting wavelength-dependent transients with Equation 3.1.....	<b>45</b>
<b>Table 3.2:</b> Heat capacities and thermal conductivities of aluminum, aluminum oxide and isopropanol.....	<b>49</b>
<b>Table 4.1:</b> Parameters determined from fitting the time-dependent evolution of transient absorption signals to Equation 1 and from TEM analysis ( $d$ and $\sigma_d$ ) as a function of nanoparticle size. Fitting details are explained in the text. Standard errors associated with the fitting timescales are given in Table A2.2.....	<b>74</b>
<b>Table 4.2:</b> Vibrational periods and damping times for 54 nm, 85 nm, 121 nm, and 144 nm Al NPs from TA experiments ( $\tau_p$ and $T_l$ ) and FEM simulations ( $\tau_{p.sim}$ and $T_{l.sim}$ ) including both a soft oxide layer and ligand shell.....	<b>78</b>
<b>Table 5.1:</b> Thiophene-methanoannulene structures; this chapter focuses on exciton diffusion in TI-PTMT.....	<b>90</b>
<b>Table 5.2:</b> Calculated values of initial exciton density ( $N_0$ ), photon density ( $N_{photon}$ ), and effective path length ( $l$ ).....	<b>98</b>
<b>Table 5.3:</b> Calculated diffusion constant and length for TI-PTMT from varying interaction radius and fixed exciton lifetime.....	<b>100</b>
<b>Table 5.4:</b> Values taken from the literature of the diffusion constant and diffusion length for excitons in the polymer P3HT.....	<b>100</b>
<b>Table A1.1:</b> Parameters for fits shown in Figure 3A in the text.....	<b>108</b>
<b>Table A1.2:</b> Parameters for fits shown in Figure A2.4a.....	<b>109</b>
<b>Table A1.3:</b> Oscillation period calculated from the truncated data sets 5-100 ps shown in Figure 3B in the text.....	<b>109</b>
<b>Table A2.1:</b> FTIR feature assignments.....	<b>120</b>
<b>Table A2.2:</b> $^1\text{H}$ NMR peak assignments.....	<b>123</b>
<b>Table A2.3:</b> Standard errors associated with each fitting timescale. $T_1$ was fixed to simulated value for 85 nm particles as described in the text due to sample polydispersity.....	<b>125</b>



# List of Figures

<b>Figure 1.1:</b> Comparison of reaction coordinate energetics for 1) a photocatalyst and 2) a traditional catalyst.....	2
<b>Figure 1.2:</b> Schematic of Conventional Photocatalysis via TiO <sub>2</sub> from left to right: (1) TiO <sub>2</sub> lattice in direct contact with an adsorbed target molecule (TM) before excitation. (2) Photoexcitation of the TiO <sub>2</sub> with UV light. (3) Charge transfer from CB of TiO <sub>2</sub> with reduction of the TM. (4) Charge recovery via oxidation of an electron donor.....	4
<b>Figure 1.3:</b> Schematic of plasmon oscillation for a metal sphere. A surface plasmon can be characterized as a surface charge density wave at a metal surface.	6
<b>Figure 1.4:</b> Plasmon resonance of gold nanoparticles with a 25 nm diameter results in an enhanced absorption near the plasma frequency ~520 nm.....	7
<b>Figure 1.5:</b> Schematic of the non-radiative decay pathway experienced by a solitary plasmonic nanoparticle with relative time scales.....	10
<b>Figure 1.6:</b> Simple schematic of the Schottky junction formed between a metal and n-type semiconductor. Photoexcitation of the metal NP results in a Fermi distribution of hot electrons that have been shown to have enough energy to overcome the Schottky barrier $\phi_B$ and enter the CB of TiO <sub>2</sub> .....	13
<b>Figure 2.1:</b> Simplified laser table layout schematic. One of three primary experimental setups is chosen based on the desired excitation wavelength. Purple - 3 <sup>rd</sup> harmonic UV light with a fixed wavelength of 266 nm. Green - Femtosecond OPA with variable wavelengths ranging from 290 – 2200 nm. Blue – 2 <sup>nd</sup> frequency doubling BBO with fixed wavelength of 400nm.....	25
<b>Figure 2.2:</b> Basic schematic of pump-probe spectroscopy with relevant changes in signal response and their corresponding processes. The inset on the right describes the common molecular processes that result in different signal changes and the left side shows the response of a nanoparticle.....	27
<b>Figure 2.3:</b> Example of correction of chirp introduced by white light super continuum generation.....	30

**Figure 3.1:** (A) TEM image of aluminum NPs. (B) A single aluminum particle surrounded by an oxide layer with an average thickness of 3.7 nm. (C) FDTD-calculated spatial electromagnetic field profile for a 93 nm-diameter aluminum NP at the LSPR wavelength of 393 nm (color scale in a.u.). (D) UV-Vis-NIR extinction (blue curve) of an aluminum NP solution in 2-propanol. FDTD-calculated extinction cross sections for a single bare aluminum icosahedron in a 2-propanol background (red curve) and an aluminum icosahedron with a  $3.7 \pm 0.8$  nm thick aluminum oxide shell (orange curve) in the same background. The inset shows the first derivative of measured (blue) and simulated (red/orange) extinction near the aluminum interband transition (1.5 eV)..... 38

**Figure 3.2:** (A) Contour plot of transient spectra from 420 – 790 nm and 820-1150 nm after 400 nm excitation with a fluence of  $134 \mu\text{J cm}^{-2}$ . The time axis is linear from 0-50 ps and logarithmic from 50-1450 ps. Data in the NIR region is scaled by a factor of 5 for clarity. (B) Visible (left) and NIR (right) transient spectra at selected time delays of the same data sets (no scaling applied in NIR). 39

**Figure 3.3:** (A) Time-dependent traces obtained from three different spectral regions: near the LSPR peak, (415-500 nm) (blue); off the LSPR peak in the NIR (1000-1125 nm) (gold); and in the interband transition region of metallic aluminum (825-900 nm) (red). Data from the visible region of the spectrum were scaled by a factor of 0.2 in order to display all three data sets in one plot. Fitting curves (described in the text) are displayed in black. (B) Fits to damped signal oscillations observed in the visible region at each of the excitation fluences used in this study..... 41

**Figure 3.4:** Simulations of thermal energy transport. (A) Temperature evolution relative to the initial temperature increase ( $\Delta T_0$ ) of the nanoparticle after optical excitation at the surface of a large (93 nm diameter) aluminum nanoparticle (solid blue line) and 3 nm into the surrounding isopropanol (solid red line) for the case where no oxide is included, and where a thin oxide shell layer on the nanoparticle is incorporated into the model (blue and red dotted lines). The yellow dotted line corresponds to temperature evolution in the oxide layer. (B) Temperature evolution for a small (10 nm diameter) aluminum nanoparticle without an oxide layer. The thermal decay dynamics in this case roughly match those of the larger particle with an oxide shell. .... 49

**Figure 4.1:** (a)-(d) TEM image of Al NPs with mean diameters of 54 nm, 85 nm, 121 nm and 144 nm. (e) High resolution TEM image showing both the surface oxide (thickness of  $3.3 \pm 0.3$  nm) and organic ligand shell (thickness of  $1.6 \pm 0.5$  nm) on an Al NP. (f) UV-Vis-NIR spectrophotometric extinction spectra for Al NP solutions with these four different mean diameters as indicated in the legend. 68

<b>Figure 4.2:</b> Contour plots of transient spectra (plotted in terms of change in optical density, $\Delta OD$ ) collected for particles with a) $\sim 54$ nm and b) $\sim 144$ nm diameters. Transients are plotted on a split linear-log timescale to highlight spectral evolution on timescales up to $\sim 1$ ns after excitation. The contour for the smallest particles is scaled by 0.25 for comparison.....	<b>69</b>
<b>Figure 4.3:</b> (a): Time-dependent changes in near-IR extinction (integrated 1000-1075 nm) observed for particles of each size. Fits are shown as dashed lines; fitting functions are described in the text. (b): Time-dependent signals for the same samples plotted on timescales relevant to thermal energy transfer to solvent.....	<b>71</b>
<b>Figure 4.4:</b> (a) Vibrational oscillation periods and (b) damping times calculated for icosahedral Al NPs of different sizes via finite element method simulations. The solid circles, rhombuses, squares, triangles and open circles represent pure Al particles, particles with a 4 nm thick crystalline oxide shell, particles with a soft (reduced Young's modulus) oxide shell, particles with a 1.3 nm oleic acid shell layer, and experimental results from TA measurements, respectively. The stars represent the combined simulation results for particles with both a soft oxide shell and an oleic acid ligand layer. The inset of (a) is a calculation of the displacement of the fundamental radial mode for a 144 nm icosahedral Al NP with a 4 nm crystalline oxide shell.....	<b>77</b>
<b>Figure 4.5:</b> Normalized calculated temperature evolutions relative to the initial temperature increase at both the outer edge of the aluminum cores and 3 nm into the surrounding solvent (IPA) of core-shell Al/Al <sub>2</sub> O <sub>3</sub> NPs with sizes ranging from 54 nm to 144 nm in diameter. An oxide shell layer of 4 nm in thickness is included in the simulation.....	<b>79</b>
<b>Figure 5.1:</b> (a) displays the thickness in nm of a film subsection. (b) Values found for the real and imaginary parts of the refractive index. (c) Absorption coefficient as a function of energy (eV).....	<b>93</b>
<b>Figure 5.2:</b> Schematic diagram of method used to find the beam width for calculation of the laser fluence.....	<b>95</b>
<b>Figure 5.3:</b> Kinetic Traces of Exiton Decay in a PTMT film.....	<b>99</b>
<b>Figure A1.1:</b> TEM images of aluminum NPs in (A), (B) and Figure 3.1A, were used to obtain the histogram (C) of the synthesized aluminum nanoparticle size. This analysis yields a size distribution with an average particle diameter of $98 \pm 12$ nm. (D) FDTD-calculated spatial electromagnetic field profile for a 93 nm-diameter aluminum NP at the quadrupole resonance wavelength of 269 nm	<b>103</b>

<b>Figure A1.2:</b> TEM images of aluminum nanoparticles before (A) and after (B) prolonged exposure to a 400 nm excitation source show no observable changes in nanoparticle morphology.....	<b>104</b>
<b>Figure A1.3:</b> Fluence dependent transient absorption data conducted at 101 $\mu\text{J cm}^{-2}$ (Top), 64 $\mu\text{J cm}^{-2}$ (Middle), and 34 $\mu\text{J cm}^{-2}$ (Bottom). Similar spectral responses were observed at all fluences with intensity having linear dependence on pump fluence Shown in Figure A1.4B.....	<b>105</b>
<b>Figure A1.4:</b> (A) Time-dependent traces (415-500 nm) at different pump fluences ranging from 134 $\mu\text{J cm}^{-2}$ (red) to 34 $\mu\text{J cm}^{-2}$ (yellow); fitting models described in the text are overlaid as dashed black lines. (B) Fluence dependence of max positive and negative extinction obtained in TAS measurements; fit reveals closely linear relationship between signal and fluence (slope – 1.29, see main text) .....	<b>106</b>
<b>Figure A1.5:</b> FDTD simulations of (top) absorption and (bottom) scattering cross sections of Al nanoparticle in IPA at different refractive indices (and corresponding dielectric constants). These comparisons reveal that the scattering contribution dominates absorption by an order of magnitude in most regions. Furthermore, local solvent heating (which generally induces reduction in refractive index and dielectric constants) can be expected to result in a net negative change in spectral scattering profile.....	<b>107</b>
<b>Figure A1.6:</b> Crude isolation of interband bleach contribution. (Top) Linear trend lines were calculated for NIR spectra obtained at each delay using points at 1000 nm and 1100 nm. The value of the trend line at the wavelength where the bleach maximum occurred (869 nm) was subtracted from measured value at this wavelength. The difference is plotted in the bottom panel. Although this method is a crude approximation for the shape of the scattering contributions in this wavelength range, this analysis shows that the interband transition recovers roughly on the timescale of thermal energy transport.....	<b>110</b>
<b>Figure A1.7:</b> Normalized calculated temperature evolutions at the surface of varying sizes of aluminum nanoparticles (10 nm to 100 nm in diameter) and 3 nm into the surrounding medium: (Top) without the presence of an oxide layer, and (Bottom) with the presence of an oxide layer.....	<b>112</b>

<b>Figure A1.8:</b> Temperature evolution time constant ( $1/e$ ) 3 nm into the solvent medium as a function of oxide thickness in the case of: (a) constant total nanoparticle size (the metal core diameter decreases with increasing oxide thickness) and (b) constant metal core size (the total size of the nanoparticle increases with increasing oxide thickness). Associated spectra for (a) and (b) are plotted in (c) and (d), respectively. Solid lines are for temperature evolution in the particles, and dashed lines are for temperature evolution in the solvent medium. The blue, orange, yellow, purple, green, cyan, and red spectra correspond to 0, 0.5 nm, 3.5 nm, 6.5 nm, 9.5 nm, 12.5 nm, and 15.5 nm oxide thicknesses respectively. These results indicate that changing the size of the aluminum metal core has a much greater influence on thermal energy transfer to the medium than changing the oxide thickness itself beyond a drastic decrease in the time constant after introduction of an oxide layer.....	113
<b>Figure A1.9:</b> Solvent coherences during the pump-probe overlap were used to determine the instrument response function. The inset displays the calculated IRF Gaussian obtained by fitting the solvent coherences at time zero. The full width half max was calculated to be 262 fs.....	115
<b>Figure A2.1:</b> Histograms of aluminum nanoparticle (Al NP) diameters based on analysis of transmission electron microscope images of different NP ensembles. The particles have average diameters of (a) $54 \pm 11$ nm, (b) $85 \pm 21$ nm, (c) $121 \pm 8.4$ nm, and (d) $144 \pm 4.3$ nm (d).....	117
<b>Figure A2.2:</b> (a)-(f) Additional high-resolution transmission electron microscopy (HRTEM) images of Al NPs. The oxide and organic ligand shells are visible in all images, although their thickness is obscured by faceting in (a)-(c). A thickness measurement is displayed in (f).....	118
<b>Figure A2.3:</b> X-ray photoelectron spectroscopy (XPS) measurements of (a) the $Al^0$ 2p and $Al^{3+}$ 2p states before and after argon sputtering of the surface as indicated in the legend and (b) the C 1s region (red) of the Al NPs prior to sputtering and fits (yellow, green, blue) as indicated in the legend. The presence of the $Al^{3+}$ 2p peak in the XPS spectrum indicates the presence of an oxide shell on the Al NPs, and the thickness of the shell was determined to be $3.1 \pm 10\%$ nm as described in the text below. The intensity ratio between the carboxylate-associated shoulder in (b) and the aliphatic C 1s feature is consistent with surface-bound oleate.....	118
<b>Figure A2.4.</b> FTIR spectra of free oleic acid (blue) and oleic-acid-capped aluminum nanoparticles (pink) cast from IPA, multiplied by 5 and offset for comparison of vibrational features.....	120

<b>Figure A2.5:</b> Full $^1\text{H}$ NMR of (a) aluminum nanoparticles capped with oleate ligand and (b) free oleic acid with peak assignments (c.f. Figure A2.6 (a)) .....	<b>121</b>
<b>Figure A2.6:</b> (a) Structure of oleic acid with $^1\text{H}$ peak assignments and (b, c, d) highlighted regions of aluminum nanoparticle and free oleic acid $^1\text{H}$ NMR spectra.....	<b>122</b>
<b>Figure A2.7.</b> Thermogravimetric analysis (TGA) of oleate bound to Al nanoparticle surfaces used to determine surface coverage of $\sim 5$ oleate ligands per $\text{nm}^2$ . See text for details.....	<b>124</b>
<b>Figure A2.8.</b> (a) Vibrational periods and (b) damping times calculated using finite element methods for single Al NPs with diameters of 54 nm (red), 85 nm (yellow), 121 nm (green), and 144 nm (blue) as a function of the Young's modulus of a 4 nm oxide shell layer which is varied between 50 GPa and 269 GPa.....	<b>124</b>

# Chapter 1

## Introduction

### 1.0 OVERVIEW

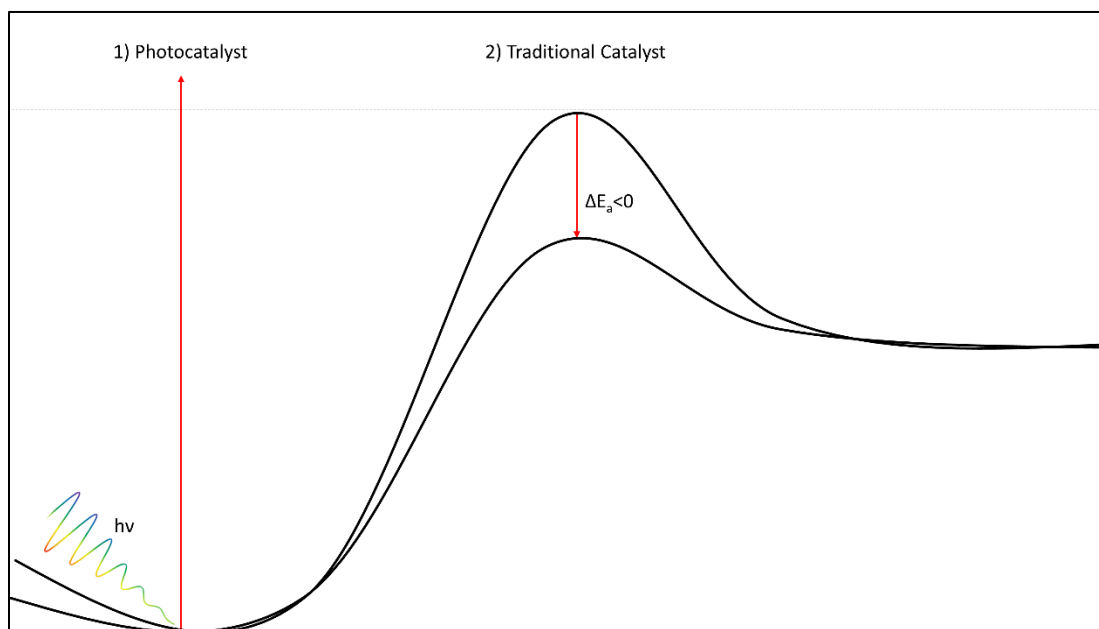
In order to reduce demand for petrochemical energy sources (oil, coal, gas, etc.) that produce CO<sub>2</sub>, a greenhouse gas, a great deal of effort has been put forth to develop “green” sources of energy. One of the prevailing fields is the development of photocatalytic materials that harness solar radiation to provide the energy needed to produce H<sub>2</sub> and O<sub>2</sub> gas from the dissociation of water.<sup>1</sup> Another, perhaps more direct approach, to reducing energy demand is through the use of photocatalysts in large scale production of common chemicals or chemical precursors.<sup>2-5</sup> Use of catalysts in this capacity would be geared towards reducing reliance on traditional energy sources, rather than replacing them. As of 2009 the chemical industry accounted for 6% of the total energy demand in the US.<sup>6</sup> Reduction in the industries’ energy demand through the development of efficient photocatalysts composed of earth abundant materials capable of producing chemicals utilizing solar radiation is of great interest.

A fundamental understanding of the photophysical properties of materials that will be used in these processes is essential for their development. One attractive option is the enhancement of photocatalytic efficiency by utilizing plasmonic nanoparticles as visible light harvesters that have enough energy to inject electrons into the conduction band (CB) of a semiconductor. While this has been shown in TiO<sub>2</sub> decorated with gold nanoparticles,<sup>7</sup>

the main focus of this thesis is to study the properties of nanoparticles made with earth-abundant aluminum in order to assess their feasibility as a gold replacement. Transient absorption spectroscopy (TAS) is a powerful tool that can elucidate the energy-transfer dynamics of excited or “hot” particles after photoexcitation.

## 1.1 PHOTOCATALYSIS

A traditional catalyst functions by lowering the activation energy necessary for a chemical reaction or process while a photocatalyst actually harnesses the energy of light to increase the energy in a system to overcome the reaction barrier. While these processes are very similar it is important to draw a distinction between the two. Figure 1.1 illustrates the difference between a traditional catalyst and a photocatalyst.

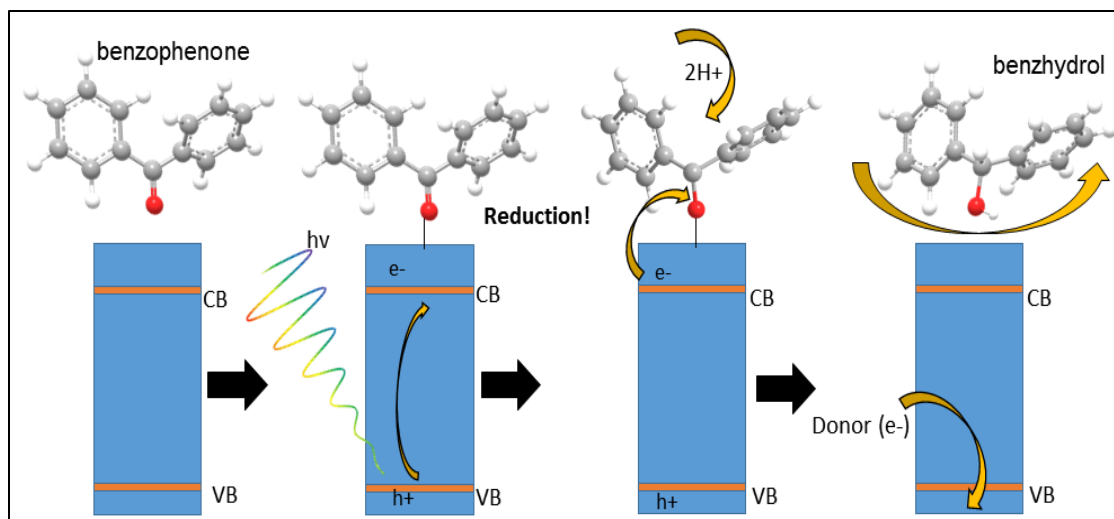


**Figure 1.1:** Comparison of reaction coordinate energetics for 1) a photocatalyst and 2) a traditional catalyst.

The process of photocatalysis can be loosely defined as the acceleration or



facilitation of a chemical reaction in the presence of some photo-activated catalytic substance. Materials capable of this for heterogeneous photocatalysis are almost exclusively semiconductors such as  $\text{TiO}_2$ .<sup>8</sup> A photocatalytic reaction cycle, involves several steps beginning with the initial absorption of a photon or photons by the semiconductor, in which case valence band (VB) electrons are promoted to the conduction band via absorption of incident photon(s). Ostensibly, after excitation there is a sufficient lifetime on the order of nanoseconds<sup>9</sup>, for the electron-hole pair to facilitate a redox reaction with a molecule adsorbed to the substrate.<sup>10</sup> Finally, the cycle must be completed by replenishing the supply of electrons in the catalyst lost in the reaction, typically through a coupled redox reaction. The efficiency of this reaction will be controlled by a number of factors, and an ideal catalyst possesses the following traits: (1) the ability to convert absorbed photons into electron-hole pairs across a broad region of the solar spectrum, in order to make use of as much solar energy as possible. (2) Allow for the separation of the electron-hole pairs and facilitate their transport to the surface of the material where redox reactions may occur. (3) The surface electronic structure should make each half reaction thermodynamically favorable, that is, in an *ideal* situation the product of each half reaction will have a lower free energy than the adsorbed/reactant state. (4) The system must be capable of continually regenerating electrons lost in the redox reaction with the target molecule (TM). Most commonly materials are hampered by low photocatalytic activity or low response to solar radiation,<sup>11</sup> making large-scale deployment impractical.



**Figure 1.2:** Schematic of Conventional Photocatalysis via TiO<sub>2</sub> from left to right: (1) TiO<sub>2</sub> lattice in direct contact with an adsorbed target molecule (TM) before excitation. (2) Photoexcitation of the TiO<sub>2</sub> with UV light. (3) Charge transfer from CB of TiO<sub>2</sub>, with reduction of the TM. (4) Charge recovery via oxidation of an electron donor.

Since the seminal paper by Fujishima and Honda<sup>1</sup> in 1972 demonstrating titania's (TiO<sub>2</sub>) ability to split water, it has become the gold standard for catalysis. This is due to its low toxicity, thermal stability, and because it is inert to the presence of most acids, alkalis and solvents.<sup>12</sup> The importance of its high stability in aqueous solution under UV irradiation cannot be overstated. When the conduction band energy ( $E_{CB}$ ) is higher than the evolution potential for a given reaction, photo-generated electrons can reduce the target molecule (TM) to product. Given that the band gap energy in TiO<sub>2</sub> is  $\Delta E_{bg} = 3.2$  eV this only allows for the direct promotion of electrons to the CB via absorption of UV photons with  $\lambda \leq 387.5$  nm. However, the amount of UV light (280-400 nm) that reaches the earth's surface is only approximately 8% of the total solar irradiance on the earth's surface.<sup>13</sup> From this information it would seem that TiO<sub>2</sub> is a poor choice as a catalyst. Indeed, the large bandgap in titania has proved to be a major obstacle however many SC's with smaller bandgaps have been investigated and were found to corrode in aqueous electrolytes under

irradiation, as well as have photo-generated holes oxidize the semiconductor itself.<sup>11</sup>

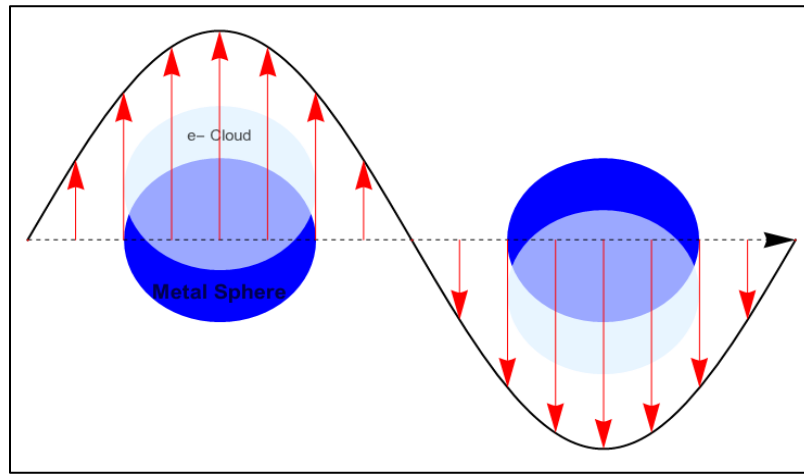
Thanks to its durability and low environmental impact, TiO<sub>2</sub> remains a leading candidate as a potential photocatalyst; with the focus turning to the development of methods to inject electrons photoexcited by visible light photons, which account for 40% of the solar constant,<sup>12</sup> into the CB of TiO<sub>2</sub>. This idea was first pursued through the creation of dye sensitized solar cells (DSSC) the first of which was created in 1991.<sup>14</sup> Recent DSSC's have achieved efficiencies<sup>15</sup> of ~15% however the primary limitation of these devices is the need for a liquid phase electrolyte which can cause significant engineering complications such as temperature sensitivity as well as structural integrity. Additionally, the most efficient cells have utilized a prohibitively expensive design incorporating ruthenium and platinum. One possible avenue that is relatively new involves coupling traditional semiconductor photocatalysts such as titania with plasmonic nanoparticles serving as visible-light sensitizers.

## **1.2 PHOTOPHYSICS OF PLASMONIC NANOPARTICLES**

### ***1.2.1 What is Localized Surface Plasmon Resonance (LSPR)?***

Colloidal gold NP's are responsible for the red color seen in stained glass windows that have been made for centuries. The reason for the coloration wasn't known until Michael Faraday published a paper outlining how gold and other metals interact with light.<sup>16</sup> In 1908 Gustav Mie presented a solution to Maxwell's equations that describes extinction spectra of spherical particles. The Mie solution remains central to the study of plasmonic materials due to the fact that it is a simple, exact solution to Maxwell's equations that can be applied to particles. When metal surfaces and small particles are irradiated by

light that is resonant with the plasma frequency of conduction electrons near the surface, the oscillating electromagnetic field of the incident radiation causes a perturbation in the electrons. Coulombic attraction to the positive atomic nuclei acts as a restoring force, inducing an oscillation of the free electrons illustrated in Figure 1.3. This depicts only a dipolar interaction however higher order, multipolar oscillations, do occur when the size of the NP is on the order of the exciting wavelength.



**Figure 1.3:** Schematic of plasmon oscillation for a metal sphere. A surface plasmon can be characterized as a surface charge density wave at a metal surface.

The plasma oscillation frequency ( $\omega_p$ ) can be calculated from Equation 1.1 and is dependent on four factors: the density of electrons ( $n_e$ ), the effective electron mass ( $m_e$ ) which is dependent on the band structure in a periodic medium, the dielectric constant of the surrounding medium ( $\epsilon_0$ ), in the example below the permittivity of free space is used for simplicity.

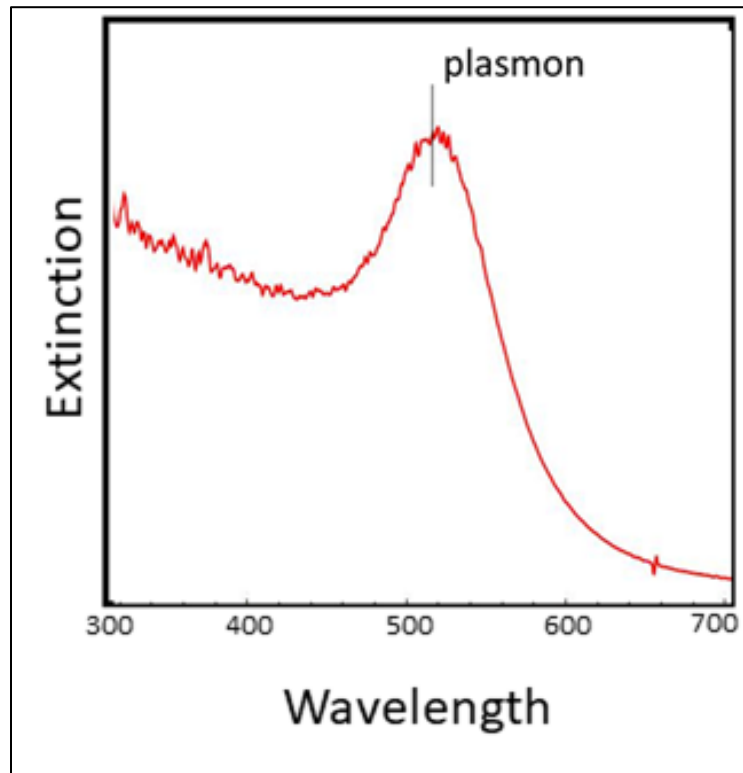
$$\omega_p = \sqrt{\frac{n_e e^2}{m_e \epsilon_0}} \quad 1.1$$

The above equation holds true for non-thermally excited electrons where the particle mass is assumed to be infinite. When incident radiation resonant with the plasma frequency

interacts with the particle a local surface plasmon resonance (LSPR) is induced. In order to relate the plasmon frequency to the dielectric constant of the medium, it must be assumed that the wavelength on incident light is much greater than the length or diameter of the particle, this is referred to as the quasistatic approximation. In this regime the electric field of the light can be assumed to be constant throughout the particle, allowing for an electrostatic as opposed to electrodynamic model to be used.<sup>17</sup>

### 1.2.2 Absorption Characteristics

The effect of a surface plasmon can be observed in steady state absorption spectra



**Figure 1.4:** Plasmon resonance of gold nanoparticles with a 25 nm diameter results in an enhanced absorption near the plasma frequency ~520nm

as a strong absorption peak centered about the resonant frequency (Figure 1.4).

One of the most notable traits that is common to all metallic LSPR's is the influence that the physical characteristics: size, shape, and composition as well as the dielectric of the surrounding environment, have on the resonant plasma frequency. The dipole approximation works well for nanoparticles that are very small compared to the exciting wavelength ( $\lambda \gg 2R$ ), which is the case for the absorption spectra of 25 nm gold particles shown in Figure 1.2.2. When the particle is too large light is no longer capable of polarizing the particle homogeneously at which point higher order multipolar modes with lower energy become increasingly dominant.<sup>18</sup> Eventually the plasmon resonance becomes explicitly dependent on particle size and these higher order modes with lower resonant energies causing the absorption peak to red shift with increasing particle size proportional to  $1/R$ .<sup>18,19</sup>

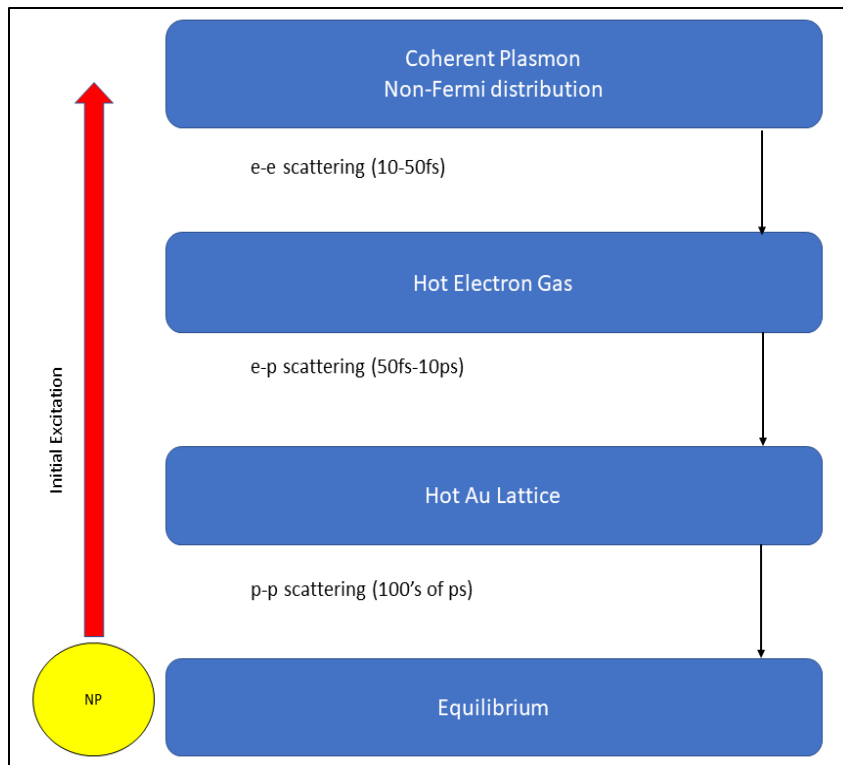
Shape effects are also very pronounced in the optical absorption spectra. The plasmon band splits into 2 distinct bands for cylindrical gold nanorods, where each band corresponds to the oscillation of electrons along the vertical and principle axes. The band at lower energies represents the electron oscillation along the principle axis and is referred to as longitudinal plasmon absorption. As the aspect ratio increases, the energy separation between the resonance frequencies of the two plasmon bands increases.<sup>18,19</sup>

The effect of local environment has been studied previously. When an Ag sphere 10 nm in diameter is engulfed by a mica shell the LSPR wavelength is seen to shift dramatically to the red.<sup>17</sup> This arises from the plasma frequency being inversely proportional to dielectric permittivity shown in Equation 1.1. By tuning the particles to have specific shapes and sizes that have a broad absorption across the solar spectrum and

manipulating their interactions with the local environment it's thought that plasmonic nanomaterials have great potential application in the production of composite photocatalysts that capture more solar radiation, thereby increasing their efficiency.

### ***1.2.3 Photophysical response to optical excitation***

The relaxation dynamics of a photoexcited “hot” particle can be well described by three processes. Electrons are initially excited to a non-Fermi distribution with the excess energy quickly thermalizing through electron-electron (e-e) scattering which occurs within 100 fs. This is followed by electron-phonon scattering (e-ph), where energy is deposited into the lattice within 1-10 ps. Last, the heat is slowly dissipated to the surroundings through phonon-phonon (ph-ph) interactions occurring on the 100s of picoseconds timescale<sup>19</sup> (Figure 1.5).



**Figure 1.5:** Schematic of the non-radiative decay pathway experienced by a solitary plasmonic nanoparticle with relative time scales.

Immediately following excitation of electrons in a plasmonic particles there exists a coherent non-Fermi distribution of electron energies that match the gaussian profile of the laser pulse. This coherence is lost very quickly on the order of femtoseconds and is difficult to observe directly in the time domain. Eventually the electrons thermalize into a hot electron gas with a Fermi distribution of energies via e-e scattering occurring within 10-100 fs.

A phenomenological two-temperature model<sup>20</sup> (TTM) is commonly used to treat thermal energy transfer from electrons to the nuclear lattice in metals (Equations 1.2 & 1.3). The electron phonon coupling relaxation time depends on the laser excitation fluence and is usually on the order of a few picoseconds.



$$C_e(T_e) \frac{dT_e}{dt} = -g(T_e - T_l) \quad 1.2$$

$$C_l \frac{dT_l}{dt} = g(T_e - T_l) \quad 1.3$$

The model is comprised of coupled differential equations where  $T_e$  and  $T_l$  are the electronic and lattice temperatures, respectively,  $C_e(T_e)$  and  $C_l$  are the specific heats and  $g$  is the electron-phonon coupling constants. The rate constant for the energy transfer scales inversely with the electronic temperature resulting in a nonexponential rise in the lattice temperature.

Finally lattice phonons (ph-ph scattering) disperse the energy into the surrounding medium which occurs within a few hundred picoseconds. This relaxation timescale has been found to be proportional to the square of the particle radius,<sup>21</sup> but more interesting is the dependence this timescale has on the surrounding medium. Recovery times become slower when thermal conductivity of the medium is decreased or if thermal contact with the medium is decreased,<sup>22,23</sup> which shows that the surrounding medium has a profound impact on the cooling dynamics of these particles. Additionally, acoustic breathing modes have been observed in previous femtosecond pump-probe studies with comparable timescales.<sup>24-27</sup> The fast heating of the particle lattice causes thermal expansion and can be accurately modeled with a damped harmonic oscillator.

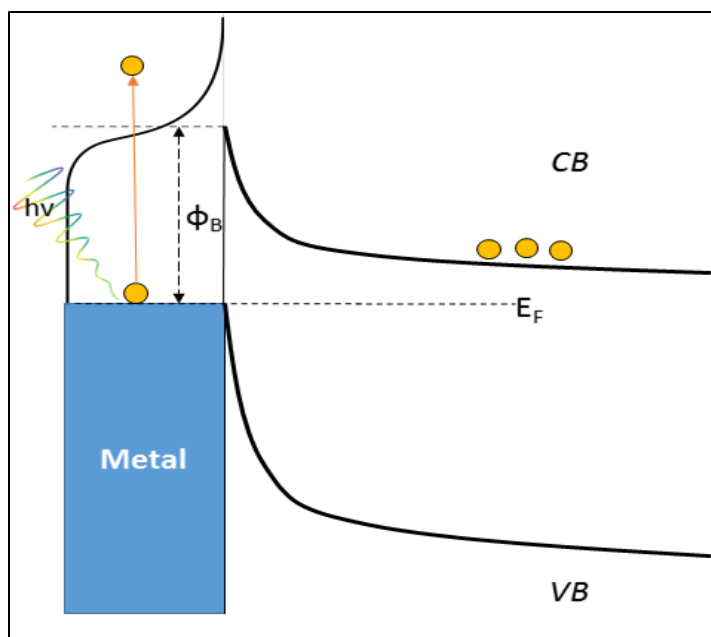
### 1.3 PLASMON ENHANCED PHOTOCATALYSIS

Under ordinary circumstances it should be impossible for an electron generated from a visible photon to have enough energy to access the CB of  $\text{TiO}_2$ .<sup>3</sup> However it has been

found that upon absorption of resonant photons an LSPR generates hot electron-hole pairs with an elevated effective temperature, during nonradiative decay.<sup>29,30</sup> The term “hot electron” is used to refer to an electron that possesses energy greater than those of thermal excitations at ambient conditions and is characterized by an elevated effective electron temperature. By employing plasmonic materials as visible light harvesters to increase the optical absorption range of photocatalysts, plasmon-enhanced photocatalysis has emerged as a possible avenue for the production of highly efficient photocatalysts.<sup>3,8,31,32</sup> Having metal NP's in contact with the semiconductor substrate results in an increased photoreactivity of TiO<sub>2</sub> and other semiconductors, subsequently increasing their efficiencies.<sup>30,33</sup>

When a metal and n-type semiconductor are brought into contact they form a Schottky junction.<sup>34</sup> In order to increase the harvesting efficiency of the semiconductor is it important that a junction is formed between the NP and SC, as a poor contact will inhibit the electrons' ability to enter the CB. Once in contact, the Fermi level throughout the whole solid must be continuous at equilibrium which results in the bending of the CB and VB.<sup>34</sup> Figure 1.6 depicts a Schottky junction with a Fermi distribution of hot electron where some have energy above  $\phi_B$ , the Schottky barrier height. Indeed it has been shown that surface plasmons in Au and Ag can transfer energies between 1 eV and 4 eV to hot electrons.<sup>3,30</sup> This type of interaction is especially favorable in the case of TiO<sub>2</sub> due to its high density of states (DOS) in the CB, which allows it to readily accept electrons.<sup>35</sup> The transfer of electrons into the CB is a means by which the number of electrons that can participate in chemical reactions is increased. After the successful electron injection to the TiO<sub>2</sub> the metal particle will be left with a positive charge. As such a ‘complete’ photocatalytic

system must include an electron donor solution or a hole transporting material in order to maintain charge balance (Figure 1.3.1).



**Figure 1.6:** Simple schematic of the Schottky junction formed between a metal and n-type semiconductor. Photoexcitation of the metal NP results in a Fermi distribution of hot electrons that have been shown to have enough energy to overcome the Schottky barrier  $\phi_B$  and enter the CB of  $TiO_2$ .

Previous studies on charge transfer dynamics in Au-TiO<sub>2</sub> composite systems have measured the timescales of hot-electron creation, injection and recombination.<sup>36,37</sup> Furube and Du's group used ultrafast transient absorption spectroscopy with visible pump and infrared probe pulses in order to characterize charge-transfer kinetics. The LSPR was selectively excited using 550 nm light, with a 150 fs pulse duration, while the transient absorption of conduction-band electrons in TiO<sub>2</sub> was measured at 3500 nm in order to directly observe injected electrons. Their results revealed that hot electron generation and injection occurred in under 50 fs with the relaxation of non-Fermi electrons occurring within 100 fs through electron-electron (e-e) scattering, similar to what is observed for

isolated particles as discussed in Figure 1.6.

Comparing these dynamics with that of the ruthenium dye N3 coupled to TiO<sub>2</sub>, they found that electron injection efficiency was approximately 40% when excited at 550 nm, which corresponds to the observed maximum of the plasmon. Surprisingly this represented a minimum in the percentage of electrons transferred between the wavelengths of 400 nm and 700 nm. In subsequent studies they found a relationship between excitation wavelength and injection efficiency, with a maximum of 100% occurring at 480 nm. Interestingly they also found that at 600 nm the injection efficiency rose to 80%. This bimodal behavior indicates that there are 2 possible injection pathways. The authors attributed the higher energy pathway to interband transition in the gold from the *d* to the *sp* band, making an electron-hole pair. Since interband transitions are not expected at 600 nm, it stands to reason that the electron-hole pair formed in this pathway must be entirely due to the hot electrons formed in the plasmon.

#### **1.4 ALUMINUM FOR PLASMONICS**

Nanoparticles composed of noble metals (Au, Ag, Cu) present a very attractive option when studying plasmons, as they are very easy to synthesize, manipulate and functionalize. However, any large-scale implementation of these materials into commercial photocatalytic systems would be prohibitively expensive. Aluminum possesses a plasmon that has a tunable range that is wider than that of Au or Ag in certain circumstances,<sup>38</sup> and has been proposed as a possible alternative to the use of noble metals. Furthermore, Al is earth abundant, making it more attractive from a financial standpoint. Unfortunately, thus far the experimental optical response of Al NPs has not matched with relative calculated spectra obtained using Finite Difference Time Domain (FDTD)

calculations.<sup>39,40</sup> These discrepancies can be attributed to oxidation of aluminum during the deposition process. In order to attain reproducible results, extreme care must be taken to ensure contaminants don't extend into the bulk of the particle.<sup>38</sup> Very little research has been conducted on the prospect of coupling Al NPs with TiO<sub>2</sub> or other materials in order to produce a plasmon enhanced photocatalyst.

Unlike gold, aluminum materials are readily oxidized under ambient conditions. As such, they require additional modification in order to be utilized. Recently, high purity aluminum nanocrystals were synthesized in a variety of shapes (monodisperse, icosahedral, trigonal bipyramidal) and sizes (70-220 nm) that are air-stable for weeks due to the formation of a 2-4 nm passivating metal oxide layer on the surface.<sup>41</sup> Addition of an alumina capping layer, which is an insulator with a bandgap of ~9 eV,<sup>41</sup> will have a large influence on the carrier density of free electrons at or around the Al/Al<sub>2</sub>O<sub>3</sub> interface. Invariably this will influence the aluminum LSPR frequency, rates of charge recombination, phonon-phonon thermalization timescales as well as the efficiency with which hot-electrons may be injected into the TiO<sub>2</sub> lattice.

The photothermal properties of these particles are poorly understood currently and will play a pivotal role in energy relaxation/transfer pathways. While characterization of the charge separation dynamics in particles that have 2 interfacial barriers, and how morphological alterations effect electron injection efficiencies is imperative for the design of photocatalysts, it is also important to understand how these particles will respond to an excess of thermal energy. Even if there is a high charge injection efficiency much of the absorbed energy must still dissipate via thermalization. Finding the thermalization timescales of aluminum particles will provide valuable insight into what effects the oxide

layer has on energy transfer from the particles to the oxide layer as well as from the oxide layer to the surrounding medium.  $\text{Al}_2\text{O}_3$  possesses vastly different thermal properties than that of aluminum metal and this additional interface will impact energy transfer timescales and efficiencies. It is well known that bare metal particles will melt or disintegrate from exposure to laser excitation given high enough intensities. An oxide shell that facilitates very fast thermalization may indicate that these particles are robust and resistant to degradation caused by the absorption of additional energy.

## **1.5 THESIS LAYOUT**

This thesis will cover the work done over the past 6 years of research. Chapter 2 will cover all of the experimental techniques used to conduct the research of this thesis as well as offer a detailed fundamental description of the laser system used in all experiments. Chapter 3 will cover our seminal paper published about solution phase aluminum nanoparticles and their photothermal relaxation properties. Chapter 4 will expand upon the work done with aluminum interrogating the changes in relaxation dynamics observed by altering the particle size. The 5<sup>th</sup> and final chapter will discuss the work done to characterize exciton diffusion in the conjugated polymer PTMT using the singlet-singlet annihilation (SSA) method.

## 1.6 REFERENCES

- (1) Fujishima, A.; Honda, K. Electrochemical Photolysis of Water at a Semiconductor Electrode. *Nature* **1972**, *238*, 37–38.
- (2) Abbott, D. Keeping the Energy Debate Clean: How Do We Supply the World's Energy Needs? *Proc. IEEE* **2010**, *98* (1), 42–66.  
<https://doi.org/10.1109/JPROC.2009.2035162>.
- (3) Clavero, C. Plasmon-Induced Hot-Electron Generation at Nanoparticle/Metal-Oxide Interfaces for Photovoltaic and Photocatalytic Devices. *Nat. Photonics* **2014**, *8* (2), 95–103. <https://doi.org/10.1038/nphoton.2013.238>.
- (4) Yoon, T. P.; Ischay, M. A.; Du, J. Visible Light Photocatalysis as a Greener Approach to Photochemical Synthesis. *Nat. Chem.* **2010**, *2* (7), 527–532.  
<https://doi.org/10.1038/nchem.687>.
- (5) Schultz, D. M.; Yoon, T. P. Solar Synthesis: Prospects in Visible Light Photocatalysis. *Science* **2014**, *343* (6174), 1239176–1239176.  
<https://doi.org/10.1126/science.1239176>.
- (6) Pratt, J.; Banholzer, W. *Improving Energy Efficiency in the Chemical Industry*; LBNL-2413E, 971846; 2009; p LBNL-2413E, 971846. <https://doi.org/10.2172/971846>.
- (7) Furube, A.; Du, L.; Hara, K.; Katoh, R.; Tachiya, M. Ultrafast Plasmon-Induced Electron Transfer from Gold Nanodots into TiO<sub>2</sub> Nanoparticles. *J. Am. Chem. Soc.* **2007**, *129* (48), 14852–14853. <https://doi.org/10.1021/ja076134v>.
- (8) Zhang, X.; Chen, Y. L.; Liu, R.-S.; Tsai, D. P. Plasmonic Photocatalysis. *Rep. Prog. Phys.* **2013**, *76* (4), 046401. <https://doi.org/10.1088/0034-4885/76/4/046401>.
- (9) Nosaka, Y.; Fox, M. A. Kinetics for Electron Transfer from Laser-Pulse Irradiated Colloidal Semiconductors to Adsorbed Methylviologen: Dependence of the Quantum Yield on Incident Pulse Width. *J. Phys. Chem.* **1988**, *92* (7), 1893–1897.  
<https://doi.org/10.1021/j100318a039>.
- (10) Matthews, R. An Adsorption Water Purifier with in-Situ Photocatalytic Regeneration. *J. Catal.* **1988**, *113* (2), 549–555. [https://doi.org/10.1016/0021-9517\(88\)90283-7](https://doi.org/10.1016/0021-9517(88)90283-7).
- (11) Hashimoto, K.; Irie, H.; Fujishima, A. TiO<sub>2</sub> Photocatalysis: A Historical Overview and Future Prospects. *Jpn. J. Appl. Phys.* **2005**, *44* (12), 8269–8285.  
<https://doi.org/10.1143/JJAP.44.8269>.
- (12) Baraton, M.-I. Nano-TiO<sub>2</sub> for Solar Cells and Photocatalytic Water Splitting: Scientific and Technological Challenges for Commercialization. *Open Nanosci. J.* **2011**, *5* (1), 64–77. <https://doi.org/10.2174/1874140101105010064>.
- (13) Gueymard, C. A. The Sun's Total and Spectral Irradiance for Solar Energy Applications and Solar Radiation Models. *Sol. Energy* **2004**, *76* (4), 423–453.  
<https://doi.org/10.1016/j.solener.2003.08.039>.
- (14) O'Regan, B.; Grätzel, M. A Low-Cost, High-Efficiency Solar Cell Based on Dye-Sensitized Colloidal TiO<sub>2</sub> Films. *Nature* **1991**, *353* (24), 737–740.
- (15) Burschka, J.; Pellet, N.; Moon, S.-J.; Humphry-Baker, R.; Gao, P.; Nazeeruddin, M. K.; Grätzel, M. Sequential Deposition as a Route to High-Performance Perovskite-Sensitized Solar Cells. *Nature* **2013**, *499* (7458), 316–319.  
<https://doi.org/10.1038/nature12340>.

- (16) Faraday Michael X. The Bakerian Lecture. —Experimental relations of gold (and other metals) to light. *Phil. Trans. R. Soc.* **1857**. 147  
<http://doi.org/10.1098/rstl.1857.0011>
- (17) Kelly, K. L.; Coronado, E.; Zhao, L. L.; Schatz, G. C. The Optical Properties of Metal Nanoparticles: The Influence of Size, Shape, and Dielectric Environment. *J. Phys. Chem. B* **2003**, *107* (3), 668–677. <https://doi.org/10.1021/jp026731y>.
- (18) Link, S.; El-Sayed, M. A. Shape and Size Dependence of Radiative, Non-Radiative and Photothermal Properties of Gold Nanocrystals. *Int. Rev. Phys. Chem.* **2000**, *19* (3), 409–453. <https://doi.org/10.1080/01442350050034180>.
- (19) Papavassiliou, G. C. Optical Properties of Small Inorganic and Organic Metal Particles. *Prog. Solid State Chem.* **1979**, *12* (3–4), 185–271.  
[https://doi.org/10.1016/0079-6786\(79\)90001-3](https://doi.org/10.1016/0079-6786(79)90001-3).
- (20) Hodak, J. H.; Martini, I.; Hartland, G. V. Spectroscopy and Dynamics of Nanometer-Sized Noble Metal Particles. *J. Phys. Chem. B* **1998**, *102* (36), 6958–6967.  
<https://doi.org/10.1021/jp9809787>.
- (21) Hartland, G. V.; Hu, M.; Sader, J. E. Softening of the Symmetric Breathing Mode in Gold Particles by Laser-Induced Heating. *J. Phys. Chem. B* **2003**, *107* (30), 7472–7478. <https://doi.org/10.1021/jp0276092>.
- (22) Mohamed, M. B.; Ahmadi, T. S.; Link, S.; Braun, M.; El-Sayed, M. A. Hot Electron and Phonon Dynamics of Gold Nanoparticles Embedded in a Gel Matrix. *Chem. Phys. Lett.* **2001**, *343* (1–2), 55–63. [https://doi.org/10.1016/S0009-2614\(01\)00653-4](https://doi.org/10.1016/S0009-2614(01)00653-4).
- (23) Link, S.; Furube, A.; Mohamed, M. B.; Asahi, T.; Masuhara, H.; El-Sayed, M. A. Hot Electron Relaxation Dynamics of Gold Nanoparticles Embedded in MgSO<sub>4</sub> Powder Compared To Solution: The Effect of the Surrounding Medium. *J. Phys. Chem. B* **2002**, *106* (5), 945–955. <https://doi.org/10.1021/jp013311k>.
- (24) Hodak, J. H.; Martini, I.; Hartland, G. V. Observation of Acoustic Quantum Beats in Nanometer Sized Au Particles. *J. Chem. Phys.* **1998**, *108* (22), 9210–9213.  
<https://doi.org/10.1063/1.476374>.
- (25) Hodak, J. H.; Henglein, A.; Hartland, G. V. Size Dependent Properties of Au Particles: Coherent Excitation and Dephasing of Acoustic Vibrational Modes. *J. Chem. Phys.* **1999**, *111* (18), 8613–8621. <https://doi.org/10.1063/1.480202>.
- (26) Hartland, G. V. Coherent Vibrational Motion in Metal Particles: Determination of the Vibrational Amplitude and Excitation Mechanism. *J. Chem. Phys.* **2002**, *116* (18), 8048–8055. <https://doi.org/10.1063/1.1469021>.
- (27) Hartland, G. V.; Hu, M.; Wilson, O.; Mulvaney, P.; Sader, J. E. Coherent Excitation of Vibrational Modes in Gold Nanorods. *J. Phys. Chem. B* **2002**, *106* (4), 743–747. <https://doi.org/10.1021/jp013887+>.
- (28) Semenov, A. D.; Gol'tsman, G. N.; Sobolewski, R. Hot-Electron Effect in Superconductors and Its Applications for Radiation Sensors. *Supercond. Sci. Technol.* **2002**, *15* (4), R1. <https://doi.org/10.1088/0953-2048/15/4/201>.
- (29) Sönnichsen, C.; Franzl, T.; Wilk, T.; von Plessen, G.; Feldmann, J.; Wilson, O.; Mulvaney, P. Drastic Reduction of Plasmon Damping in Gold Nanorods. *Phys. Rev. Lett.* **2002**, *88* (7), 077402. <https://doi.org/10.1103/PhysRevLett.88.077402>.
- (30) Linic, S.; Christopher, P.; Ingram, D. B. Plasmonic-Metal Nanostructures for Efficient Conversion of Solar to Chemical Energy. *Nat. Mater.* **2011**, *10* (12), 911–921.  
<https://doi.org/10.1038/nmat3151>.



- (31) Gomes Silva, C.; Juárez, R.; Marino, T.; Molinari, R.; García, H. Influence of Excitation Wavelength (UV or Visible Light) on the Photocatalytic Activity of Titania Containing Gold Nanoparticles for the Generation of Hydrogen or Oxygen from Water. *J. Am. Chem. Soc.* **2011**, *133* (3), 595–602. <https://doi.org/10.1021/ja1086358>.
- (32) Tian, Y.; Tatsuma, T. Mechanisms and Applications of Plasmon-Induced Charge Separation at TiO<sub>2</sub> Films Loaded with Gold Nanoparticles. *J. Am. Chem. Soc.* **2005**, *127* (20), 7632–7637. <https://doi.org/10.1021/ja042192u>.
- (33) Wang, P.; Huang, B.; Dai, Y.; Whangbo, M.-H. Plasmonic Photocatalysts: Harvesting Visible Light with Noble Metal Nanoparticles. *Phys. Chem. Chem. Phys.* **2012**, *14* (28), 9813–9825. <https://doi.org/10.1039/C2CP40823F>.
- (34) Kasap, S. O. *Optoelectronics and Photonics: Principles and Practices*, 2nd ed.; Pearson: Boston, 2013.
- (35) Fabregat-Santiago, F.; Mora-Seró, I.; Garcia-Belmonte, G.; Bisquert, J. Cyclic Voltammetry Studies of Nanoporous Semiconductors. Capacitive and Reactive Properties of Nanocrystalline TiO<sub>2</sub> Electrodes in Aqueous Electrolyte. *J. Phys. Chem. B* **2003**, *107* (3), 758–768. <https://doi.org/10.1021/jp0265182>.
- (36) Du, L.; Furube, A.; Yamamoto, K.; Hara, K.; Katoh, R.; Tachiya, M. Plasmon-Induced Charge Separation and Recombination Dynamics in Gold–TiO<sub>2</sub> Nanoparticle Systems: Dependence on TiO<sub>2</sub> Particle Size. *J. Phys. Chem. C* **2009**, *113* (16), 6454–6462. <https://doi.org/10.1021/jp810576s>.
- (37) Du, L.; Furube, A.; Hara, K.; Katoh, R.; Tachiya, M. Ultrafast Plasmon Induced Electron Injection Mechanism in Gold–TiO<sub>2</sub> Nanoparticle System. *J. Photochem. Photobiol. C Photochem. Rev.* **2013**, *15*, 21–30. <https://doi.org/10.1016/j.jphotochemrev.2012.11.001>.
- (38) Knight, M. W.; King, N. S.; Liu, L.; Everitt, H. O.; Nordlander, P.; Halas, N. J. Aluminum for Plasmonics. *ACS Nano* **2014**, *8* (1), 834–840. <https://doi.org/10.1021/nn405495q>.
- (39) Chan, G. H.; Zhao, J.; Schatz, G. C.; Van Duyne, R. P. Localized Surface Plasmon Resonance Spectroscopy of Triangular Aluminum Nanoparticles. *J. Phys. Chem. C* **2008**, *112* (36), 13958–13963. <https://doi.org/10.1021/jp804088z>.
- (40) Ekinci, Y.; Solak, H. H.; Löffler, J. F. Plasmon Resonances of Aluminum Nanoparticles and Nanorods. *J. Appl. Phys.* **2008**, *104* (8), 083107. <https://doi.org/10.1063/1.2999370>.
- (41) Karunakaran, C.; Magesan, P.; Gomathisankar, P.; Vinayagamoorthy, P. Absorption, Emission, Charge Transfer Resistance and Photocatalytic Activity of Al<sub>2</sub>O<sub>3</sub>/TiO<sub>2</sub> Core/Shell Nanoparticles. *Superlattices Microstruct.* **2015**, *83*, 659–667. <https://doi.org/10.1016/j.spmi.2015.04.014>.

# Chapter 2

## Experimental Methods

### **2.0 BRIEF OVERVIEW**

All the experiments used in this thesis revolve around transient absorption spectroscopy (TAS), which is the ‘bread and butter’ technique used in the Bragg lab. The details of this method are described below. Briefly, aluminum nanoparticles suspended in isopropyl alcohol (IPA) were placed into a 2 mm cuvette with a magnetic stir bar and excited with a femtosecond laser pulse. The excitation wavelength can vary with the specific wavelength that corresponds to the plasmon resonance of the particles being interrogated. The photoexcited or ‘hot’ particles are then probed by a femtosecond broadband white light laser pulse that gives a spectroscopic snapshot of the excited particles at various time delays after the initial excitation. The arrival of the probe pulse is controlled via a translation stage and can range from sub picosecond to  $\sim 1$  ns after excitation. Intensity dependent studies were accomplished by placing neutral density filters with well-known optical densities (OD) in the path of the pump beam to attenuate the excitation fluence.

### **2.1 DESCRIPTION OF THE FEMTOSECOND LASER SOURCE**

The laser source consists of two devices: a mode-locked femtosecond oscillator which outputs light at 800 nm with a 35 fs pulse width at 80 MHz and a power density of  $\sim 6$  nJ/pulse. This output is seeded into a regenerative amplifier that modulates this seed beam to produce pulses with an energy density of  $\sim 4.5$  mJ/pulse at 1 kHz while preserving

the 35 fs pulse duration through chirped-pulse amplification (CPA). This 800 nm fundamental beam can be used to drive various non-linear optical processes to create light of many different specific wavelengths from the UV (266 nm) to IR (2500 nm) to be used as an ultrafast excitation source. It can also be used to create a broadband white light continuum by being focused into different materials like sapphire or CaF<sub>2</sub>. Details of this laser system has been documented extensively.<sup>1-3</sup> The description here will be brief.

*Oscillator.* Any laser has 4 essential components: 1) pump source 2) gain medium 3) high reflector 4) output coupler/partial reflector. In the case of the femtosecond oscillator, a Ti:Sapphire rod acts as the gain medium and is pumped by a continuous wave (CW) solid-state diode laser with a fundamental wavelength of 532 nm. Light traveling within the high-finesse cavity between the high reflector and output coupler will make many passes through the gain medium and is strongly amplified by constructive interference of stimulated emission from the gain medium. Ti:Sapphire is capable of producing laser light anywhere from 680 nm to 1100 nm. In order to amplify a specific wavelength, optics that only reflect a narrow range of the fluoresce are used inside the cavity. Each lasing wavelength must be precisely an integral number of half wavelengths that fit inside the cavity; wavelengths that meet this criterion are referred to as longitudinal modes.

It is not possible to conduct ultrafast transient absorption experiments using a CW laser. Part of what makes ultrafast spectroscopy so powerful is the ability to excite a material on a timescale that will not interfere with the dynamics of the process being interrogated. Using a pulsed laser with a pulse width on the order of femtoseconds accomplishes this and in addition, the nature of generating short laser pulses results in very

high peak intensities that allow for many useful non-linear optical processes to take place as well as increased absorption by the sample.

Creating laser pulses can be accomplished through various methods. Here a “passive Kerr lens mode-locking” technique is used. Passive mode-locking requires a saturable absorber which is a material where the transmission of light through the material is intensity dependent. In a laser cavity at sufficiently high incident light intensity, atoms in the ground state become excited into an upper energy so fast that there is insufficient time for them to decay back to the ground state before the ground state becomes depleted, and the absorption subsequently saturates. Creating an artificial perturbation in the cavity by quickly varying the cavity path length the peak mode experiences self-phase modulation progressively locking adjacent modes together and forming a pulse. Pulse broadening that would break up the mode-locked pulse is eliminated with negatively chirped mirrors that balance dispersion in other cavity optics. The Gaussian spatial profile of the beam allows for the creation of a Kerr-lens<sup>4</sup> in the gain medium, allowing for an optical discrimination of mode-locked vs. CW in the oscillator cavity.

*Amplification.* As mentioned earlier, once the femtosecond seed pulse is generated it is routed into a regenerative amplifier that maintains the ~35 fs pulse width while increasing the energy density from 6 nJ/pulse to ~4.5 mJ/pulse and decreases the repetition from 80 MHz to 1 kHz. This is accomplished through Chirped-Pulse Amplification<sup>4</sup> (CPA). While the total energy per pulse of the seed beam may be low, each pulse possesses exceedingly high peak intensities which have the potential to damage optics if amplified directly. For this reason, the beam is stretched in time with a grating system which sends the higher frequency light (bluer) over a longer distance than the redder light. Stretching a

pulse in such a way results in a positive group velocity dispersion (GVD) and is said to be “positively chirped.”

Amplification is accomplished by optically pumping another Ti:Sapphire rod with ~30 mJ of 527 nm light at 1kHz from a solid-state laser (Nd:YLF). Since the gain medium through which the seed pulse passes already contains atoms in the excited state the pulse is intensified through stimulated emission. Regenerative amplifiers allow the seed to pass through the gain medium several times (in our case, 16-17) allowing for an overall amplification of greater than  $10^6$ . The entrance of the seed pulse and exit of the amplified pulse are synchronized to the firing of the pump laser by a set of Pockel cells triggered at the repetition rate of the pump laser. Once this stretched beam is amplified the pulse is recompressed by giving the pulse negative GVD, simply the reverse process that was used to stretch the pulse.

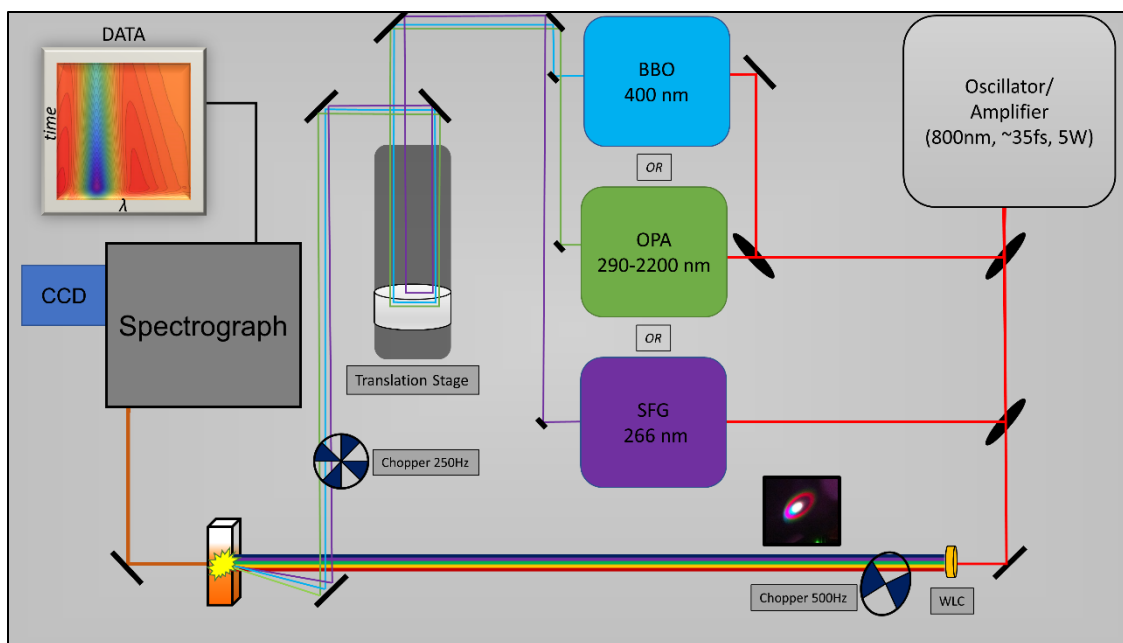
## **2.2 EXPERIMENTAL SETUP**

After leaving the amplifier the 800 nm fundamental beam is split multiple times for use in various non-linear optical processes that generate the desired wavelengths of light for any given experiment. A very small fraction of light is focused into a 2 mm x 2 mm sapphire or calcium fluoride ( $\text{CaF}_2$ ) plate in order to generate the broadband white light continuum (WLC) which serves as the TAS probe pulse. Immediately before the sample the light passes through a wire grid polarizer (WGP) set at magic angle relative to the pump pulse polarization to eliminate possible anisotropy in the absorption measurements.

Another portion of the amplifier output is routed into a series of BBO crystals to produce photoexcitation pump pulses at harmonic frequencies of the original 800 nm

output. Second harmonic generation (SHG) is achieved after passing through the first BBO to generate 400 nm light at relatively high fluences ( $\sim 100 \mu\text{J}/\text{pulse}$ ). If desired, this output can be used as the experimental pump source after attenuation of the beam power. Alternatively, the 400 nm light can also be spatially overlapped with the original 800 nm pulse in a second BBO crystal where sum frequency generation (SFG) occurs to generate 266 nm light which corresponds to the third harmonic of the fundamental.

Lastly a portion of the amplifier output can also be routed into an optical parametric amplifier (OPA, Coherent OPerA Solo). Using internally generated WLC and the original 800 nm beam the OPA is capable of generating tunable excitation pulses (290-2200 nm) via optical parametric amplification (splitting 800 nm photons into two photons of IR wavelength) followed by SFG and other non-linear processes. A schematic of the laser table with relevant non-linear processes can be seen in Figure 2.1.



**Figure 2.1:** Simplified laser table layout schematic. One of three primary experimental setups is chosen based on the desired excitation wavelength. Purple - 3<sup>rd</sup> harmonic UV light with a fixed wavelength of 266 nm. Green - Femtosecond OPA with variable wavelengths ranging from 290 – 2200 nm. Blue – 2<sup>nd</sup> frequency doubling BBO with fixed wavelength of 400nm.

### 2.3 STEADY-STATE SPECTROSCOPIES

One of the simplest optical spectroscopy methods is UV/VIS absorption, which quantifies the absorption of light by molecules or materials. It has four general components: a light source, a molecular solution or sample, a spectrometer for dispersion of light by wavelength or photon energy, and a light detector. Absorption spectroscopy requires a reference intensity,  $I_0$ , and is a differential measurement which detects an attenuation of light intensity,  $I$  of photons transmitted through the sample. This experiment allows for observations of optical resonances between ground and excited electronic states. Equations 2.2 and 2.3 give the relationships that quantify absorption, which are given in the unit-less parameters of percent transmittance (%T) or absorbance (ABS / OD). Equation 2.3 corresponds to Beer's law where  $\epsilon$  is the absorption coefficient,  $l$  is the path length and  $c$

is the concentration.

$$\%T = \frac{I}{I_0} \quad 2.2$$

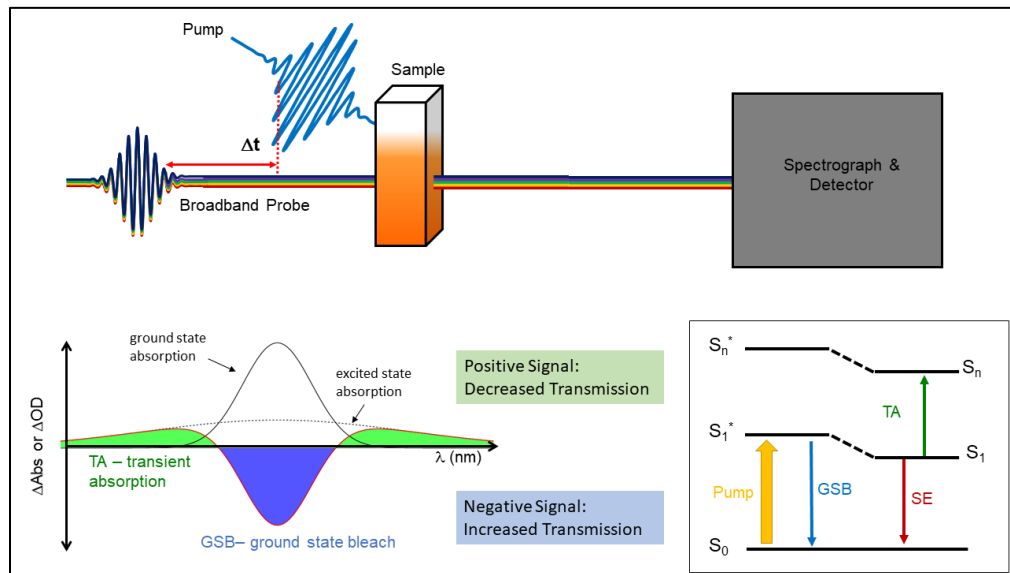
$$OD = -\log \frac{I}{I_0} = \epsilon lc \quad 2.3$$

## 2.4 INTRODUCTION TO TRANSIENT ABSORPTION SPECTROSCOPY

Transient Absorption Spectroscopy (TAS) also referred to as “pump-probe” spectroscopy is a derivative of UV/VIS spectroscopy where instead of acquiring a time-averaged or steady-state absorption spectrum a time-resolved absorption spectrum is acquired of some higher lying energy state following perturbation of the sample with light. In order to observe photophysical behavior of a higher energy state a light pulse, i.e. the “pump,” is required to initiate the photo-physical or photochemical process by photoexcitation in addition to the light source that monitors the change in sample absorption, i.e. the “probe”. The pump-probe measurement is a differential measurement like UV/VIS spectroscopy except that the transmission of probe light following sample excitation with the pump,  $OD_p$ , is referenced against the probe transmission with the pump absent,  $OD_u$ . Switching of the “pump” is generally achieved by using an optical chopper that physically blocks the light. Two phases, i.e. pump on/probe on and pump off/probe on, are required for determining the differential absorbance or  $\Delta OD$  at a given pulse time delay as given by Equation 2.4. The observed changes in intensity arise from the difference between the absorbance of the pumped  $OD_p$  and unpumped  $OD_u$  signals which is a function of time and wavelength.



$$\Delta OD(t, \lambda) = OD_p(t, \lambda) - OD_u(\lambda) = \log \left[ \frac{I_0(\lambda)}{I_p(t, \lambda)} \right] \quad 2.4$$



**Figure 2.2:** Basic schematic of pump-probe spectroscopy with relevant changes in signal response and their corresponding processes. The inset on the right describes the common molecular processes that result in different signal changes and the left side shows the response of a nanoparticle.

This technique is ideally suited to study processes occurring on timescales ranging from 100s of fs to nanoseconds, depending on the particular experimental setup. Some commonly studied processes include non-radiative relaxation of electronic excited states, vibrational relaxation, radiative relaxation, and thermalization of electrons excited in a metal. Additionally, it is possible to monitor the presence of intermediate states involved in photochemical reactions or energy transfer mechanisms. Due to the nature of this experiment as a differential signal measurement, it is possible to observe both positive and

negative changes in absorbance with each response yielding different information about the target molecule or material.

Figure 2.2 illustrates the consequences of transient absorption being a difference measurement. A positive  $\Delta OD$  indicates a decrease in light transmission through the sample at certain wavelengths which corresponds to the formation of an excited state which has a different absorption spectrum than the ground state, commonly referred to as the transient absorption spectrum (TA). While the excited-state population increases the corresponding ground state is depopulated leading to an increase in transmitted light and a negative  $\Delta OD$ , this is known as the ground-state bleach (GSB). Another feature commonly seen in these types of measurements is that of stimulated emission (SE) where an additional photon is emitted and corresponds to a negative signal. While it is easiest to describe these processes in terms of discrete energy levels that would be found in photoactive molecules, a large portion of the work described here will refer to spectra collected from metallic nanoparticles which do not have discrete energy “states” and are instead referred to as “hot” or “cold” to denote the deposition of energy.

The inset of Figure 2.2 depicts the molecular processes that would give rise to the various positive and negative signals observed in a TAS experiment, where the transient signal from an excited-state absorption (TA) can appear at a different wavelength than that of the ground state. In the case of plasmonic nanoparticles the center wavelength of the hot plasmon lies directly on top of that of the cold plasmon. This leads to a difference spectrum similar to that shown in the bottom left of the figure, however the hot particles have a wider range of energy distributions such that when the signals are subtracted there are areas on the periphery of spectrum that still appear as positive signals, sometimes

referred to as the “wings” of the TAS signal.

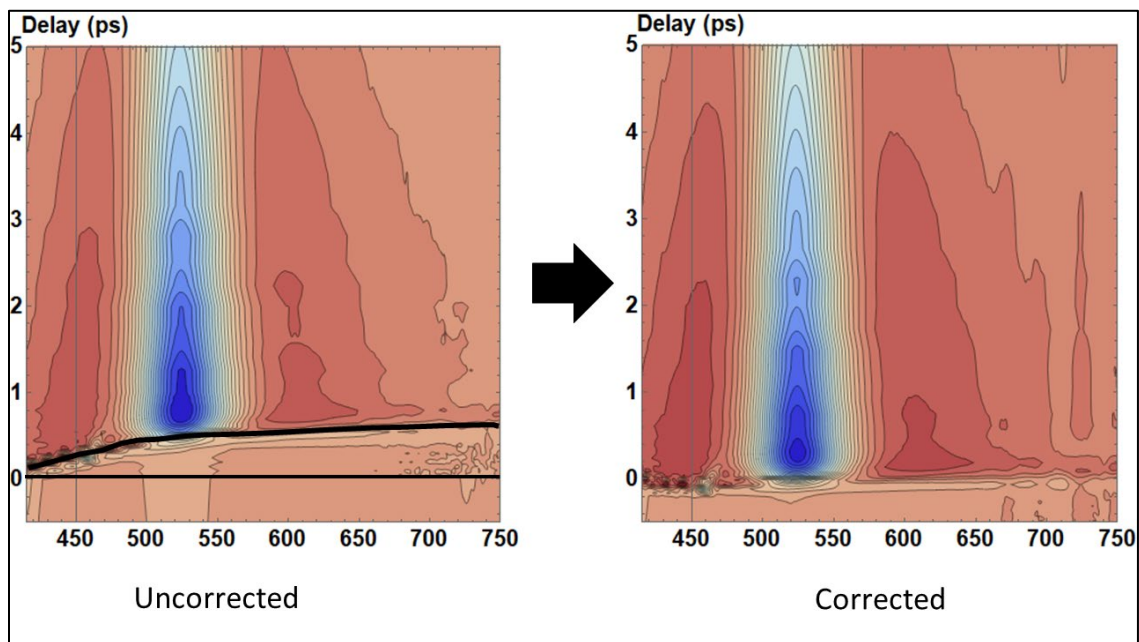
The evolution of the excited absorption spectrum is tracked by acquiring multiple ‘snapshots’ of the absorption spectrum at some time  $\Delta t$  after initial excitation at  $t_0$ , which is accomplished by employing an optical delay stage that changes the path length for an incident laser pulse. For processes occurring on an ‘ultrafast timescale’ laser pulses with a very narrow duration ( $\sigma < 200$  fs) are able to populate the excited state almost instantly after excitation, where the rise of the sample response is limited by the convolution of the laser instrument response function (IRF) and the decay of the excited state.

## **2.5 DATA ACQUISITION AND ANALYSIS**

All data collection was accomplished using a LabVIEW-based data acquisition program created by previous lab members. The transient spectra are calculated automatically by the LabVIEW program for each accumulation and averaged over the course of several accumulations before moving on to the next time delay. Details of this acquisition program can be found elsewhere.<sup>2</sup>

After experimental data is collected, the matrix of time- and wavelength-dependent transient absorption data is loaded into Mathematica for additional processing and analysis. If data is exceptionally noisy a gaussian filter can be applied in the wavelength dimension in order to smooth the data. Smoothing in the time dimension is avoided at all costs due to its effect on the time-resolution and possibly response lifetimes to be determined from analysis. After smoothing is applied it is necessary to account for temporal chirp introduced when the WLC is generated. The introduction of this temporal chirp causes bluer light to arrive at the sample earlier than redder wavelengths. In order to obtain accurate timescales this must be corrected. An example of pre and post chirp correction

can be seen in Figure 2.3.



**Figure 2.3:** Example of correction of chirp introduced by white light super continuum generation.

Briefly, this is accomplished in Mathematica by fitting a low order polynomial to the half-rise of the transient signals; this fit provides a common reference delay at all wavelengths. Corrected time delays are then calculated at each wavelength from a series of interpolating functions in order to shift all the experimental data to a set of common delays.

$$f(t) \circ \text{IRF}(t) = \left( H(t) \sum_n a_n e^{\frac{-t}{\tau_n}} \right) \circ \frac{1}{\sigma\sqrt{2\pi}} e^{-\frac{(t-\mu)^2}{2\sigma^2}} \quad 2.5$$

Kinetic traces are created by integrating spectral intensities for each time delay over a specified range of wavelengths that correspond to a region of interest, usually for each

apparent spectral feature in the spectrum. A non-linear regression algorithm is then used to fit the traces with an appropriate exponential kinetic model. At early times ( $< 1$  ps) the signal rise is accounted for by the convolution of the instrument response function (IRF) with the particular model. The IRF is computed as the gaussian envelope of the pump-probe cross-convolution. A general form is shown in Equation 2.5 where  $f(t)$  is the kinetic model being applied,  $H(t)$  is the Heaviside step function and  $IRF(t)$  is the instrument response. While this represents the general form of the function used, in some circumstances it is necessary to make customizations, such as the addition of exponential rise and damped oscillator terms. From these fits relevant excited-state lifetimes are extracted and used to make conclusions about the dynamics of the excited molecules or particles. More complex models for fitting time-dependent signals from Al nanoparticles are described in Chapters 3 and 4; fitting models accounting for singlet-singlet annihilation in polymer films are described in Chapter 5.

## 2.6 REFERENCES

- (1) Hu, K. *Fundamental Insights into the Charge Transfer Processes in Dye-Sensitized Solar Cells: Hole Transfer, Regeneration Charge Recombination and Electron Injection*. PhD Thesis, Johns Hopkins University, Baltimore, MD. 2014
- (2) Magnanelli, T. J. *Spectroscopic Probes of Charge Separation, Energy Transfer and their Dependencies on Local Structure in Assembled Organic Materials*. PhD Thesis, Johns Hopkins University, Baltimore, MD. 2017
- (3) Molloy, M. S. *Structural and Solvent Control of Photochemical Bond Formation: Nonadiabatic Photocyclization of Ortho-Terphenyls*. PhD Thesis, Johns Hopkins University, Baltimore, MD, 2016
- (4) Verdeyen, J. *Laser Electronics*, 3rd ed. Prentice Hall, Englewood Cliffs, 1995

# Chapter 3

## Dynamics of Energy Transfer in Large Plasmonic Aluminum Nanoparticles

### 3.0 ABSTRACT

We report the first photophysical characterization of energy-transfer dynamics in large (100 nm diameter) plasmonic aluminum nanoparticles suspended in liquid isopropanol. The spectral response of the particles to ultrafast excitation is characterized by a decrease in light transmission broadly across the visible and near infrared on a 700 fs timescale that is consistent with predictions for electron-lattice relaxation processes. Time-dependent bleaching of the interband transitions is largely isolated from spectral changes to the intraband transition associated with light scattering and provides a window into electron-electron thermalization dynamics that occur on a  $\sim 350$  fs timescale. Subsequent relaxation in these particles is characterized by a 250 ps energy transfer to the surrounding medium – comparable to energy-transfer rates expected for much smaller particle sizes ( $< 10$  nm in diameter). Using a two-interface model, we find that the rapid thermal energy transfer is accounted for by the presence of a compact  $\sim 4$  nm native oxide layer on the aluminum nanoparticles. We propose that using surface modifications, including controlled oxidation, could be an effective tool to engineer heat transfer rates from large particles to the surrounding medium and could be a handle for controlling thermal decay processes in a broad range of applications involving metal nanoparticles.

### 3.1 INTRODUCTION

Novel realizations of metal nanoparticles (NPs) are of continuing interest due to their unique optical properties and potential applications in optoelectronics, sensing, and catalysis.<sup>1-6</sup> Plasmonic materials have great appeal as harvesters of visible light, with plasmonic-enhancement promising increased efficiency and spectral sensitivity of catalytic materials.<sup>7-10</sup> In contrast to bulk metals, metal NPs exhibit localized surface plasmonic resonances (LSPRs) that are tunable via adjustment of particle size, shape, and composition as well as the properties of the surrounding environment.<sup>11,12</sup> Methods for synthesizing, functionalizing and manipulating gold and silver NPs are well established, and hence their photophysical properties, including narrow and tunable LSPRs across the visible and near-infrared (NIR) regions of the electromagnetic spectrum, are well characterized.<sup>13-16</sup> However, large-scale deployment of precious-metal materials is impractical for many applications due to their high cost and relatively low earth abundance. Several alternatives have been proposed and synthesized,<sup>17-19</sup> but there remains an urgent need to understand their photophysical properties, many of which differ non-trivially from gold and silver due to their unique electronic structures and complex dielectric constants.<sup>20,21</sup>

Aluminum, in particular, is an inexpensive earth-abundant plasmonic material and a promising alternative to noble metals for applications requiring UV sensitivity and scalability. The plasmon resonance of bulk aluminum metal falls in the ultraviolet, but the LSPRs of aluminum NPs have been tuned successfully to the visible and NIR using size- and shape-modulation<sup>22-24</sup> and are tunable over an even wider spectral range than those of Au or Ag.<sup>22</sup> Aluminum also forms a native oxide layer at its surface in air<sup>25</sup> that further



red-shifts the LSPRs of particles. Unlike the interband transitions of gold (5d-6s) and silver (4d-5s), with threshold energies that overlap with the intraband plasmon resonance, the interband transitions of aluminum fall at 1.5 eV and do not overlap significantly with the intraband transitions.<sup>21</sup> Greater understanding of how these differences in electronic structure affect energy transfer mechanisms is critical for developing optoelectronic and photocatalytic applications<sup>26,27</sup> based on plasmonic aluminum.

The photophysical dynamics of noble-metal plasmonic nanomaterials have been characterized extensively with ultrafast transient absorption spectroscopy over the last two decades.<sup>28,29</sup> Studies on relaxation dynamics of aluminum have been recently conducted on bulk films, nanorods and nanodisks.<sup>30-33</sup> It is now well understood that interaction between a plasmonic NP and a femtosecond laser pulse creates a coherent electronic state (a “plasmon”) that rapidly dephases (typically in 5-10 fs) to a highly non-thermal electron distribution.<sup>34,35</sup> These “excited” non-equilibrium NPs subsequently relax through a sequence of energy-conversion and transfer mechanisms beginning with thermalization via electron-electron (10-100 fs)<sup>36,37</sup> and electron-lattice (~1-10 ps)<sup>29,38</sup> scattering followed by lattice relaxation by intraparticle equilibration (10s of ps)<sup>38,39</sup> and thermal energy transport to the surrounding environment (100s of ps to nanoseconds).<sup>40-42</sup> The extensive body of work that has explored these processes has also led to an understanding of how energy transfer scales with NP dimensions<sup>35,38,40</sup> and shape<sup>43-47</sup> as well as particle composition<sup>48,49</sup> and interface properties.<sup>42,50</sup> Transient optical methods have also been used to demonstrate that hot electrons generated in noble metal NPs are able to overcome an interfacial Schottky barrier when coupled to TiO<sub>2</sub>, a common and robust semiconductor, thereby facilitating enhanced photocatalytic activity.<sup>51-54</sup>

In this study, we report the first photophysical characterization of energy-transfer dynamics in large, solution-synthesized aluminum NPs. Time-scales for spectral dynamics are similar to those ascribed for electron-electron, electron-photon, and lattice cooling temperatures for noble-metal particles,<sup>28,29,55</sup> although we find that the spectral responses of Al NPs differ qualitatively. Notably, bleaching of the interband transitions is largely isolated from spectral changes associated with LSPR and provides a window into electron-electron thermalization dynamics. Furthermore, we find a ~250 ps energy transfer to the surrounding medium – comparable to energy transfer rates for a small (<10 nm in diameter) NPs, but much faster than predicted for the particle size (98 nm in diameter) studied. To understand this phenomenon, we investigated thermal energy transfer dynamics using a two-interface model and find that rapid thermal energy transfer out of the Al core is mediated by the presence of the ~4-nm thick native oxide layer, pointing the way to using surface modifications as a tool to engineer heat transfer rates in applications such as photocatalysis.

### **3.2 RESULTS AND DISCUSSION**

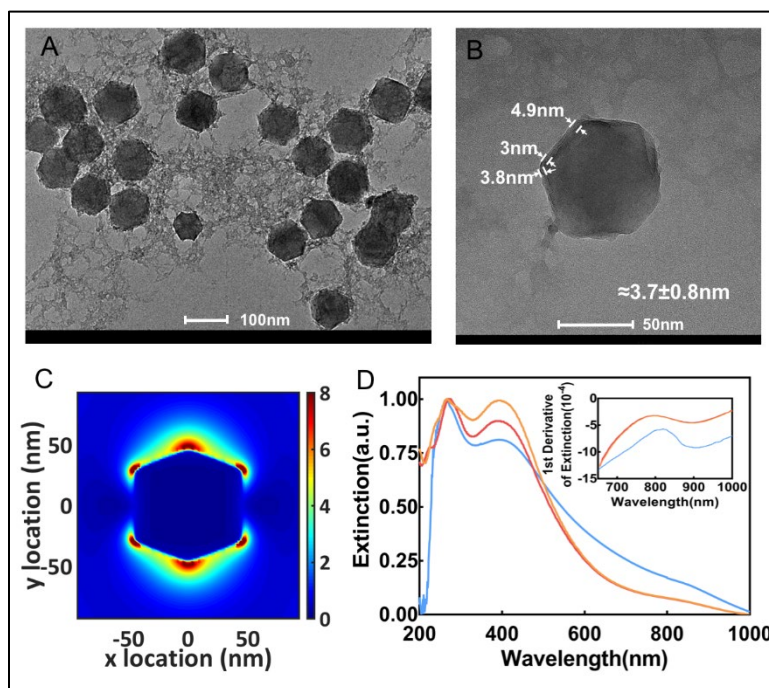
We synthesized aluminum NPs using modifications of established procedures.<sup>56</sup> Briefly, the particles were formed through decomposition of dimethylethylamine alane under mild heating using titanium (IV) isopropoxide as a catalyst. Morphologies of the synthesized aluminum NPs are shown in the transmission electron microscope (TEM) image in Figure 1A. According to our analysis of the size distribution, the particles are relatively monodisperse with an average diameter of  $98 \pm 12$  nm (see Figure A1.1). The NP shapes are primarily icosahedra and truncated trigonal bipyramids. Figure 3.1B shows

a high-resolution TEM image of a single aluminum NP taken using a FEI Talos S200 in which a thin oxide shell with an average thickness of approximately 3.7 nm is visible, consistent with previous observations.<sup>57</sup>

Based on the morphologies obtained from these images, we employed finite difference time-domain (FDTD) simulations to predict the LSPR spatial field intensity distribution (Figure 1C) and spectrum (Figure 3.1D) of the aluminum NPs. The blue curve in Figure 3.1D shows the experimental extinction spectrum of the aluminum NPs in 2-propanol measured by UV-Vis spectrophotometry. The solution exhibited a clear broadband absorption peak due to the NP dipolar plasmon resonance with a maximum at 392nm, as well as a peak at 269 nm associated with the quadrupolar plasmon resonance (spatial field intensity distribution shown in Figure A1.1d) in both simulated and measured extinction spectra. We used FDTD simulations to calculate the extinction cross section of an icosahedral aluminum NP 93 nm in diameter with and without an aluminum oxide shell of  $3.7 \pm 0.8$  nm in thickness. The simulated peak extinction cross-sections of the aluminum NPs without (red curve) and with (orange curve) an oxide layer are 389 nm and 393 nm, respectively; the latter matches well with that of the measured extinction peak, with the broadening of the peaks in the measured extinction spectra compared to the simulated ones attributed to the slight size inhomogeneity of the Al NP solution. We also observe that there is a broad shoulder, both in the measured and the calculated extinction spectra, between 800 nm and 900 nm that is clearer from plots of the first derivative shown in the inset of Figure 3.1D. This shoulder in the experimental spectrum falls at 815 nm and agrees well with the known spectral position of the parallel-band interband transitions in aluminum ( $\sim 1.5$  eV).<sup>21</sup> Importantly, the extinction spectrum is dominated by particle scattering *except*

in the region of the interband transition (*vide infra*)

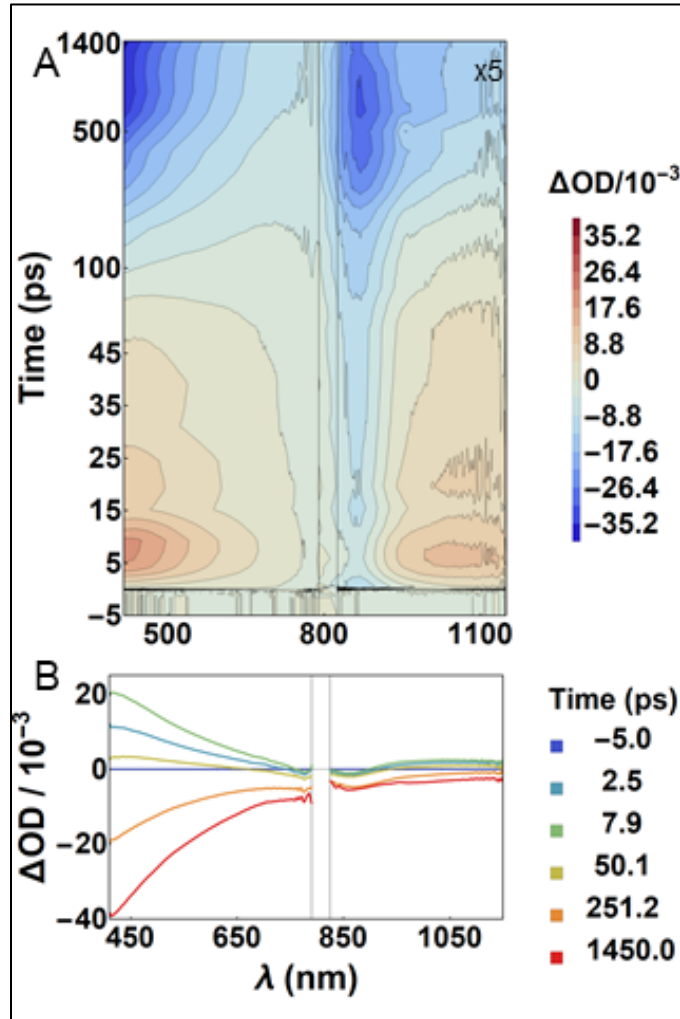
Guided by this understanding of steady-state properties, we interrogated the photophysics of these particles suspended in 2-propanol with transient absorption spectroscopy. Figure 3.2A presents a contour plot of time-dependent changes in optical density (i.e. extinction) from 420 – 1150 nm following interaction with ultrafast laser pulses at 400 nm (fluence of  $134 \mu\text{J cm}^{-2}$ ). “Time zero” can be identified by the sharp line



**Figure 3.1.** (A) TEM image of aluminum NPs. (B) A single aluminum particle surrounded by an oxide layer with an average thickness of 3.7 nm. (C) FDTD-calculated spatial electromagnetic field profile for a 93 nm-diameter aluminum NP at the LSPR wavelength of 393 nm (color scale in a.u.). (D) UV-Vis-NIR extinction (blue curve) of an aluminum NP solution in 2-propanol. FDTD-calculated extinction cross sections for a single bare aluminum icosahedron in a 2-propanol background (red curve) and an aluminum icosahedron with a  $3.7 \pm 0.8$  nm thick aluminum oxide shell (orange curve) in the same background. The inset shows the first derivative of measured (blue) and simulated (red/orange) extinction near the aluminum interband transition (1.5 eV).

near the bottom of the plot that is associated with ultrafast coherent interactions of the laser pulses with the sample solution that occur during the pulse cross correlation. Spectra collected at various time delays for each spectral region are plotted in Figure 3.2B. In total,

Figure 3.2 demonstrates that changes in extinction occur broadly across the visible and NIR.

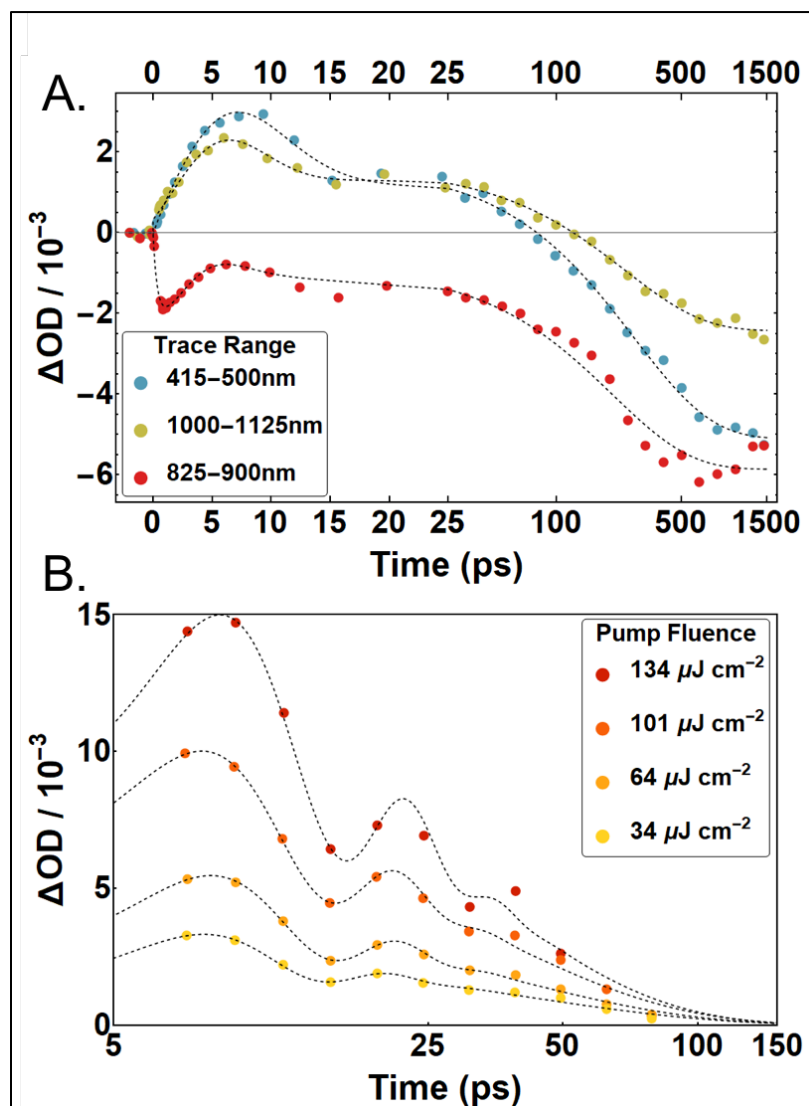


**Figure 3.2.** (A) Contour plot of transient spectra from 420 – 790 nm and 820-1150 nm after 400 nm excitation with a fluence of  $134 \mu\text{J cm}^{-2}$ . The time axis is linear from 0-50 ps and logarithmic from 50-1450 ps. Data in the NIR region is scaled by a factor of 5 for clarity. (B) Visible (left) and NIR (right) transient spectra at selected time delays of the same data sets (no scaling applied in NIR).

Figure 3.3 plots temporal traces obtained by averaging over three different spectral regions: a region to the red of the LSPR peak (415-500 nm), near the aluminum interband transition (825-900 nm), and in the NIR beyond the interband transition (1000-1125 nm).

Transient spectral dynamics can be summarized as follows: Immediately following excitation, a slow induction to a positive  $\Delta OD$  occurs broadly across the visible and beyond 900 nm, reaching a maximum positive value by 8 ps. At later time delays, this broad signal decreases in amplitude turning to a negative  $\Delta OD$  on a timescale of a few hundred picoseconds. The time-dependence of transient signals collected in the visible and longer-wavelength NIR are highly similar. Interestingly, despite the plasmon resonance having a maximum extinction at 392 nm, no extinction bleach is observed in this region immediately after excitation, which differs from studies conducted previously with noble-metal nanoparticles and aluminum nanodisks.<sup>33</sup>

A different temporal response is observed near the Al interband transition. Here the extinction drops rapidly to negative values within a few hundred femtoseconds after sample excitation (Figure 3.3, red symbols) – a timescale slower than the experimental time resolution, but faster than the slow induction of extinction observed in other spectral regions. This negative dip arises from a “bleach” of the Al inter-band transition. At later delays, the bleach is overtaken by a broad negative extinction observed across the near infrared.



**Figure 3.3.** (A) Time-dependent traces obtained from three different spectral regions: near the LSPR peak, (415-500 nm) (blue); off the LSPR peak in the NIR (1000-1125 nm) (gold); and in the interband transition region of metallic aluminum (825-900 nm) (red). Data from the visible region of the spectrum were scaled by a factor of 0.2 in order to display all three data sets in one plot. Fitting curves (described in the text) are displayed in black. (B) Fits to damped signal oscillations observed in the visible region at each of the excitation fluences used in this study.

Numerous studies have demonstrated the effects of high-fluence laser excitation on the photophysics of plasmonic NPs, and it is critical to rule these out before ascribing the timescales observed to specific energy-transfer processes. Non-linear effects can include,

but are not limited to, bubble formation by local solvent vaporization,<sup>58</sup> persistent hole burning through particle ablation or melting,<sup>59</sup> and multi-photon absorption.<sup>60</sup> Notably, the broad spectral response we observe long after photoexcitation manifests as a reduction in optical density. In contrast, the formation of large vapor bubbles around photoexcited gold NPs has been shown to increase the probe extinction via increased Mie scattering; additionally, the threshold fluence for bubble formation (5.2 mJ cm<sup>-2</sup> for 60 nm Au NPs<sup>58</sup>) is much higher (~100 fold) than what was used for our transient absorption studies (*vide infra*). To rule out contributions from laser-induced melting, we examined NP morphology using high-resolution TEM (HRTEM) imaging both before and after prolonged exposure to the 400-nm excitation source (4-6 hours of irradiation with continuous sample mixing). The images in Figure A1.2 reveal that there is no observable change in particle morphology. Additionally, there was no observable change in the steady-state absorption of the ensemble, indicating no changes in the particle properties with irradiation. Finally, spectral transients were collected at a series of laser excitation fluences (Figure A1.3). Time-dependent traces collected at various fluences are shown in Figure A4A and exhibit similar time-dependent behavior across all fluences. The fluence-dependence of the maximum positive and negative extinction is plotted as a log-log plot in Figure A4B and reflects a closely linear relationship between measured fluence and signal (slope = 1.29±0.15). Together, these control experiments indicate that the spectral responses apparent in Figures 3.2, 3.3, A1.3 and A1.4 reflect the intrinsic relaxation dynamics of the plasmonic particles in a linear excitation regime.

As described in the introduction, the photoinduced responses of Au and Ag NPs involve at least four processes that impact their transient spectral dynamics: electron-



electron thermalization (~100 fs), electron-phonon thermalization (~1 ps), and lattice relaxation dynamics, which include coherent phonon oscillations (~few-10s of ps period) and thermal energy transfer to the surrounding medium (10s to 100s of ps). The transient spectra of Al NPs evolve on qualitatively similar timescales as Au and Ag, although the transient spectra have somewhat different characteristics due to the weaker overlap between the intra and interband transitions in Al and the fact that extinction associated with the Al intraband transition is dominated by the scattering cross section. The ultrafast induction in the interband bleach region is similar to behavior observed with Ag NPs in a glass matrix;<sup>36</sup> this induction in the bleach is attributed to electron-electron thermalization that fills states above the Fermi level that serve as terminal states for the interband transition, such that the bleach of this transition increases with electronic relaxation.<sup>61,62</sup> The rise in transient spectra broadly across the visible and NIR occurs in part due to particle lattice heating in response to LSPR excitation and subsequent electron thermalization.<sup>38</sup> It also arises from modulation in the extinction coefficient due to phonon breathing modes activated by electron-lattice energy transfer. The signal induction can be seen quite clearly for Al NPs, as there is no overlap with the interband transition in the visible spectral region. Importantly, we expect that this signal will be dominated by modulation in scattering cross section; qualitatively, the rapid thermal expansion of the particle should increase scattering cross-section. The rapid photoinduced depletion of the interband transition in the NIR provides a direct signature of electron-electron thermalization within the material by which to clock the slow induction in electron-lattice thermalization and lattice heating.

Finally, the slower inversion of the broad transient spectrum occurs on timescales consistent with thermal energy transport observed with noble-metal NPs.<sup>40,42,49,63</sup> The

optical response at the latest delays explored in our experiment ( $\sim 1$  ns) is characterized by a broadband negative signal that has been observed in silver and gold particles previously and has been attributed to thermal lensing<sup>64</sup> or changes in the dielectric medium of the solvent.<sup>65</sup> In the present study the possibility of thermal lensing was ruled out by varying the slit width of the spectrograph in order to confirm that 100% of transmitted light was observed on the detector. The dielectric constant of the solvent is expected to decrease as it heats up due to thermal energy transport. Previous studies that attributed negative extinction to changes in the dielectric of the solvent medium were conducted in water ( $(\partial\epsilon_m/\partial T)_v = -6.2 \times 10^{-5} \text{ K}^{-1}$ );<sup>65</sup> in contrast,  $(\partial\epsilon_m/\partial T)_v \sim -0.15 \text{ K}^{-1}$  for isopropanol.<sup>66</sup> The authors of the previous study only observed this effect at very high laser excitation fluences ( $> 1 \text{ mJ cm}^{-2}$ ); although our experiments were conducted with comparatively lower pump fluences the extremely high sensitivity of the isopropanol dielectric constant to temperature variation explains this effect. Indeed, FDTD simulation shows that the scattering cross-section will blueshift with lower dielectric of the surrounding medium (e.g. Figure A1.5), resulting in a broad negative change in particle extinction, consistent with observations from our experiments.

In order to get a better handle on the timescales associated with these processes, we fit the traces plotted in Figure 3.3A with various time-dependent functions. The signal intensity after lattice heating was modeled with exponential rise ( $\tau_1$ ) and decay ( $\tau_2$ ) as well as damped harmonic oscillations according to Equation 3.1.

$$a_1 \left( 1 - e^{-\frac{t}{\tau_1}} \right) + a_2 e^{-\frac{t}{\tau_2}} + a_3 e^{-(\gamma t)^2} \text{Cos} \left( \frac{2\pi t}{\tau_R} + \varphi \right) + c \quad 3.1$$

Here  $\tau_R$ ,  $\gamma$ , and  $\phi$  are the oscillatory period, damping parameter and phase offset for the phonon breathing modes. Timescales obtained for all three regions are very similar and are listed in Table 3.1 below (all fit parameters are given in Table A1.1).

**Table 3.1.** Time constants obtained by fitting wavelength-dependent transients with Equation 3.1.

	$\tau_1$	$\tau_2$	$\tau_R$
Visible (415-500 nm)	0.7 ps	191 ps	25 ps
NIR Interband (825-900 nm)	0.35 ps	206 ps	23 ps
NIR (1000-1125 nm)	3.5 ps	244 ps	22 ps

The rise timescale was necessary in order to obtain acceptable fits to the signal induction in the visible and is attributed to the electron-phonon thermalization. (In the interband region this value corresponds with the ultrafast bleach induction.) This analysis in the visible therefore indicates an effective electron-to-lattice energy transfer lifetime of  $\sim 0.7$  ps; values obtained at all fluences ranged 0.7-0.9 ps, with no obvious trend (Table A1.2). We note that this model poorly resolves the phonon oscillations in the data when applied to the entire data set. In order to obtain a more accurate period for this oscillation a truncated data set (5 to 100 ps) was fit for visible transients collected at each excitation fluence, as shown in Figure 3.3B. Based on this analysis we find  $\tau_R$  to be  $\sim 13.7 \pm 0.6$  ps., with a weak dependence on excitation fluence (Table A1.3).

The decay timescales (200-250 ps) obtained from these fits is in qualitative agreement with expectations for thermal energy transport to the surrounding solvent medium (*vide infra*).<sup>42,49,50,63,67</sup> The signal oscillation period is generally consistent with timescales associated with modulation in optical properties as a result of low-frequency “breathing” or coherent phonon displacement that can occur as a result of fast electron-to-

phonon energy transfer.<sup>38,39</sup> Using the method described in previous work<sup>68</sup> the approximate longitudinal speed of sound of the particles was calculated using the equation

$$\tau_R = \frac{2\pi R}{\eta c_l} \quad 3.2$$

Here  $\tau_R$  is the oscillation period,  $R$  is the radius of the particles,  $c_l$  is the longitudinal speed of sound of Al and  $\eta$  is an eigenvalue calculated from Lamb's equation (approximated in this case using the melting point of Al). Based on this analysis and using the observed period of 13.7 ps the longitudinal speed of sound was calculated to be 7,900 m/s, which is not physical for pure Al. The speed of sound in aluminum oxide is much higher than that of aluminum, 10,900 m/s vs. 6,405 m/s at room temperature, respectively<sup>69</sup> This intermediate value is reasonable for a particle composed of both materials. Damping of these modes likely reflects attenuation of the acoustic breathing modes by the aluminum oxide shell as well as the effect of size polydispersity on the ensemble-averaged phonon breathing.

A phenomenological two-temperature model (TTM)<sup>65</sup> is commonly used to treat thermal energy transfer from electronic to lattice degrees of freedom in metals. Briefly, the model is composed of two coupled heat equations that describe how the electronic temperature changes with time after laser excitation.

$$C_e(T_e) \frac{dT_e}{dt} = -g(T_e - T_l) \quad \text{and} \quad C_l \frac{dT_l}{dt} = g(T_e - T_l) \quad 3.3$$

Here  $T_e$  and  $T_l$  are the electronic and lattice temperatures,  $C_e(T_e)$  and  $C_l$  are the corresponding specific heats, and  $g$  is the electron-phonon coupling constant. This model involves a rate constant for energy transfer that scales inversely with electronic temperature, which results in a non-exponential rise in the lattice temperature. The electronic specific heat is found using the relationship  $C_e(T_e) = \gamma T_e$ . Using the two temperature model with the Sommerfeld constant  $\gamma = 91.2 \text{ (J} \cdot \text{m}^{-3} \text{K}^{-2}\text{)}$ , and an electron-phonon coupling constant of  $g = 1.2 \times 10^{17} \text{ (W} \cdot \text{m}^{-3} \text{K}^{-1}\text{)}$  for Al.<sup>70</sup> The maximum electronic temperature was approximated using the same method and assumptions as previous studies,<sup>33</sup> we estimate a maximum electronic temperature in the range of 500-1000 K and the electron-to-lattice energy transfer timescale corresponding to a decay of  $(1/e)$  is found to be 300-600 fs, which is qualitatively consistent with timescales obtained from our fits.

The average intensity in the region of the interband transition of metallic aluminum (800-850 nm) exhibits a bleach signal that appears rapidly following the instrument response. This behavior is similar to that exhibited by noble metals while probing in the region of their respective interband transitions.<sup>71</sup> As noted above, transient signals in the region of the interband transition also have contributions from the time-dependent spectral response of the particles observed at other wavelengths (i.e. scattering); this is clear from the very similar modulations in signal intensity on the picosecond to nanosecond timescales that occur with a clear offset in spectral intensity between the interband and 1000-1125 nm regions. The superposition of these signals makes it difficult to analyze the time-dependence of the interband bleach feature alone. When the model is applied to the region near the interband transition of aluminum this reveals a bleach induction time,  $\tau_{bleach}$ , of  $\sim 350$  fs that reflects the slowest phases of electron-electron thermalization. This timescale

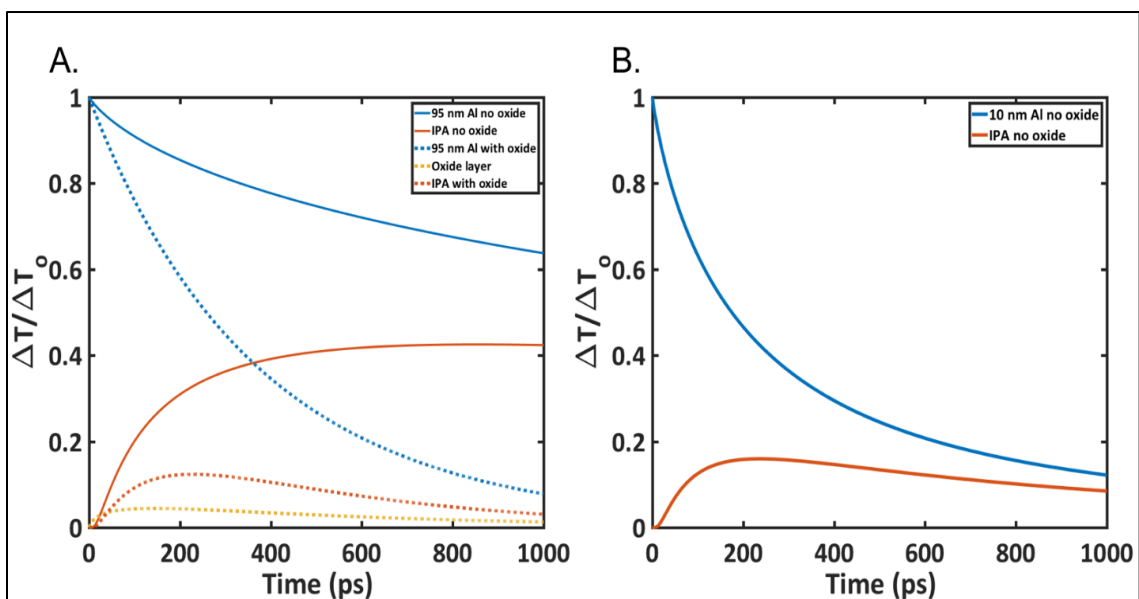
is slightly longer than the longest electron thermalization timescales observed in large Au and Ag NPs.<sup>36</sup> As noted above, the signature of this bleach becomes less pronounced and is overtaken by the broad negative extinction spectrum at later delays, indicating that the bleach recovers as a consequence of thermal energy transfer out of the Al core. Although exact separation of the time-dependent scattering cross-section and interband absorption is not possible, a crude analysis reveals that the interband transition recovers on a timescale commensurate with nanoparticle cooling (Figure A1.6).

Based on precedent with noble-metal NPs, the slowest relaxation timescales observed in our measurements are assigned to thermal energy transport to the surrounding solvent environment. Various models for thermal energy transfer from nanoparticles to the surrounding media have been developed and applied.<sup>42,49,63,67,71,72</sup> For example, Vallée and coworkers<sup>63</sup> have applied thermal transfer models to fit the time-dependence of transient absorption measurements conducted with Au and Ag in solution and embedded in various glasses.<sup>71,73</sup> These previous studies have investigated a large range of nanoparticle sizes (from about 5 nm to 133 nm in diameter).<sup>71,72</sup> Their model involved a single interface between a NP and the surrounding medium to compute the temperature evolution of both the particle and the medium. Thermal dynamics in this model are governed by the interfacial thermal conductance ( $G$ ) as well as the thermal conductivity ( $\lambda$ ) and heat capacity ( $c$ ) of both the metal NP and surrounding medium. Whereas the bulk values of  $\lambda$  and  $c$  are reasonable approximations for NPs,  $G$  is generally not known and is varied to fit the temporal behavior observed from optical measurements. Therefore, this line of investigation has also explored the impact of particle size and the chemical composition of interfaces on energy transfer.<sup>40,42,50,63,67,71</sup>

We extended our analysis to a two-interface model to incorporate the native aluminum oxide layer on our particles, as described in the Supporting Information. Table 3.2 gives a summary of parameters relevant for the aluminum NP / aluminum oxide shell / isopropanol system.

**Table 3.2.** Heat capacities and thermal conductivities of aluminum, aluminum oxide and isopropanol.<sup>72</sup>

Material	$c$ ( $10^6 \text{ J.m}^{-1} .\text{K}^{-1}$ )	$\Lambda$ ( $\text{W.m}^{-1} .\text{K}^{-1}$ )
Aluminum ( $p$ )	2.43	205
Aluminum Oxide ( $o$ )	3.48	30
Isopropanol ( $m$ )	2.1	0.16



**Figure 3.4.** Simulations of thermal energy transport. (A) Temperature evolution relative to the initial temperature increase ( $\Delta T_0$ ) of the nanoparticle after optical excitation at the surface of a large (93 nm diameter) aluminum nanoparticle (solid blue line) and 3 nm into the surrounding isopropanol (solid red line) for the case where no oxide is included, and where a thin oxide shell layer on the nanoparticle is incorporated into the model (blue and red dotted lines). The yellow dotted line corresponds to temperature evolution in the oxide layer. (B) Temperature evolution for a small (10 nm diameter) aluminum nanoparticle without an oxide layer. The thermal decay dynamics in this case roughly match those of the larger particle with an oxide shell.

We used our model to explore the thermal dynamics in aluminum NPs with 93 nm diameters and 3.7 nm aluminum oxide shells suspended in isopropanol. Our results are plotted in Figure 3.4A and indicate that heat dissipates much more quickly from the aluminum core when an oxide shell is present (blue dashed line) compared to the case without an oxide shell (blue solid line). Notably, the  $1/e$  timescale for energy loss from the Al core from these simulations is  $\sim 300$  ps when the oxide is present, in close agreement with the relaxation timescales observed in our experiments. Varying the free parameter  $G$  (thermal interface conductance) can control the rate of decay. The value used for the plot in Figure 3.4 was chosen from typical literature values for the thermal interfacial conductance of metal/metal oxide interfaces.<sup>71,74–77</sup> Additionally, we predict that large Al NPs (93 nm in diameter) with an oxide layer possess thermal transport properties equivalent to those of much smaller particles (10 nm in diameter, solid blue line in Figure 3.4B) with no oxide layer. These results indicate that the native oxide coverage on Al NPs likely provides an intrinsic protection against melting or ablation after interaction with a high intensity laser pulse by facilitating fast and efficient thermal energy transfer to the surrounding solvent. Additional studies of the temperature evolution as a function of nanoparticle size (from 10 nm to 100 nm in diameter) with and without the presence of an oxide layer are included in the Supporting Information (Figure A1.7).

We also found that the temperature evolution decay timescale ( $1/e$ ) had little dependence on the oxide thickness, indicating that the addition of even a thin oxide shell could be a highly effective means for controlling the lattice temperature of plasmonic NPs (see Figure A1.8). Previous work has demonstrated an increase in thermal energy transfer from Au NPs when encased by a silica shell.<sup>50</sup> This work revealed a dependence on the



silica shell thickness, but that the method of shell formation greatly impacted control of thermal energy transport because porous SiO<sub>2</sub> could allow penetration of solvent towards the Au core. In contrast, direct oxidation of the Al surface results in a compact native oxide layer that should prohibit formation of channels through which solvent can directly interface with the metal surface. Methods for replacing the native oxide layer on Al NPs in the solution phase have been demonstrated using fluoropolymer capping ligands<sup>78,79</sup> and oxidizing salts (aluminum iodate hexahydrate).<sup>80</sup> The thickness of the oxide layer could also be potentially tuned by introducing varied amounts of oxidizing agents.<sup>81</sup>

### **3.3 CONCLUSIONS**

We presented the first characterization of the photophysical dynamics of solution-synthesized plasmonic aluminum NPs, an emerging earth-abundant materials platform of interest for photocatalysis, optoelectronics, and sensing applications. We found that the response of Al NPs differs qualitatively from noble-metal NPs near the interband transitions, which are largely isolated from spectral changes to the intraband transitions, allowing for study of electron-electron thermalization dynamics. We found that induction timescales match predictions for electron-lattice relaxation processes in related materials, and energy transfer to the surrounding medium from large particles is comparable to the energy transfer rates predicted for much smaller particles. To understand this phenomenon, we investigated thermal energy transfer dynamics using a two-interface model to account for the presence of a native oxide layer on the aluminum NPs that mediates rapid thermal energy transfer out of the Al core. We propose that using surface modifications, including controlled oxidation, could be an effective tool to engineer heat transfer rates from large particles to the surrounding medium and could be an important strategy for applications in

which thermal management is critical for system performance and stability, including in photocatalytic and sensing applications.

### **3.4 METHODS**

#### *Aluminum Nanoparticles Synthesis.*

All solvents and reagents were purchased from Sigma-Aldrich. Aluminum NPs were prepared in an air-free environment (Schlenk line) following published procedures<sup>56</sup> with some modifications. In a typical procedure, 6.3 ml anhydrous tetrahydrofuran (THF), 6.3 ml anhydrous 1,4-dioxane and 3.3 ml dimethylethylamine alane solution were sequentially injected into a flask and stirred at 40°C. Then 0.4 ml of 3.3 mM titanium (IV) isopropoxide in toluene was subsequently added as a reaction catalyst, and the solution turned light brown. Five minutes later, 70 µl oleic acid in dioxane was injected. The reaction was completed after 1.5 hours, and the solution became greyish. The particles were washed twice using THF and twice using 2-propanol and finally redispersed in 2-propanol for measurements.

#### *Absorbance Measurement.*

Solution-phase steady-state absorption was measured using an Agilent Cary 5000 UV-Vis-NIR spectrophotometer. Particles in 2-propanol were measured in a 0.4 mL quartz cuvette over a wavelength range of 200 to 1000 nm.

#### *Finite-Difference Time-Domain Simulations.*

FDTD calculations were performed using commercial software (FDTD Solutions, Lumerical, Inc.). A total-field scattered-field (TFSF) wave source spanning a wavelength

range of 200 to 1200 nm was used as the excitation source. The nanostructures were modeled as aluminum icosahedra 93 nm in diameter possessing 3.7 nm aluminum oxide shells. The TFSF source is used to separate the simulation region into two distinct regions: one containing the total field (sum of incident and scattered fields) and the other region containing only the scattered field. Total-field and scattered-field monitors were placed at the edge of the simulation region to calculate the absorption and scattering cross-sections, respectively. Additionally, absorbing boundary conditions, in the form of perfectly matched layers (PMLs), were used to curb artificial reflections. Optical constants for aluminum used in the simulations were obtained from literature values.<sup>82</sup>

### *Ultrafast Laser Measurements.*

The ultrafast laser setup used for our experiments has been described previously.<sup>83</sup> Briefly, a regeneratively amplified, 1-kHz Ti:sapphire laser (Coherent Legend Elite) was used to generate excitation and probe pulses for transient absorption measurements. Ultrafast broadband probe pulses spanning 420-750 nm or 820-1100 nm were obtained by driving generation of a white-light supercontinuum in a 2-mm sapphire or rastered CaF<sub>2</sub> plate with ~100-200 nJ of the 800 nm laser fundamental. A ~1-mJ portion of the amplified output was up-converted by second-harmonic generation in a BBO crystal as a source of 400-nm pump pulses. Photophysical dynamics were examined at multiple fluences in the range of 10-100  $\mu\text{J}/\text{cm}^2$  to confirm linearity between excitation fluence and signal intensity.

The 400-nm pump beam was gently focused to a 2.14-mm beam diameter at the sample using a 50-cm focal length lens positioned approximately 26 cm from the sample. The pump beam crossed the probe at a small relative incident angle of  $\sim 10^\circ$  in the sample. The white-light probe was focused to  $\sim 100 \mu\text{m}$  within the excited region of the sample

using a parabolic mirror. All transient spectra were collected with linearly polarized pump and probe, with the relative polarization of the probe beam aligned at the “magic angle” (54.7°) to that of the pump beam by passing the white-light continuum through a wire-grid polarizer (Thorlabs) immediately before the sample.

The transmitted probe beam was aligned into a 0.3-m spectrograph (Acton-2360, Princeton Instruments) outfitted with a low-resolution grating (800-nm blaze, 150 lines/mm) with the center wavelength adjusted to either 600 or 1000 nm to acquire spectra in the visible or NIR regions, respectively. A CCD camera (Pixis-100BR, Princeton Instruments) was configured to detect the white-light continuum from the probe on each laser shot. Although the samples studied here did not fluoresce, they did scatter pump light considerably. For this reason, the pump and probe beams were chopped at one-half and one-quarter the repetition rate of the laser, respectively, in order to enable corrections to the transmitted probe intensity for scattered pump light according to Equation 3.4.

$$\Delta I_{trans} = \frac{I_{pump-probe} - I_{pump}}{I_{probe} - I_{background}} \quad 3.4$$

Transient spectra were then obtained by averaging scatter-corrected signals over 20,000-25,000 laser shots at each pump-probe time delay. The pump beam was retroreflected off of an Al corner cube mounted to a motorized translation stage (Newport); relative pulse time delay was controlled via stage position. The relative position of the stage, collection of spectra and chopper phases, and the calculation and averaging of transient absorption ( $-\log \Delta I_{trans}$ ) were accomplished with an in-house data acquisition program written in LABVIEW.

Transient data were “chirp-corrected” for group velocity dispersion prior to kinetic analysis. The instrument response of transient measurements (i.e. the cross correlation of excitation and probe pulses) was determined to be 250 fs FWHM based on the time dependence of coherent artifacts observed at time zero (Figure A1.4).

Samples of Aluminum NPs (Al-NPs) re-suspended in Isopropyl alcohol (IPA) after synthesis were too optically dense for laser measurements and were diluted ~10x with reagent grade (99.9% purity) IPA from Fischer Scientific. The diluted sample was placed in a 2-mm cuvette. The samples were slowly stirred continuously throughout data acquisition in order to ensure a homogeneous distribution of particles within the beam.

### 3.5 REFERENCES

- (1) Atwater, H. A.; Polman, A. Plasmonics for Improved Photovoltaic Devices. *Nat. Mater.* **2010**, *9* (3), 205–213. <https://doi.org/10.1038/nmat2629>.
- (2) Sau, T. K.; Rogach, A. L.; Jäckel, F.; Klar, T. A.; Feldmann, J. Properties and Applications of Colloidal Nonspherical Noble Metal Nanoparticles. *Adv. Mater.* **2010**, *22* (16), 1805–1825. <https://doi.org/10.1002/adma.200902557>.
- (3) Talapin, D. V.; Lee, J.-S.; Kovalenko, M. V.; Shevchenko, E. V. Prospects of Colloidal Nanocrystals for Electronic and Optoelectronic Applications. *Chem. Rev.* **2010**, *110* (1), 389–458. <https://doi.org/10.1021/cr900137k>.
- (4) Luo, X.; Morrin, A.; Killard, A. J.; Smyth, M. R. Application of Nanoparticles in Electrochemical Sensors and Biosensors. *Electroanalysis* **2006**, *18* (4), 319–326. <https://doi.org/10.1002/elan.200503415>.
- (5) Guo, S.; Zhang, S.; Sun, S. Tuning Nanoparticle Catalysis for the Oxygen Reduction Reaction. *Angew. Chem. Int. Ed.* **2013**, *52* (33), 8526–8544. <https://doi.org/10.1002/anie.201207186>.
- (6) Murray, R. W. Nanoelectrochemistry: Metal Nanoparticles, Nanoelectrodes, and Nanopores. *Chem. Rev.* **2008**, *108* (7), 2688–2720. <https://doi.org/10.1021/cr068077e>.
- (7) Zhang, X.; Chen, Y. L.; Liu, R.-S.; Tsai, D. P. Plasmonic Photocatalysis. *Rep. Prog. Phys.* **2013**, *76* (4), 046401. <https://doi.org/10.1088/0034-4885/76/4/046401>.
- (8) Clavero, C. Plasmon-Induced Hot-Electron Generation at Nanoparticle/Metal-Oxide Interfaces for Photovoltaic and Photocatalytic Devices. *Nat. Photonics* **2014**, *8* (2), 95–103. <https://doi.org/10.1038/nphoton.2013.238>.
- (9) Primo, A.; Corma, A.; García, H. Titania Supported Gold Nanoparticles as Photocatalyst. *Phys Chem Chem Phys* **2011**, *13* (3), 886–910. <https://doi.org/10.1039/C0CP00917B>.
- (10) Tian, Y.; Tatsuma, T. Mechanisms and Applications of Plasmon-Induced Charge Separation at TiO<sub>2</sub> Films Loaded with Gold Nanoparticles. *J. Am. Chem. Soc.* **2005**, *127* (20), 7632–7637. <https://doi.org/10.1021/ja042192u>.
- (11) Noguez, C. Surface Plasmons on Metal Nanoparticles: The Influence of Shape and Physical Environment. *J. Phys. Chem. C* **2007**, *111* (10), 3806–3819. <https://doi.org/10.1021/jp066539m>.
- (12) Kelly, K. L.; Coronado, E.; Zhao, L. L.; Schatz, G. C. The Optical Properties of Metal Nanoparticles: The Influence of Size, Shape, and Dielectric Environment. *J. Phys. Chem. B* **2003**, *107* (3), 668–677. <https://doi.org/10.1021/jp026731y>.
- (13) Link, S.; El-Sayed, M. A. Size and Temperature Dependence of the Plasmon Absorption of Colloidal Gold Nanoparticles. *J. Phys. Chem. B* **1999**, *103* (21), 4212–4217. <https://doi.org/10.1021/jp984796o>.
- (14) Eustis, S.; El-Sayed, M. A. Why Gold Nanoparticles Are More Precious than Pretty Gold: Noble Metal Surface Plasmon Resonance and Its Enhancement of the Radiative and Nonradiative Properties of Nanocrystals of Different Shapes. *Chem. Soc. Rev.* **2006**, *35* (3), 209–217. <https://doi.org/10.1039/B514191E>.
- (15) Jensen, T. R.; Malinsky, M. D.; Haynes, C. L.; Van Duyne, R. P. Nanosphere Lithography: Tunable Localized Surface Plasmon Resonance Spectra of Silver

- Nanoparticles. *J. Phys. Chem. B* **2000**, *104* (45), 10549–10556.  
<https://doi.org/10.1021/jp002435e>.
- (16) Link, S.; Wang, Z. L.; El-Sayed, M. A. Alloy Formation of Gold–Silver Nanoparticles and the Dependence of the Plasmon Absorption on Their Composition. *J. Phys. Chem. B* **1999**, *103* (18), 3529–3533. <https://doi.org/10.1021/jp990387w>.
- (17) Comin, A.; Manna, L. New Materials for Tunable Plasmonic Colloidal Nanocrystals. *Chem. Soc. Rev.* **2014**, *43* (11), 3957–3975.  
<https://doi.org/10.1039/C3CS60265F>.
- (18) Naik, G. V.; Shalaev, V. M.; Boltasseva, A. Alternative Plasmonic Materials: Beyond Gold and Silver. *Adv. Mater.* **2013**, *25* (24), 3264–3294.  
<https://doi.org/10.1002/adma.201205076>.
- (19) Guler, U.; Shalaev, V. M.; Boltasseva, A. Nanoparticle Plasmonics: Going Practical with Transition Metal Nitrides. *Mater. Today* **2015**, *18* (4), 227–237.  
<https://doi.org/10.1016/j.mattod.2014.10.039>.
- (20) Brown, A. M.; Sundararaman, R.; Narang, P.; Goddard, W. A.; Atwater, H. A. Ab Initio Phonon Coupling and Optical Response of Hot Electrons in Plasmonic Metals. *Phys. Rev. B* **2016**, *94* (7), 075120. <https://doi.org/10.1103/PhysRevB.94.075120>.
- (21) Ehrenreich, H.; Philipp, H. R.; Segall, B. Optical Properties of Aluminum. *Phys. Rev.* **1963**, *132* (5), 1918–1928. <https://doi.org/10.1103/PhysRev.132.1918>.
- (22) Knight, M. W.; King, N. S.; Liu, L.; Everitt, H. O.; Nordlander, P.; Halas, N. J. Aluminum for Plasmonics. *ACS Nano* **2014**, *8* (1), 834–840.  
<https://doi.org/10.1021/nm405495q>.
- (23) Chan, G. H.; Zhao, J.; Schatz, G. C.; Van Duyne, R. P. Localized Surface Plasmon Resonance Spectroscopy of Triangular Aluminum Nanoparticles. *J. Phys. Chem. C* **2008**, *112* (36), 13958–13963. <https://doi.org/10.1021/jp804088z>.
- (24) Lecarme, O.; Sun, Q.; Ueno, K.; Misawa, H. Robust and Versatile Light Absorption at Near-Infrared Wavelengths by Plasmonic Aluminum Nanorods. *ACS Photonics* **2014**, *1* (6), 538–546. <https://doi.org/10.1021/ph500096q>.
- (25) Brill, Thomas B.; Ren, Wu-Zhen; Yang, Vigor. Detailed Studies on the Flame Structure of Aluminum Particle Combustion. In *Solid Propellant Chemistry, Combustion, and Motor Interior Ballistics*; American Institute of Aeronautics and Astronautics, 2000; pp 689–722. <https://doi.org/10.2514/5.9781600866562.0689.0722>.
- (26) Hao, Q.; Wang, C.; Huang, H.; Li, W.; Du, D.; Han, D.; Qiu, T.; Chu, P. K. Aluminum Plasmonic Photocatalysis. *Sci. Rep.* **2015**, *5*.  
<https://doi.org/10.1038/srep15288>.
- (27) Zhou, L.; Zhang, C.; McClain, M. J.; Manjavacas, A.; Krauter, C. M.; Tian, S.; Berg, F.; Everitt, H. O.; Carter, E. A.; Nordlander, P.; et al. Aluminum Nanocrystals as a Plasmonic Photocatalyst for Hydrogen Dissociation. *Nano Lett.* **2016**, *16* (2), 1478–1484.  
<https://doi.org/10.1021/acs.nanolett.5b05149>.
- (28) Hartland, G. V. Optical Studies of Dynamics in Noble Metal Nanostructures. *Chem. Rev.* **2011**, *111* (6), 3858–3887. <https://doi.org/10.1021/cr1002547>.
- (29) Link, S.; El-Sayed, M. A. Shape and Size Dependence of Radiative, Non-Radiative and Photothermal Properties of Gold Nanocrystals. *Int. Rev. Phys. Chem.* **2000**, *19* (3), 409–453.
- (30) Rethfeld, B.; Kaiser, A.; Vicanek, M.; Simon, G. Ultrafast Dynamics of Nonequilibrium Electrons in Metals under Femtosecond Laser Irradiation. *Phys. Rev. B*

- 2002**, 65 (21), 214303. <https://doi.org/10.1103/PhysRevB.65.214303>.
- (31) Nie, S.; Wang, X.; Park, H.; Clinite, R.; Cao, J. Measurement of the Electronic Gruneisen Constant Using Femtosecond Electron Diffraction. *Phys. Rev. Lett.* **2006**, 96 (2), 025901. <https://doi.org/10.1103/PhysRevLett.96.025901>.
- (32) Pomfret, M. B.; Brown, D. J.; Epshteyn, A.; Purdy, A. P.; Owrutsky, J. C. Electrochemical Template Deposition of Aluminum Nanorods Using Ionic Liquids. *Chem. Mater.* **2008**, 20 (19), 5945–5947. <https://doi.org/10.1021/cm801983w>.
- (33) Su, M.-N.; Dongare, P. D.; Chakraborty, D.; Zhang, Y.; Yi, C.; Wen, F.; Chang, W.-S.; Nordlander, P.; Sader, J. E.; Halas, N. J.; et al. Optomechanics of Single Aluminum Nanodisks. *Nano Lett.* **2017**, 17 (4), 2575–2583. <https://doi.org/10.1021/acs.nanolett.7b00333>.
- (34) Stietz, F.; Bosbach, J.; Wenzel, T.; Vartanyan, T.; Goldmann, A.; Träger, F. Decay Times of Surface Plasmon Excitation in Metal Nanoparticles by Persistent Spectral Hole Burning. *Phys. Rev. Lett.* **2000**, 84 (24), 5644–5647. <https://doi.org/10.1103/PhysRevLett.84.5644>.
- (35) Bosbach, J.; Hendrich, C.; Vartanyan, T.; Stietz, F.; Träger, F. Spectral Hole Burning in Absorption Profiles of Metal Nanoparticles Prepared by Laser Assisted Growth. *Eur. Phys. J. - At. Mol. Opt. Plasma Phys.* **2001**, 16 (1), 213–217. <https://doi.org/10.1007/s100530170095>.
- (36) Voisin, C.; Christofilos, N.; Del Fatti, N.; Vallee, F.; Prevel, B.; Cottancin, E.; Lerme, M.; Broyer, M. Size-Dependent Electron-Electron Interactions in Metal Nanoparticles. *Phys. Rev. Lett.* **2000**, 85 (10), 2200–2203.
- (37) Bigot, J.-Y.; Halté, V.; Merle, J.-C.; Daunois, A. Electron Dynamics in Metallic Nanoparticles. *Chem. Phys.* **2000**, 251 (1–3), 181–203. [https://doi.org/10.1016/S0301-0104\(99\)00298-0](https://doi.org/10.1016/S0301-0104(99)00298-0).
- (38) Hodak, J. H.; Henglein, A.; Hartland, G. V. Size Dependent Properties of Au Particles: Coherent Excitation and Dephasing of Acoustic Vibrational Modes. *J. Chem. Phys.* **1999**, 111 (18), 8613–8621. <https://doi.org/10.1063/1.480202>.
- (39) Newhouse, R. J.; Wang, H.; Hensel, J. K.; Wheeler, D. A.; Zou, S.; Zhang, J. Z. Coherent Vibrational Oscillations of Hollow Gold Nanospheres. *J. Phys. Chem. Lett.* **2011**, 2 (3), 228–235. <https://doi.org/10.1021/jz101716h>.
- (40) Hu, M.; Hartland, G. V. Heat Dissipation for Au Particles in Aqueous Solution: Relaxation Time versus Size. *J. Phys. Chem. B* **2002**, 106 (28), 7029–7033. <https://doi.org/10.1021/jp020581+>.
- (41) Vallee, F. Ultrafast Non-Equilibrium Electron Dynamics in Metal Nanoparticles. In *Non-Equilibrium Dynamics of Semiconductors and Nanostructures*; Tsien, K.-T., Ed.; CRC Press, 2005; pp 101–142. <https://doi.org/10.1201/9781420027259.ch5>.
- (42) Ge, Z.; Kang, Y.; Taton, T. A.; Braun, P. V.; Cahill, D. G. Thermal Transport in Au-Core Polymer-Shell Nanoparticles. *Nano Lett.* **2005**, 5 (3), 531–535. <https://doi.org/10.1021/nl047944x>.
- (43) Dowgiallo, A.-M.; Knappenberger, K. L. Ultrafast Electron–Phonon Coupling in Hollow Gold Nanospheres. *Phys. Chem. Chem. Phys.* **2011**, 13 (48), 21585. <https://doi.org/10.1039/c1cp22743b>.
- (44) Wheeler, D. A.; Green, T. D.; Wang, H.; Fernández-López, C.; Liz-Marzán, L.; Zou, S.; Knappenberger, K. L.; Zhang, J. Z. Optical Properties and Coherent Vibrational Oscillations of Gold Nanostars. *Chem. Phys. Lett.* **2012**, 543, 127–132.



- <https://doi.org/10.1016/j.cplett.2012.06.058>.
- (45) Dacosta Fernandes, B.; Le Beulze, A.; Moroté, F.; Oberlé, J.; Tréguer-Delapierre, M.; Burgin, J.; Langot, P. Electron–Phonon Scattering in 2D Silver Nanotriangles. *J. Phys. Chem. C* **2013**, *117* (42), 22041–22045. <https://doi.org/10.1021/jp406357p>.
- (46) Sando, G. M.; Berry, A. D.; Campbell, P. M.; Baronavski, A. P.; Owrutsky, J. C. Surface Plasmon Dynamics of High-Aspect-Ratio Gold Nanorods. *Plasmonics* **2007**, *2* (1), 23–29. <https://doi.org/10.1007/s11468-006-9021-8>.
- (47) Burda, C.; Chen, X.; Narayanan, R.; El-Sayed, M. A. Chemistry and Properties of Nanocrystals of Different Shapes. *Chem. Rev.* **2005**, *105* (4), 1025–1102. <https://doi.org/10.1021/cr030063a>.
- (48) Huang, W.; Qian, W.; El-Sayed, M. A.; Ding, Y.; Wang, Z. L. Effect of the Lattice Crystallinity on the Electron–Phonon Relaxation Rates in Gold Nanoparticles. *J. Phys. Chem. C* **2007**, *111* (29), 10751–10757. <https://doi.org/10.1021/jp0738917>.
- (49) Ge, Z.; Cahill, D. G.; Braun, P. V. AuPd Metal Nanoparticles as Probes of Nanoscale Thermal Transport in Aqueous Solution. *J. Phys. Chem. B* **2004**, *108* (49), 18870–18875. <https://doi.org/10.1021/jp048375k>.
- (50) Hu, M.; Wang, X.; Hartland, G. V.; Salgueiriño-Maceira, V.; Liz-Marzán, L. M. Heat Dissipation in Gold–Silica Core-Shell Nanoparticles. *Chem. Phys. Lett.* **2003**, *372* (5), 767–772. [https://doi.org/10.1016/S0009-2614\(03\)00506-2](https://doi.org/10.1016/S0009-2614(03)00506-2).
- (51) Du, L.; Furube, A.; Yamamoto, K.; Hara, K.; Katoh, R.; Tachiya, M. Plasmon-Induced Charge Separation and Recombination Dynamics in Gold–TiO<sub>2</sub> Nanoparticle Systems: Dependence on TiO<sub>2</sub> Particle Size. *J. Phys. Chem. C* **2009**, *113* (16), 6454–6462. <https://doi.org/10.1021/jp810576s>.
- (52) Maier, G. P.; Rapp, M. V.; Waite, J. H.; Israelachvili, J. N.; Butler, A. Adaptive Synergy between Catechol and Lysine Promotes Wet Adhesion by Surface Salt Displacement. *Science* **2015**, *349* (6248), 628–632. <https://doi.org/10.1126/science.aab0556>.
- (53) Du, L.; Furube, A.; Hara, K.; Katoh, R.; Tachiya, M. Ultrafast Plasmon Induced Electron Injection Mechanism in Gold–TiO<sub>2</sub> Nanoparticle System. *J. Photochem. Photobiol. C Photochem. Rev.* **2013**, *15*, 21–30. <https://doi.org/10.1016/j.jphotochemrev.2012.11.001>.
- (54) Furube, A.; Du, L.; Hara, K.; Katoh, R.; Tachiya, M. Ultrafast Plasmon-Induced Electron Transfer from Gold Nanodots into TiO<sub>2</sub> Nanoparticles. *J. Am. Chem. Soc.* **2007**, *129* (48), 14852–14853. <https://doi.org/10.1021/ja076134v>.
- (55) Link, S.; El-Sayed, M. A. Optical Properties and Ultrafast Dynamics of Metallic Nanocrystals. *Annu. Rev. Phys. Chem.* **2003**, *54* (1), 331–366. <https://doi.org/10.1146/annurev.physchem.54.011002.103759>.
- (56) McClain, M. J.; Schlather, A. E.; Ringe, E.; King, N. S.; Liu, L.; Manjavacas, A.; Knight, M. W.; Kumar, I.; Whitmire, K. H.; Everitt, H. O.; et al. Aluminum Nanocrystals. *Nano Lett.* **2015**, *15* (4), 2751–2755. <https://doi.org/10.1021/acs.nanolett.5b00614>.
- (57) Tian, S.; Neumann, O.; McClain, M. J.; Yang, X.; Zhou, L.; Zhang, C.; Nordlander, P.; Halas, N. J. Aluminum Nanocrystals: A Sustainable Substrate for Quantitative SERS-Based DNA Detection. *Nano Lett.* **2017**. <https://doi.org/10.1021/acs.nanolett.7b02338>.
- (58) Katayama, T.; Setoura, K.; Werner, D.; Miyasaka, H.; Hashimoto, S. Picosecond-

- to-Nanosecond Dynamics of Plasmonic Nanobubbles from Pump–Probe Spectral Measurements of Aqueous Colloidal Gold Nanoparticles. *Langmuir* **2014**, *30* (31), 9504–9513. <https://doi.org/10.1021/la500663x>.
- (59) Ziegler, T.; Hendrich, C.; Hubenthal, F.; Vartanyan, T.; Träger, F. Dephasing Times of Surface Plasmon Excitation in Au Nanoparticles Determined by Persistent Spectral Hole Burning. *Chem. Phys. Lett.* **2004**, *386* (4–6), 319–324. <https://doi.org/10.1016/j.cplett.2004.01.001>.
- (60) Zhao, T.; Jiang, X.-F.; Gao, N.; Li, S.; Zhou, N.; Ma, R.; Xu, Q.-H. Solvent-Dependent Two-Photon Photoluminescence and Excitation Dynamics of Gold Nanorods. *J. Phys. Chem. B* **2013**, *117* (49), 15576–15583. <https://doi.org/10.1021/jp405929w>.
- (61) Sun, C.-K.; Vallée, F.; Acioli, L. H.; Ippen, E. P.; Fujimoto, J. G. Femtosecond-Tunable Measurement of Electron Thermalization in Gold. *Phys. Rev. B* **1994**, *50* (20), 15337–15348. <https://doi.org/10.1103/PhysRevB.50.15337>.
- (62) Del Fatti, N.; Voisin, C.; Achermann, M.; Tzortzakis, S.; Christofilos, D.; Vallée, F. Nonequilibrium Electron Dynamics in Noble Metals. *Phys. Rev. B* **2000**, *61* (24), 16956–16966. <https://doi.org/10.1103/PhysRevB.61.16956>.
- (63) Stoll, T.; Maioli, P.; Crut, A.; Rodal-Cedeira, S.; Pastoriza-Santos, I.; Vallée, F.; Del Fatti, N. Time-Resolved Investigations of the Cooling Dynamics of Metal Nanoparticles: Impact of Environment. *J. Phys. Chem. C* **2015**, *119* (22), 12757–12764. <https://doi.org/10.1021/acs.jpcc.5b03231>.
- (64) Maillard, M.; Pileni, M.-P.; Link, S.; El-Sayed, M. A. Picosecond Self-Induced Thermal Lensing from Colloidal Silver Nanodisks. *J. Phys. Chem. B* **2004**, *108* (17), 5230–5234. <https://doi.org/10.1021/jp049943z>.
- (65) Hodak, J.; Martini, I.; Harland, G. Spectroscopy and Dynamics of Nanometer-Sized Noble Metal Particles. *J. Phys. Chem. B* **1998**, *102* (36), 6958–6967. <https://doi.org/10.1021/jp9809787>.
- (66) Haynes, W.M. (ed.). *CRC Handbook of Chemistry and Physics*, 95th ed.; CRC Press: Oakville, 2014.
- (67) Wilson, O. M.; Hu, X.; Cahill, D. G.; Braun, P. V. Colloidal Metal Particles as Probes of Nanoscale Thermal Transport in Fluids. *Phys. Rev. B* **2002**, *66* (22). <https://doi.org/10.1103/PhysRevB.66.224301>.
- (68) Hartland, G. V.; Hu, M.; Sader, J. E. Softening of the Symmetric Breathing Mode in Gold Particles by Laser-Induced Heating. *J. Phys. Chem. B* **2003**, *107* (30), 7472–7478. <https://doi.org/10.1021/jp0276092>.
- (69) Simmons, G.; Wang, H. *Single Crystal Elastic Constants and Calculated Aggregate Properties: A Handbook*; M.I.T. Press, 1971.
- (70) Ma, W.; Wang, H.; Zhang, X.; Wang, W. Study of the Electron–Phonon Relaxation in Thin Metal Films Using Transient Thermoreflectance Technique. *Int. J. Thermophys.* **2013**, *34* (12), 2400–2415. <https://doi.org/10.1007/s10765-011-1063-2>.
- (71) Juvé, V.; Scardamaglia, M.; Maioli, P.; Crut, A.; Merabia, S.; Joly, L.; Del Fatti, N.; Vallée, F. Cooling Dynamics and Thermal Interface Resistance of Glass-Embedded Metal Nanoparticles. *Phys. Rev. B* **2009**, *80* (19). <https://doi.org/10.1103/PhysRevB.80.195406>.
- (72) Plech, A.; Kotaidis, V.; Grésillon, S.; Dahmen, C.; von Plessen, G. Laser-Induced Heating and Melting of Gold Nanoparticles Studied by Time-Resolved x-Ray Scattering. *Phys. Rev. B* **2004**, *70* (19). <https://doi.org/10.1103/PhysRevB.70.195423>.

- (73) Muskens, O. L.; Del Fatti, N.; Vallée, F. Femtosecond Response of a Single Metal Nanoparticle. *Nano Lett.* **2006**, *6* (3), 552–556. <https://doi.org/10.1021/nl0524086>.
- (74) Lyeo, H.-K.; Cahill, D. G. Thermal Conductance of Interfaces between Highly Dissimilar Materials. *Phys. Rev. B* **2006**, *73* (14), 144301. <https://doi.org/10.1103/PhysRevB.73.144301>.
- (75) Ge, Z.; Cahill, D. G.; Braun, P. V. Thermal Conductance of Hydrophilic and Hydrophobic Interfaces. *Phys. Rev. Lett.* **2006**, *96* (18), 186101. <https://doi.org/10.1103/PhysRevLett.96.186101>.
- (76) Gundrum, B. C.; Cahill, D. G.; Averbach, R. S. Thermal Conductance of Metal-Metal Interfaces. *Phys. Rev. B* **2005**, *72* (24), 245426. <https://doi.org/10.1103/PhysRevB.72.245426>.
- (77) Cahill, D. G.; Ford, W. K.; Goodson, K. E.; Mahan, G. D.; Majumdar, A.; Maris, H. J.; Merlin, R.; Phillpot, S. R. Nanoscale Thermal Transport. *J. Appl. Phys.* **2002**, *93* (2), 793–818. <https://doi.org/10.1063/1.1524305>.
- (78) Kaplowitz, D. A.; Jian, G.; Gaskell, K.; Ponce, A.; Shang, P.; Zachariah, M. R. Aerosol Synthesis and Reactivity of Thin Oxide Shell Aluminum Nanoparticles via Fluorocarboxylic Acid Functional Coating. *Part. Part. Syst. Charact.* **2013**, *30* (10), 881–887. <https://doi.org/10.1002/ppsc.201300112>.
- (79) Jouet, R. J.; Carney, J. R.; Granholm, R. H.; Sandusky, H. W.; Warren, A. D. Preparation and Reactivity Analysis of Novel Perfluoroalkyl Coated Aluminium Nanocomposites. *Mater. Sci. Technol.* **2006**, *22* (4), 422–429. <https://doi.org/10.1179/174328406X84003>.
- (80) Smith, D. K.; Unruh, D. K.; Pantoya, M. L. Replacing the Al<sub>2</sub>O<sub>3</sub> Shell on Al Particles with an Oxidizing Salt, Aluminum Iodate Hexahydrate. Part II: Synthesis. *J. Phys. Chem. C* **2017**, *121* (41), 23192–23199. <https://doi.org/10.1021/acs.jpcc.7b05805>.
- (81) Shavel, A.; Rodríguez-González, B.; Spasova, M.; Farle, M.; Liz-Marzán, L. M. Synthesis and Characterization of Iron/Iron Oxide Core/Shell Nanocubes. *Adv. Funct. Mater.* **2007**, *17* (18), 3870–3876. <https://doi.org/10.1002/adfm.200700494>.
- (82) Palik, E. D. *Handbook of Optical Constants of Solids*; Academic press, 1998; Vol. 3.
- (83) Molloy, M. S.; Snyder, J. A.; Bragg, A. E. Structural and Solvent Control of Nonadiabatic Photochemical Bond Formation: Photocyclization of *o*-Terphenyl in Solution. *J. Phys. Chem. A* **2014**, *118* (22), 3913–3925. <https://doi.org/10.1021/jp501988g>.

## Chapter 4

# Size and Surface-Dependent Photoresponses of Solution-Processed Aluminum Nanoparticles

### 4.0 ABSTRACT

Plasmonic aluminum nanoparticles have emerged as an exciting new materials platform, due to the high natural abundance of aluminum, their ability to be synthesized in the solution phase, and the potential of these materials to be used for photocatalysis and sensing. However, the photothermal properties of solution-processed aluminum nanoparticles, particularly how phonon energy transfer depends on particle size and surface properties, are critical for practical applications and are currently unexplored. Here, we use transient absorption spectroscopy, in combination with simulations of phonon and thermal energy dissipation, to investigate the photoresponses of aluminum nanoparticles of various diameters (54, 85, 121, and 144 nm) suspended in 2-propanol. Fast thermal transfer rates to the solvent (170-280 ps) are observed for particles of all sizes and are facilitated by native oxide coverage, as verified with a two-interface thermal energy-transfer model. Size-dependent phonon “breathing”/vibrational modes are also observed as oscillations in total cross-section. We find that both the oscillation frequency and damping rate increase as the diameter of the particles decreases. Based on results of finite element calculations, we attribute the damping strength and oscillation period observed to a combination of the

non-crystalline nature of the native oxide shell and the presence of surface-bound ligands, both of which increase the vibrational mode damping rates relative to bare Al and Al particles with a bare crystalline oxide shell. These insights should guide future work on controlling energy transfer through the use of size- and surface-tuning in sustainable aluminum nanomaterials systems for applications in catalysis and sensing.

#### **4.1 INTRODUCTION**

Plasmonic nanomaterials continue to attract considerable interest for novel applications in optoelectronics, sensing, and catalysis<sup>1-6</sup> that take advantage of the concentration of electromagnetic fields of light and/or electronic excitation associated with localized surface plasmon resonances (LSPRs). There is particular interest in using plasmonic nanoparticles as sensitizers for photocatalysis.<sup>7,8</sup> Specifically, it has been demonstrated that hot electrons in plasmonic nanoparticles originating from optical LSPR excitation can overcome the Schottky barrier with an adjoining material to generate reactive conduction-band electrons for catalysis<sup>9,10</sup> with an efficiency that depends on the electronic and thermal relaxation dynamics of the nanoparticle. The photothermal properties of plasmonic nanoparticles are also of great interest for their use in applications such as plasmonic photothermal therapies.<sup>11,12</sup> The finite thermal conductivity of metal nanoparticles allows them to be utilized as extremely efficient heat sources through far field illumination.<sup>13</sup> Optically resonant excitation of the LSPR results in localized heating around the particle with large temperature gradients. Not only can this thermal energy be used to destroy biological tissue (e.g. cancer cells),<sup>14,15</sup> these temperature gradients have been used experimentally to direct motion of nearby objects through thermophoretic

forces.<sup>16,17</sup> The impacts of material architecture, interfaces, and the chemical environment on electronic and lattice-energy dissipation pathways are critical to the efficacy of these applications.

The LSPR underlying the photoresponses of these materials is a coherent collective response of carriers (i.e. electrons) to electromagnetic radiation that is tunable according to particle size, shape and composition. Noble metal particles such as gold and silver have been studied extensively over the years both in efforts to elucidate fundamental properties of plasmonic nanomaterials and in the development of optical applications.<sup>18–21</sup> However, largescale deployment of materials, devices or chemical applications based on precious metals has the potential to be costly and also limited by the relatively low elemental abundance of precious metals.<sup>22–24</sup> In recent years, aluminum has emerged as an inexpensive, earth-abundant alternative to noble metals for plasmonic nanomaterials.<sup>25–28</sup> Yet, much less is known about the plasmonic responses of Al nanomaterials, including the impact of native oxides on their photothermal and photoacoustic behaviors as well as their charge-transfer potential for catalytic sensitization. A firm understanding of the photophysical properties of these particles and how they vary with size, shape, and chemical environment is essential for the development of Al-based plasmonic material applications.

There are currently few published studies of the photophysical properties of plasmonic Al nanomaterials in the literature. Su *et al.* have investigated the electronic relaxation behaviors of single Al nanodisks.<sup>29,30</sup> Due to the polycrystalline nature of the Al nanodisks, fast (sub-ps) electron-phonon relaxation timescales were observed, and damping of phonon vibrations was found to be largely determined by the presence of

intrinsic lattice defects and rough surfaces with minimal dependence on the substrate environment. The oxide shell was identified as providing an interface with the Al core that trapped and de-trapped carriers with the potential to enable long hot-carrier lifetimes. We recently reported on the photothermal energy-transfer dynamics of a different Al nanomaterial: solution-processed, single-crystal aluminum nanoparticles (~100 nm diameter) suspended in 2-propanol (IPA).<sup>31</sup> We observed a rapid (sub-ps to ps) decrease in probe light transmission broadly across the visible and near-IR following sample excitation at 400 nm, which we attributed to a combination of electron-phonon energy transfer followed by changes in the scattering cross-section of particles as a result of electron-to-phonon energy transfer and lattice expansion. Periodic modulation in probe transmission across the visible and near-IR associated with coherent phonon/acoustic vibrations were resolved with a period of ~14 ps. These were followed by a slow increase in light transmission observed on a timescale of ~250 ps, ultimately leading to a net increase in light transmission by 1 ns that we attributed to a decrease in the surrounding solvent dielectric constant due to thermal energy transfer from the Al particle. The latter assignment was supported with simulations of thermal-energy transfer: A simple two-interface (Al/Al oxide/solvent) model revealed that the fast local heating of the solvent is facilitated by the intermediary aluminum oxide, which quickly and efficiently mediates thermal energy transfer from the Al core to the surrounding medium. Indeed, from the model it can be seen that oxide-coated particles cool on timescales that are roughly an order of magnitude faster than particles without an oxide layer; e.g. a 100 nm particle with an oxide layer will cool on a comparable timescale to that of a 10 nm particle without an oxide layer.

Here we present an extended study of Al nanoparticles to investigate in more detail the impacts of both particle size and surface composition on their photothermal properties. In particular, we examine the size-dependence of the frequencies and damping rates for the acoustic phonon vibrations that are activated by lattice expansion.<sup>32</sup> These high frequency acoustic vibrations can be measured using techniques including transient absorption spectroscopy (as conducted in our work) and Raman scattering spectroscopy.<sup>33,34</sup> The damped oscillations in time-dependent signals are not only sensitive to the mechanical properties of the plasmonic particles, but also how these resonators interact with the surrounding environment.<sup>35</sup> There is considerable precedent in the literature regarding this sensitivity: Studies of acoustic properties of alloyed and core-shell multi-compositional metal nanoparticles<sup>36-38</sup> have revealed that both composition and mechanical interfaces are important factors that influence energy transfer. The vibrational mode frequencies of metal-dielectric core-shell particles have been found to be strongly affected by their amorphous oxide shells.<sup>39</sup> Additionally, surface ligands affect mechanical coupling between the metal, dielectric, and surrounding solvent; this has been demonstrated in recent studies on core-shell semiconductor quantum dots<sup>40</sup> in which accurate interpretation of the vibrational resonances are obtained by including the capping ligands in an elastic continuum model. Inhomogeneous broadening in nanoparticle solutions can also accelerate the ensemble decay dynamics.<sup>41</sup> Thus, the specific structure, composition, and surface functionalization of plasmonic nanoparticles are all important factors that dictate the details of their energy-dissipation dynamics. Examinations of the nanomechanical resonances associated with solution-phase aluminum nanoparticles are currently lacking and would provide insight important for developing mass sensing applications, for example.<sup>42,43</sup>



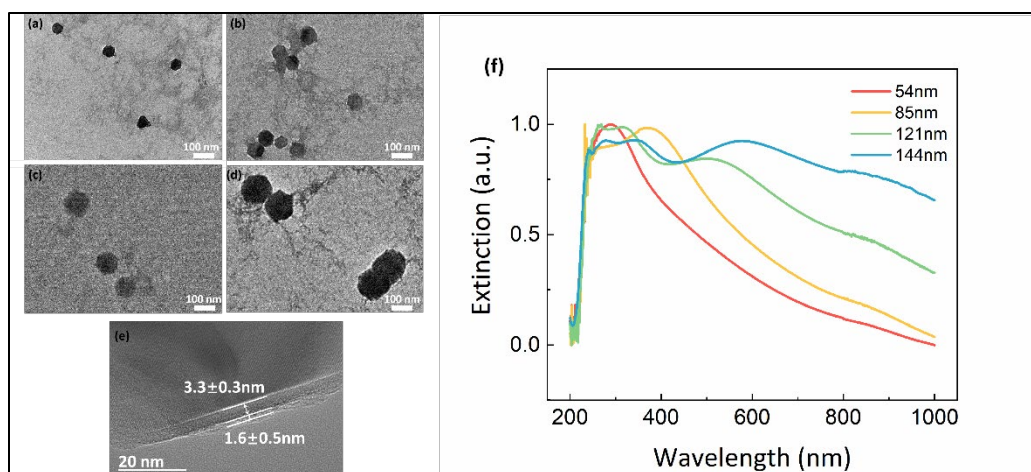
Here we demonstrate strong sensitivity of phonon breathing mode frequency and damping with particle size, with the oscillation frequency and homogeneous damping rate decreasing with increasing particle diameter. We substantiate these experimental findings by employing finite-element calculations using continuum mechanics theory. We systematically demonstrate how the oxide shell composition and presence of the ligand shell affect phonon damping dynamics with particle size and find that the surface character of the single-crystal Al particles is the dominant factor in determining the homogeneous damping rates.

## **4.2 RESULTS AND DISCUSSION**

Colloidal Al NPs were synthesized using solution-processed methods based on modifications of published procedures;<sup>31,44</sup> details are provided in the Methods section. By delaying the addition time of the capping agent, we were able to controllably tune the size of the particles. We prepared four samples with varied particle dimensions in our study and verified their sizes using transmission electron microscopy (TEM), as shown in Figure 1(a)-(d). The majority of the particles exhibit icosahedral shapes, and the four samples we studied have average particle diameters of approximately 54 nm, 85 nm, 121 nm, and 144 nm. High resolution TEM images, shown in Figure 1(e) and in Figure A2.2(a), clearly indicate the presence of an oxide layer (thickness of  $3.3 \pm 0.3$  nm) and an organic ligand layer (thickness of  $1.6 \pm 0.5$  nm) on the surface of the Al particles. We also conducted X-ray photoelectron spectroscopy and Fourier transform infrared spectroscopy (Figures A2.2(b) and A2.3) measurements to further confirm, respectively, the composition of the oxide shell and the identity of the ligands bound to the surfaces of the particles. We used UV-Vis-NIR spectrophotometry to measure the extinction spectra of the four particle

samples in IPA. The particles show tunable dipolar localized surface plasmon resonance (LSPR) peaks with wavelengths that range from 288 nm to 577 nm as the particle size increases (Figure 4.1(f)). Higher order modes also appear in the spectra at wavelengths below 400 nm with increasing particle size. The broad shoulder in all spectra near 850 nm in wavelength corresponds to the aluminum interband transition.

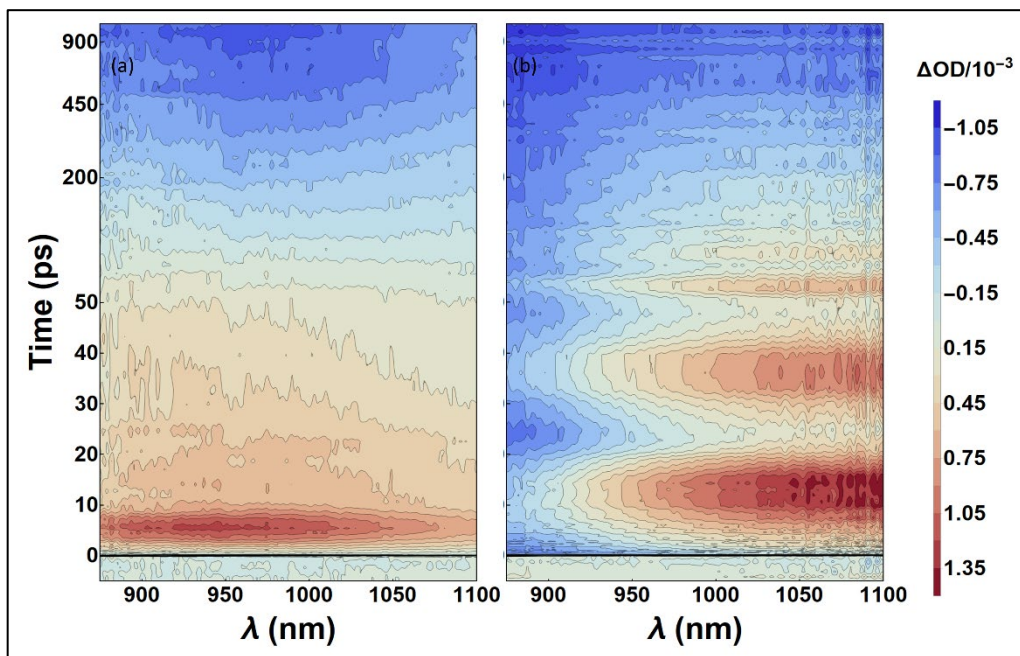
Figures 4.2(a) and 4.2(b) present contour plots of transient absorption spectra collected for 54-nm and 144-nm Al nanoparticles, respectively, excited near the peak of their plasmon resonances (specifically, 400 nm excitation for 54-, 85- and 121-nm



**Figure 4.1** (a)-(d) TEM image of Al NPs with mean diameters of 54 nm, 85 nm, 121 nm and 144 nm. (e) High resolution TEM image showing both the surface oxide (thickness of  $3.3 \pm 0.3$  nm) and organic ligand shell (thickness of  $1.6 \pm 0.5$  nm) on an Al NP. (f) UV-Vis-NIR spectrophotometric extinction spectra for Al NP solutions with these four different mean diameters as indicated in the legend.

particles, and 580 nm excitation for 144-nm particles). Here, positive absorption (shaded red) corresponds with decreased probe light transmission, whereas negative signal (shaded blue) corresponds with increased probe transmission. Time delays are reported along a split linear/log axis in order to highlight spectral dynamics across all relevant timescales;

time zero is clear from the sharp coherent, nonlinear pulse interaction with IPA (what appears as a dark line in Figures 2(a) and 2(b)) that occurs prior to signal induction.



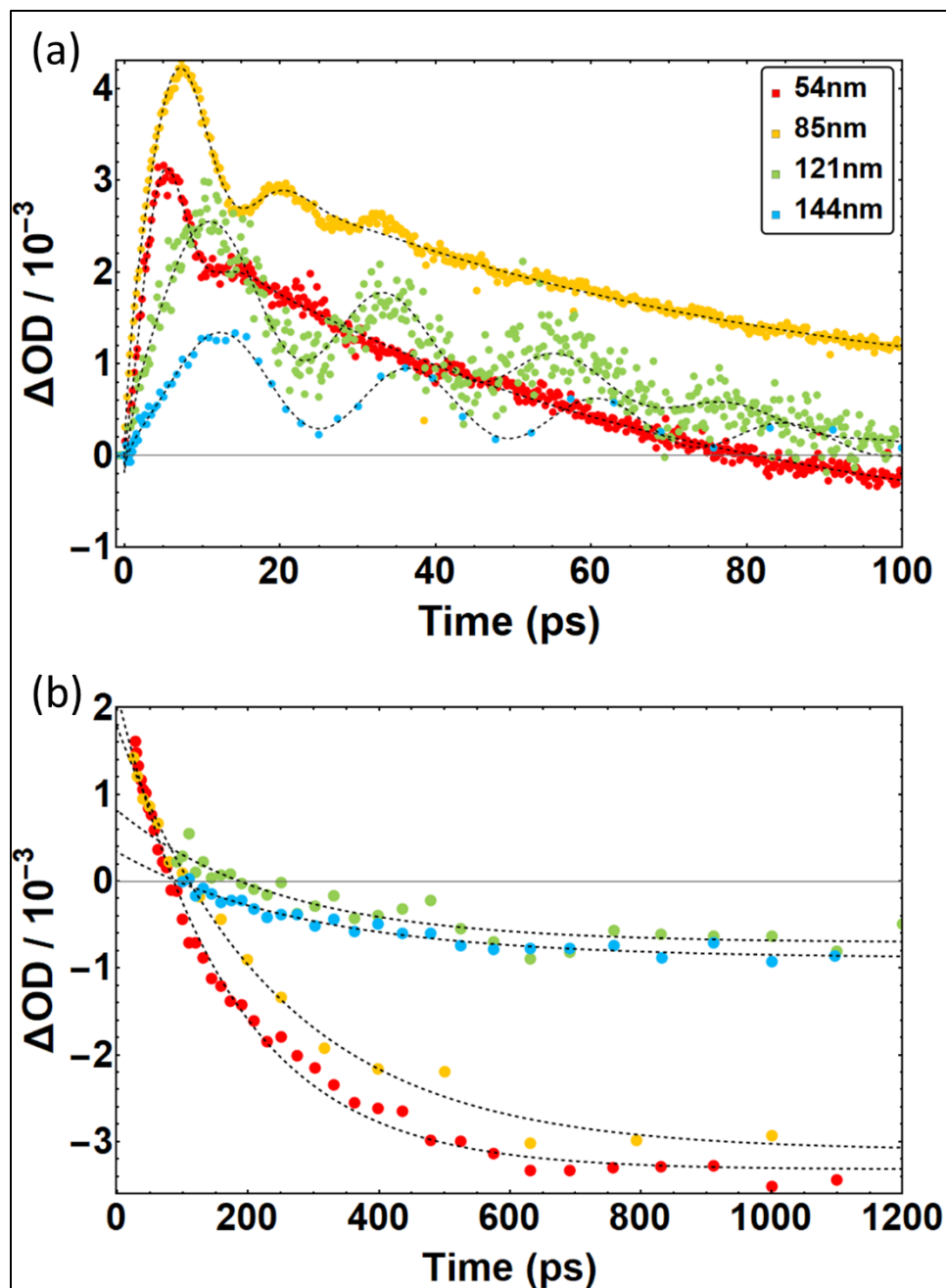
**Figure 4.2.** Contour plots of transient spectra (plotted in terms of change in optical density,  $\Delta OD$ ) collected for particles with a)  $\sim 54$  nm and b)  $\sim 144$  nm diameters. Transients are plotted on a split linear-log timescale to highlight spectral evolution on timescales up to  $\sim 1$  ns after excitation. The contour for the smallest particles is scaled by 0.25 for comparison.

The time-dependent spectral evolution observed with the particle ensembles of different sizes are qualitatively similar to what we have observed previously with  $\sim 100$ -nm-diameter particles:<sup>31</sup> In all cases a slow induction to a positive  $\Delta OD$  (i.e. a decreased probe light transmission) occurs at wavelengths above 950 nm, peaking between 5 and 15 ps after excitation. This positive signal decays to  $\Delta OD = 0$  by  $\sim 100$ -150 ps and continues to decay to a negative value (i.e. increased light transmission) within a nanosecond. We have previously assigned the initial positive  $\Delta OD$  increase to an enhanced scattering cross-section due to lattice expansion that follows electron-to-phonon energy transfer; in

contrast, the increased light transmission ( $\Delta OD < 0$ ) observed at 1 ns is attributed to a change in the solvent refractive index due to local heating that alters both the scattering and absorption cross-sections of the nanoparticles, as modelled previously with FDTD simulations.<sup>31</sup> For larger particles we observe a rapid bleach near the aluminum interband electron transition that peaks below 900 nm in wavelength; similar behavior was observed for 100-nm particles studied previously.

Although the changes in optical transmission with probe delay remain qualitatively similar across all sizes studied, it is clear from Figure 2 that the presence of signal modulations associated with acoustic lattice modes (i.e. coherent phonon vibrations), which are initiated by rapid electron-to-phonon energy transfer, is highly dependent on particle sample. For example, while a highly recurrent oscillatory response is observed after excitation of the 144-nm particles (Figure 2(b)), vibrations associated with the 54-nm particles are strongly damped (Figure 2(a)). While data for each of the samples was collected out to 1 ns to track dynamics of photothermal energy transfer from nanoparticle to solvent, data sets containing a higher number of time delays through 100 ps were also collected in order to carefully characterize the time dependence of these phonon vibrations. Figure 3(a) plots the time dependence of transient cuts through the near-IR absorption for all particle sizes studied, illustrating the differences in acoustic particle vibrations with size both in terms of phonon frequency and overall damping. For the larger particles studied (~121 and 144 nm), signal oscillations recur repeatedly through the first 100 ps that follow excitation. In samples of particles that have a diameter of 100 nm or smaller, the vibrations are apparent but are highly damped. Finally, as seen in Figures 2 and 3(a), the time delay at which the signal peaks (i.e. when the transmission is minimized) increases

monotonically with particle size.



**Figure 4.3.** (a): Time-dependent changes in near-IR extinction (integrated 1000-1075 nm) observed for particles of each size. Fits are shown as dashed lines; fitting functions are described in the text. (b): Time-dependent signals for the same samples plotted on timescales relevant to thermal energy transfer to solvent.

The functional form used to fit the traces from TA data plotted in Figure 3(a) is given in Equation 1.

$$I(t) = a_r \left(1 - e^{-t/\tau_r}\right) + a_p e^{-t/T_1} e^{-t^2/(T_2^*)^2} \cos\left(\frac{2\pi t}{\tau_p} + p\right) + a_d e^{-t/\tau_d} + c \quad 4.1$$

Fitting function parameters include: an initial increase in cross section (induction time  $\tau_r$ ); a damped periodic signal oscillation with period  $\tau_p$  and phase  $p$ ; oscillation damping with both homogeneous ( $T_1$ ) and inhomogeneous ( $T_2^*$ ) contributions; a slow cross-section decay (lifetime  $\tau_d$ ); and corresponding scaling constants ( $a_r$ ,  $a_d$ , and  $a_p$ ) as well as a constant offset ( $c$ ) that accounts for the reversal in light transmission arising from changes in the local solvent dielectric (or refractive index) due to thermal energy transfer from the nanoparticle to the surrounding solvent on longer timescales. The thermalization lifetime,  $\tau_d$ , could not be determined reliably from data sets extending only to 100 ps, the duration most useful for accurately determining the periods of the acoustic vibrations. In order to find the thermal decay timescales more accurately, data collected on longer timescales (up to 1 ns, but after oscillations have ceased) was fit to a single exponential decay, as shown in Figure 3(b). Thus, in total, the timescales for the evolution of TA signals were determined as follows: The signal decay on longer time delays attributable to thermal-energy transfer from nanoparticle to solvent was fit separately to a single exponential decay (Figure 3(b), dashed lines). Time constants extracted from these fits were found to be  $\tau_d = 173$  ps, 243 ps, 244 ps and 284 ps for the 54 nm, 85 nm, 121 nm and 144 nm particles respectively. Remaining fit parameters ( $\tau_r$ ,  $\tau_p$ ,  $p$ ,  $T_1$ , and signal amplitudes) were adjusted for best fit to

the signal oscillations seen in Figure 3(a). Notably, although  $T_2^*$  is listed as a variable parameter in Equation 1, for statistical particle size distributions it is related to the oscillation period as

$$T_2^* = \frac{\tau_p}{\pi\sqrt{2}} \left( \frac{d}{\sigma_d} \right) \quad 4.2$$

where  $d$  is the particle diameter and  $\sigma_d$  is its standard deviation. Thus,  $T_2^*$  was constrained by the size distribution determined with TEM for each particle sample ( $\sigma_d$  for each  $d$  listed in Table 1). Size histograms measured with TEM of Al NPs of four sizes are shown in Figure A2.1. Best-fit parameters obtained from this procedure are given in Table 1; errors determined for each fitting timescale are listed in Table A2.2. In the case of the 85-nm particles,  $T_1$  could not be determined accurately given the width of the particle size distribution (and therefore dominance of  $T_2^*$  in the overall damping dynamics), which is a consequence of the difficulty in controlling Al NP size dispersity through the use of carboxyl functional groups.<sup>45</sup> However, when  $T_1$  was fixed at 38.7 ps (a value determined by simulations described below) the value of  $d/\sigma_d$  determined by fitting  $T_2^*$  was within 10% of the value determined by TEM (4.4 vs. 3.95, respectively).

Based on our fits, we find that the phonon breathing period,  $T_1$  damping timescale, and thermal energy transfer timescales increase monotonically with increasing particle size. In contrast, the initial signal risetime is similar across particle samples. We note that we tried fitting the data without a rise component but found that the oscillatory component alone could not capture the shape of the signal induction correctly. This behavior is consistent with impulsive particle expansion as a combined result of electron-phonon and

initial phonon-phonon thermalization that sets the coherent phonon modes into motion.

Notably,  $\tau_d$ ,  $T_1$ , and  $\tau_p$  scale roughly linearly with nanoparticle diameter,  $d$ .

$d$ (nm)	$\sigma_d$ (nm)	$d/\sigma_d$	$T_1$ (ps)	$T_2^*$ (ps)	$\tau_p$ (ps)	$\tau_r$ (ps)	$\tau_d$ (ps)	$p$ (rad)
54	10.5	5.14	6.9	24.5	11.3	1.41	173	4.4
85	21.4	3.97	39	27.0	15.5	1.09	243	4.6
121	8.40	14.4	63	147	22.6	1.81	244	4.6
144	4.30	33.4	88	364	24.2	1.83	284	4.5

**Table 4.1:** Parameters determined from fitting the time-dependent evolution of transient absorption signals to Equation 1 and from TEM analysis ( $d$  and  $\sigma_d$ ) as a function of nanoparticle size. Fitting details are explained in the text. Standard errors associated with the fitting timescales are given in Table A2.2.

The periods and damping timescales of the phonon vibrations extracted from the transient absorption data are determined by the mechanical properties of the Al NPs and their interactions with the surrounding chemical environment. We performed finite-element method (FEM) calculations using frequency domain analysis to solve Navier's and the Navier-Stokes equations to model the vibrational period and damping associated with the oscillations in the experimental data. Our three-dimensional model consists of a single aluminum icosahedron with or without a 4 nm thick continuous  $\text{Al}_2\text{O}_3$  shell. The NP is surrounded by an IPA background in the simulations. For each particle size, we calculated the properties of the fundamental radial phonon mode which plays the dominant role in the TAS measurements. The inset of Figure 4(a) shows the displacement profile of the fundamental breathing mode of a core-shell Al/ $\text{Al}_2\text{O}_3$  icosahedron.

In order to investigate the size dependence of the Al NP phonon oscillations, we calculated the vibrational period and damping time for particles of four different sizes



corresponding to our measured samples. As shown in Figure 4(a), the oscillation periods of the core-shell particles are 7.6 ps, 12 ps, 17.1 ps and 20.6 ps for particles with diameters of 54 nm, 85 nm, 121 nm, and 144 nm, respectively. The oscillation periods of the fundamental breathing modes in the core-shell particles were slightly shorter than those calculated for pure Al NPs with the same diameters. The oscillation period has an approximately linear dependence on the diameter of the particle, consistent with Lamb's theory.<sup>46</sup> Our calculated results show similar trends compared with the values extracted from the transient spectral measurements with some deviations.

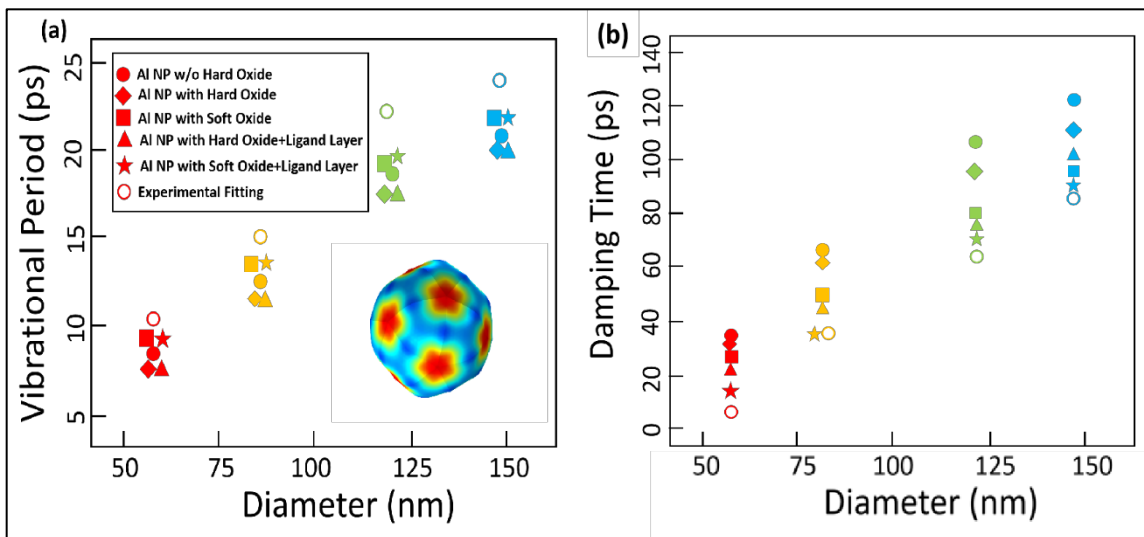
The damping timescale is defined as the time at which the displacement amplitude reaches  $1/e$  of its initial value and is equivalent to  $T_1$  in Equation 1. In Figure 4(b), we show the results of our FEM simulations for the phonon vibrational modes associated with particles of different sizes. Damping times of 34.5 ps, 62 ps, 95.4 ps and 116.2 ps were obtained for core-shell particles with diameters of 54 nm, 85 nm, 121 nm, and 144 nm, respectively. The trend of longer damping times with larger particle size was consistent for both Al-only and Al/Al<sub>2</sub>O<sub>3</sub> core/shell particles.

However, these calculated damping times from our simple particle model are in general much longer than the values we extracted from the TAS measurements. We attribute the discrepancy to the simplified model of the nanoparticle surface in the initial simulation model in which we assumed purely crystalline Al (in the case of the bare Al particles) and Al<sub>2</sub>O<sub>3</sub> (in the case of the core-shell particles) interacting with the surrounding fluid. We hypothesize that continuum damping processes associated with surfactant molecules bound to the particle surfaces, as well as the non-crystalline and non-stoichiometric nature of the native aluminum oxide layer, could play a non-trivial role in

the acoustic dynamics.

We sought to account for the hypothesized non-crystalline nature of the thin aluminum oxide shell<sup>47</sup> by reducing its assigned Young's modulus. As the Young's modulus of the oxide shell decreases, the damping time for particles of all sizes also decreases, while the oscillation period increases (Figure A2.4), leading to a closer match with experimental values. The results of the FEM model for an oxide shell Young's modulus of 50 GPa, consistent with literature reports on amorphous oxides,<sup>48</sup> are shown in Figure 4.

We next added an additional 1.3 nm capping layer on top of the oxide surface in the simulation model to account for the presence of the oleic acid capping ligands, using mechanical properties for the ligand shell from literature reports.<sup>40</sup> As can be seen in Figure 4(a) and (b), adding a thin organic shell to the particles results in no significant change in the oscillation periods. However, the damping times were considerably decreased, and the soft ligand shell played a more important role in the damping properties of the smaller particles. This resulted in calculated decay times of 21.3 ps, 46.6 ps, 79.6 ps, and 104.4 ps, compared to the experimental decay times of 6.9 ps, 39 ps, 63 ps, and 88 ps. The results from the FEM model that includes both a soft oxide shell and a ligand layer are also shown in Figure 4.



**Figure 4.4.** (a) Vibrational oscillation periods and (b) damping times calculated for icosahedral Al NPs of different sizes via finite element method simulations. The solid circles, rhombuses, squares, triangles and open circles represent pure Al particles, particles with a 4 nm thick crystalline oxide shell, particles with a soft (reduced Young’s modulus) oxide shell, particles with a 1.3 nm oleic acid shell layer, and experimental results from TA measurements, respectively. The stars represent the combined simulation results for particles with both a soft oxide shell and an oleic acid ligand layer. The inset of (a) is a calculation of the displacement of the fundamental radial mode for a 144 nm icosahedral Al NP with a 4 nm crystalline oxide shell

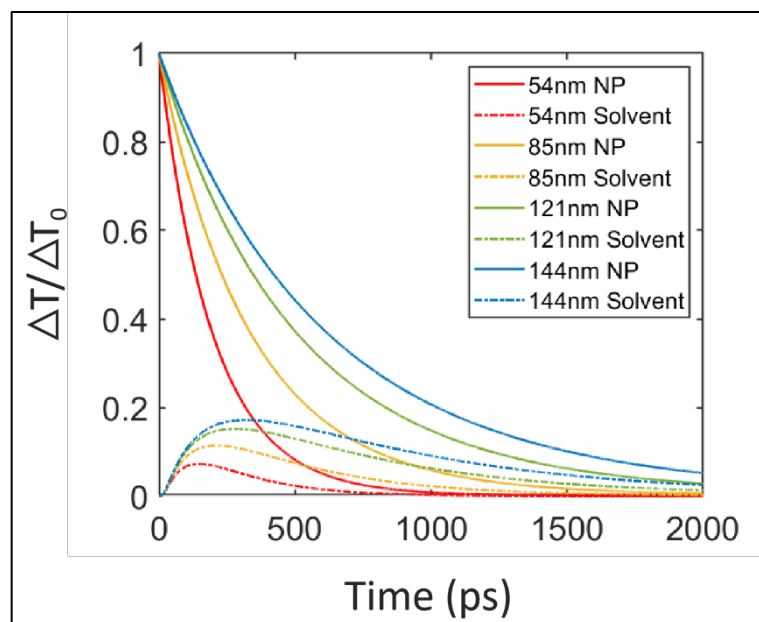
We compare the vibrational periods and damping times for the four sets of nanoparticles obtained via fitting of our transient absorption spectra ( $\tau_p$  and  $T_I$ ) and simulations of a single particle with soft oxide shell and ligand layer ( $\tau_{p.sim}$  and  $T_{I.sim}$ ) in Table 2. In quantitative comparison with experiments, adding a soft oxide shell layer had the largest impact on the vibrational period, and the calculated results match with the experimental values to within 9.1%-18.1%, depending on particle size. Adding a ligand shell to a crystalline oxide shell had a smaller effect on the vibrational period (14.5%-28.3% deviation from the experimental values) but produced damping times which are closer to the experimental values. In combination, the particle model that included both a soft oxide layer and an organic ligand shell most closely approached both the experimental

vibrational period (due primarily to the soft oxide) and damping timescale (due primarily to the ligand).

$d$ (nm)	$\tau_p$ (ps)	$\tau_{p.sim}$ (ps)	$T_l$ (ps)	$T_{l.sim}$ (ps)
54 nm	10.6	9.1	6.9	16.2
85 nm	15.1	13.5	39	38.7
121 nm	22.6	18.7	63	69.7
144 nm	24.2	22	88	90.5

**Table 4.2:** Vibrational periods and damping times for 54 nm, 85 nm, 121 nm, and 144 nm Al NPs from TA experiments ( $\tau_p$  and  $T_l$ ) and FEM simulations ( $\tau_{p.sim}$  and  $T_{l.sim}$ ) including both a soft oxide layer and ligand shell.

Finally, we used an extended two-interface model<sup>31</sup> to calculate the temperature evolution in both the particles and the solvent. As shown in Figure 5, we calculate solvent thermal heating times associated with the peak value of  $\Delta T/\Delta T_0$  in the solvent of 150 ps, 210 ps, 280 ps and 320 ps for particles with average diameters of 54 nm, 85 nm, 121 nm, and 144 nm, respectively. Fast heat transfer rates are observed for core-shell particles of all sizes compared to those predicted for aluminum-only particles which follow the same trend as in the TAS measurements. This further confirms that the oxide shell efficiently mediates heat transfer between the particle and the solvent independent of particle size.



**Figure 4.5.** Normalized calculated temperature evolutions relative to the initial temperature increase at both the outer edge of the aluminum cores and 3 nm into the surrounding solvent (IPA) of core-shell Al/Al<sub>2</sub>O<sub>3</sub> NPs with sizes ranging from 54 nm to 144 nm in diameter. An oxide shell layer of 4 nm in thickness is included in the simulation.

### 4.3 CONCLUSIONS

In conclusion, we studied the photothermal responses of solution-grown Al NPs as a function of nanoparticle size. In our TAS measurements, we observed fast heat transfer rates to the solvent for NPs of all sizes, mediated by the native oxide shell which is substantiated by results of a two-interface model for heat transfer. We also observed phonon vibrations in the optical spectra with decreasing periods and damping times as the size of the NPs decreases. FEM calculations verify the qualitative trends observed in experiment. We refined this model by considering surface effects on phonon damping and find that the non-crystalline nature of the native oxide shell and the presence of surface ligands leads to faster damping dynamics than predicted for pure aluminum nanoparticles interacting with a surrounding fluid only. Our study provides insight on the roles of surface

composition and particle size on both the photothermal and photoacoustic properties of Al-based plasmonic NPs. Specifically, by adding or subtracting “soft” surface components, such as oxide or polymer shells, phonon damping rates and thermal energy transfer times can be systematically increased or decreased. This effect could be useful for tuning nanoparticle properties “on demand” through prescriptive design for applications in photocatalysis, sensing, and medicine.

#### 4.4 METHODS

##### *Nanoparticle Synthesis.*

All solvents and reagents were purchased from Sigma-Aldrich. We used a nanoparticle synthesis method similar to Reference 31. Briefly, anhydrous tetrahydrofuran (THF) (6.3 ml), anhydrous 1,4-dioxane (6.3 ml) and 3.3 ml of dimethylethylaminealane were sequentially injected into a flask connected to an air-free Schlenk line. The solution was stirred and mildly heated to 40°C. Then 0.4 ml of 3.3 mM titanium (IV) isopropoxide in toluene was injected into the solution which became light brownish in color. 70 µl of oleic acid in dioxane was then injected at different times, ranging from three to thirty minutes, following titanium isopropoxide injection to obtain particles of tunable sizes. The reaction was completed after 1.5 hours and the solution became grey in color. The particles were washed twice using both THF and IPA and finally redispersed in IPA for measurements.

**Nanoparticle Surface Characterization.** Transmission Electron Microscopy (TEM) images were obtained with an FEI Tecnai T12 instrument with an accelerating voltage of 120 kV. High Resolution Transmission Electron Microscopy (HRTEM) measurements

were conducted with a Thermo Scientific TF30 TEM instrument working at 300 kV with better than 0.2 nm point-to-point resolution.

X-ray photoelectron spectroscopy (XPS) data were obtained using a PHI 5600 instrument equipped with a Mg K $\alpha$  flood source (1253.6 eV, 15 kV, 300 W) and a hemispherical energy analyzer. Scans were taken using a pass energy of 23.5 eV and 0.025 eV/step. Samples were attached to double-sided copper adhesive tape on an iron XPS sample stage. Spectra were energy adjusted to the C (1s) envelope at 285.0 eV and analyzed using CASA XPS software. Ion sputtering was performed using a PHI 04-303 differentially pumped ion gun operated at an emission current of 25 mA with argon pressure of 20 mPa. Samples were sputtered with 4 keV Ar<sup>+</sup> ions for 4 min. or 14 min. with a raster area of 7 x 7 mm<sup>2</sup>.

Fourier transform infrared (FTIR) spectra of oleate-capped nanoparticles and free oleic acid were measured using a Mattson Infinity Series FTIR with an EG&G Judson MCT detector. Nanoparticle samples were analyzed by drop-casting onto an NaCl salt plate and measuring a transmission spectrum. Free oleic acid samples were introduced by drop-casting onto an attachment for attenuated total reflectance (ATR). Nuclear magnetic resonance (<sup>1</sup>H NMR) spectra of oleate-capped nanoparticles and free oleic acid were collected with a Bruker Avance 300 MHz NMR Spectrometer. Oleic acid was dissolved and nanoparticle samples were resuspended in deuterated chloroform for these measurements.

Thermogravimetric analysis (TGA) was conducted with a TA Instruments SDT Q600 under flowing Ar at a heating rate of 5.0 °C min<sup>-1</sup>. An isothermal step was included at 82 °C for a duration of 30 min. to help drive off excess solvent. The temperature range

for ligand decomposition was found to be well below the onset of Al oxidation (600 °C).

### *UV-Vis Spectrophotometry Measurements*

Extinction spectra were obtained using an Agilent Cary 5000 UV-Vis-NIR spectrophotometer. Transmission through the solution of aluminum nanoparticles in IPA was measured in a 0.4 mL quartz cuvette over a wavelength range of 200 to 1000 nm.

### *Ultrafast spectroscopic measurements.*

The laser system used to conduct our experiments has been described previously.<sup>31,49</sup> Briefly, the 800-nm output from a Ti:Sapphire regenerative amplifier (Coherent Legend Elite, 1kHz, 4 mJ/pulse, 35-fs) was used to generate pump and probe pulses by non-linear optical processes. For the 3 smallest particle sizes the 400 nm pump pulses were produced by 2<sup>nd</sup> harmonic generation of 1 mJ of the fundamental in a BBO crystal. For the largest particles a 580 nm pump beam was generated from a femtosecond Optical Parametric Amplifier (Coherent OPerA Solo) was used to generate tunable pump pulses from 350 – 580 nm via various sequential nonlinear processes. The temporal resolution of these pulses has previously been measured between 50-70 fs. Broadband probe pulses were produced by driving white light supercontinuum generation with 100-200 nJ of 800 nm light in a 2-mm thick sapphire plate. We specifically utilized the near-infrared continuum (850-1150+ nm) to interrogate size-dependence of energy-transfer processes.

Output from the optical parametric amplifier (OPA) as well as the 400-nm pump beam were attenuated and gently focused to a 2.14-mm beam diameter at the sample using a 50-cm focal length lens positioned approximately 26 cm from the sample ensuring that the pump beam completely encompassed the entirety of the 100  $\mu$ m probe beam with a relative incident angle of  $\sim 10^\circ$ . Fluence dependent studies were conducted previously and



we found that the maximum energy density of these pump pulses under these focusing conditions was  $134 \mu\text{J cm}^{-2}$ , which was found to be well-below the threshold for nonlinear excitation of Al NP's.<sup>50-52</sup> All transient spectra were collected with linearly polarized pump and probe, with the relative polarization of the probe beam aligned at the “magic angle” ( $54.7^\circ$ ) to that of the pump beam by passing the white-light continuum through a wire-grid polarizer (Thorlabs) immediately before the sample.

The transmitted probe beam was aligned into a 0.3 m spectrograph (Acton-2360, Princeton Instruments) outfitted with a low-resolution grating (800 nm blaze, 150 lines/mm) with the center wavelength adjusted to 1000 nm to acquire spectra in the NIR region. A CCD camera (Pixis-100BR, Princeton Instruments) was configured to detect the NIR white-light continuum from the probe on each laser shot. Although the samples studied here did not fluoresce, they did scatter pump light considerably. In order to subtract the scattered light from the total acquisition corrections to the transmitted probe light was accomplished by alternately chopping the pump and probe to enable scatter-correction as summarized by Eqn 3.

$$\Delta I = \frac{I_{pump-probe} - I_{pump}}{I_{probe} - I_{background}} \quad 4.3$$

Transient spectra were then obtained by averaging scatter corrected signals over 20 000–25 000 laser shots at each pump–probe time delay.

### ***Finite Element Simulations.***

The phonon vibrational modes were calculated using Comsol Multiphysics software. The simulated structure consisted of a single Al/Al<sub>2</sub>O<sub>3</sub> icosahedral NP immersed in IPA. We performed frequency domain analysis for 3D simulations by solving Navier's and the Navier-Stokes equations. Continuity conditions for displacement, stress and velocity were applied at the particle's boundaries to fully couple the interaction between the particle and the liquid environment. Bulk elastic constants of Al and Al<sub>2</sub>O<sub>3</sub> were used as inputs for mechanical parameters. The soft shell of the oxide layer was modeled by reducing the oxide shell Young's modulus from 269 GPa to 50 GPa. We included the effect of oleic acid surface ligands by adding a thin shell layer on the particle surface with a Young's modulus, Poisson's ratio and density of 3 GPa, 0.36 and 900 kg/cm<sup>3</sup>, respectively.<sup>40</sup> The simulation results are independent of mesh size to within 0.1%.

## 4.5 REFERENCES

- (1) Atwater, H. A.; Polman, A. Plasmonics for Improved Photovoltaic Devices. *Nat. Mater.* **2010**, *9* (3), 205–213. <https://doi.org/10.1038/nmat2629>.
- (2) Sau, T. K.; Rogach, A. L.; Jäckel, F.; Klar, T. A.; Feldmann, J. Properties and Applications of Colloidal Nonspherical Noble Metal Nanoparticles. *Adv. Mater.* **2010**, *22* (16), 1805–1825. <https://doi.org/10.1002/adma.200902557>.
- (3) Talapin, D. V.; Lee, J.-S.; Kovalenko, M. V.; Shevchenko, E. V. Prospects of Colloidal Nanocrystals for Electronic and Optoelectronic Applications. *Chem. Rev.* **2010**, *110* (1), 389–458. <https://doi.org/10.1021/cr900137k>.
- (4) Luo, X.; Morrin, A.; Killard, A. J.; Smyth, M. R. Application of Nanoparticles in Electrochemical Sensors and Biosensors. *Electroanalysis* **2006**, *18* (4), 319–326. <https://doi.org/10.1002/elan.200503415>.
- (5) Guo, S.; Zhang, S.; Sun, S. Tuning Nanoparticle Catalysis for the Oxygen Reduction Reaction. *Angew. Chem. Int. Ed.* **2013**, *52* (33), 8526–8544. <https://doi.org/10.1002/anie.201207186>.
- (6) Murray, R. W. Nanoelectrochemistry: Metal Nanoparticles, Nanoelectrodes, and Nanopores. *Chem. Rev.* **2008**, *108* (7), 2688–2720. <https://doi.org/10.1021/cr068077e>.
- (7) Wang, P.; Huang, B.; Dai, Y.; Whangbo, M.-H. Plasmonic Photocatalysts: Harvesting Visible Light with Noble Metal Nanoparticles. *Phys. Chem. Chem. Phys.* **2012**, *14* (28), 9813–9825. <https://doi.org/10.1039/C2CP40823F>.
- (8) Ma, X.-C.; Dai, Y.; Yu, L.; Huang, B.-B. Energy Transfer in Plasmonic Photocatalytic Composites. *Light Sci. Appl.* **2016**, *5* (2), e16017. <https://doi.org/10.1038/lsa.2016.17>.
- (9) Atta, S.; Pennington, A. M.; Celik, F. E.; Fabris, L. TiO<sub>2</sub> on Gold Nanostars Enhances Photocatalytic Water Reduction in the Near-Infrared Regime. *Chem* **2018**, *4* (9), 2140–2153. <https://doi.org/10.1016/j.chempr.2018.06.004>.
- (10) Méndez-Medrano, M. G.; Kowalska, E.; Lehoux, A.; Herissan, A.; Ohtani, B.; Bahena, D.; Briois, V.; Colbeau-Justin, C.; Rodríguez-López, J. L.; Remita, H. Surface Modification of TiO<sub>2</sub> with Ag Nanoparticles and CuO Nanoclusters for Application in Photocatalysis. *J. Phys. Chem. C* **2016**, *120* (9), 5143–5154. <https://doi.org/10.1021/acs.jpcc.5b10703>.
- (11) Qin, Z.; Bischof, J. C. Thermophysical and Biological Responses of Gold Nanoparticle Laser Heating. *Chem. Soc. Rev.* **2012**, *41* (3), 1191–1217. <https://doi.org/10.1039/C1CS15184C>.
- (12) Huang, X.; Jain, P. K.; El-Sayed, I. H.; El-Sayed, M. A. Plasmonic Photothermal Therapy (PPTT) Using Gold Nanoparticles. *Lasers Med. Sci.* **2007**, *23* (3), 217. <https://doi.org/10.1007/s10103-007-0470-x>.
- (13) Jones, S.; Andrén, D.; Karpinski, P.; Käll, M. Photothermal Heating of Plasmonic Nanoantennas: Influence on Trapped Particle Dynamics and Colloid Distribution. *ACS Photonics* **2018**, *5* (7), 2878–2887. <https://doi.org/10.1021/acsp Photonics.8b00231>.
- (14) Kim, M.; Lee, J.-H.; Nam, J.-M. Plasmonic Photothermal Nanoparticles for Biomedical Applications. *Adv. Sci.* **0** (0), 1900471. <https://doi.org/10.1002/advs.201900471>.

- (15) Bagley, A. F.; Hill, S.; Rogers, G. S.; Bhatia, S. N. Plasmonic Photothermal Heating of Intraperitoneal Tumors through the Use of an Implanted Near-Infrared Source. *ACS Nano* **2013**, *7* (9), 8089–8097. <https://doi.org/10.1021/nn4033757>.
- (16) Braun, M.; Cichos, F. Optically Controlled Thermophoretic Trapping of Single Nano-Objects. *ACS Nano* **2013**, *7* (12), 11200–11208. <https://doi.org/10.1021/nn404980k>.
- (17) Chen, J.; Cong, H.; Loo, F.-C.; Kang, Z.; Tang, M.; Zhang, H.; Wu, S.-Y.; Kong, S.-K.; Ho, H.-P. Thermal Gradient Induced Tweezers for the Manipulation of Particles and Cells. *Sci. Rep.* **2016**, *6*, 35814. <https://doi.org/10.1038/srep35814>.
- (18) Fasciani, C.; Silvero, M. J.; Anghel, M. A.; Argüello, G. A.; Becerra, M. C.; Scaiano, J. C. Aspartame-Stabilized Gold–Silver Bimetallic Biocompatible Nanostructures with Plasmonic Photothermal Properties, Antibacterial Activity, and Long-Term Stability. *J. Am. Chem. Soc.* **2014**, *136* (50), 17394–17397. <https://doi.org/10.1021/ja510435u>.
- (19) Hu, M.; Chen, J.; Li, Z.-Y.; Au, L.; V. Hartland, G.; Li, X.; Marquez, M.; Xia, Y. Gold Nanostructures : Engineering Their Plasmonic Properties for Biomedical Applications. *Chem. Soc. Rev.* **2006**, *35* (11), 1084–1094. <https://doi.org/10.1039/B517615H>.
- (20) Menezes, J. W.; Ferreira, J.; Santos, M. J. L.; Cescato, L.; Brolo, A. G. Large-Area Fabrication of Periodic Arrays of Nanoholes in Metal Films and Their Application in Biosensing and Plasmonic-Enhanced Photovoltaics. *Adv. Funct. Mater.* **2010**, *20* (22), 3918–3924. <https://doi.org/10.1002/adfm.201001262>.
- (21) Tan, H.; Santbergen, R.; Smets, A. H. M.; Zeman, M. Plasmonic Light Trapping in Thin-Film Silicon Solar Cells with Improved Self-Assembled Silver Nanoparticles. *Nano Lett.* **2012**, *12* (8), 4070–4076. <https://doi.org/10.1021/nl301521z>.
- (22) Comin, A.; Manna, L. New Materials for Tunable Plasmonic Colloidal Nanocrystals. *Chem. Soc. Rev.* **2014**, *43* (11), 3957–3975. <https://doi.org/10.1039/C3CS60265F>.
- (23) Naik, G. V.; Shalaev, V. M.; Boltasseva, A. Alternative Plasmonic Materials: Beyond Gold and Silver. *Adv. Mater.* **2013**, *25* (24), 3264–3294. <https://doi.org/10.1002/adma.201205076>.
- (24) Ge, Z.-H.; Zhao, L.-D.; Wu, D.; Liu, X.; Zhang, B.-P.; Li, J.-F.; He, J. Low-Cost, Abundant Binary Sulfides as Promising Thermoelectric Materials. *Mater. Today* **2016**, *19* (4), 227–239. <https://doi.org/10.1016/j.mattod.2015.10.004>.
- (25) Knight, M. W.; King, N. S.; Liu, L.; Everitt, H. O.; Nordlander, P.; Halas, N. J. Aluminum for Plasmonics. *ACS Nano* **2014**, *8* (1), 834–840. <https://doi.org/10.1021/nn405495q>.
- (26) Olson, J.; Manjavacas, A.; Liu, L.; Chang, W.-S.; Foerster, B.; King, N. S.; Knight, M. W.; Nordlander, P.; Halas, N. J.; Link, S. Vivid, Full-Color Aluminum Plasmonic Pixels. *Proc. Natl. Acad. Sci.* **2014**, *111* (40), 14348–14353. <https://doi.org/10.1073/pnas.1415970111>.
- (27) Hao, Q.; Wang, C.; Huang, H.; Li, W.; Du, D.; Han, D.; Qiu, T.; Chu, P. K. Aluminum Plasmonic Photocatalysis. *Sci. Rep.* **2015**, *5*, 15288. <https://doi.org/10.1038/srep15288>.
- (28) Tseng, M. L.; Yang, J.; Semmlinger, M.; Zhang, C.; Nordlander, P.; Halas, N. J. Two-Dimensional Active Tuning of an Aluminum Plasmonic Array for Full-Spectrum

- Response. *Nano Lett.* **2017**, *17* (10), 6034–6039.  
<https://doi.org/10.1021/acs.nanolett.7b02350>.
- (29) Su, M.-N.; Dongare, P. D.; Chakraborty, D.; Zhang, Y.; Yi, C.; Wen, F.; Chang, W.-S.; Nordlander, P.; Sader, J. E.; Halas, N. J.; et al. Optomechanics of Single Aluminum Nanodisks. *Nano Lett.* **2017**, *17* (4), 2575–2583.  
<https://doi.org/10.1021/acs.nanolett.7b00333>.
- (30) Su, M.-N.; Ciccarino, C. J.; Kumar, S.; Dongare, P. D.; Hosseini Jebeli, S. A.; Renard, D.; Zhang, Y.; Ostovar, B.; Chang, W.-S.; Nordlander, P.; et al. Ultrafast Electron Dynamics in Single Aluminum Nanostructures. *Nano Lett.* **2019**, *19* (5), 3091–3097. <https://doi.org/10.1021/acs.nanolett.9b00503>.
- (31) Smith, K. J.; Cheng, Y.; Arinze, E. S.; Kim, N. E.; Bragg, A. E.; Thon, S. M. Dynamics of Energy Transfer in Large Plasmonic Aluminum Nanoparticles. *ACS Photonics* **2018**, *5* (3), 805–813. <https://doi.org/10.1021/acsp Photonics.7b00932>.
- (32) Crut, A.; Maioli, P.; Del Fatti, N.; Vallée, F. Acoustic Vibrations of Metal Nano-Objects: Time-Domain Investigations. *Phys. Rep.* **2015**, *549*, 1–43.  
<https://doi.org/10.1016/j.physrep.2014.09.004>.
- (33) Mahmoud, M. A.; O’Neil, D.; El-Sayed, M. A. Shape- and Symmetry-Dependent Mechanical Properties of Metallic Gold and Silver on the Nanoscale. *Nano Lett.* **2014**, *14* (2), 743–748. <https://doi.org/10.1021/nl4040362>.
- (34) Portales, H.; Saviot, L.; Duval, E.; Fujii, M.; Hayashi, S.; Del Fatti, N.; Vallée, F. Resonant Raman Scattering by Breathing Modes of Metal Nanoparticles. *J. Chem. Phys.* **2001**, *115* (8), 3444–3447. <https://doi.org/10.1063/1.1396817>.
- (35) Major, T. A.; Crut, A.; Gao, B.; Lo, S. S.; Fatti, N. D.; Vallée, F.; Hartland, G. V. Damping of the Acoustic Vibrations of a Suspended Gold Nanowire in Air and Water Environments. *Phys. Chem. Chem. Phys.* **2013**, *15* (12), 4169–4176.  
<https://doi.org/10.1039/C2CP43330C>.
- (36) Stoll, T.; Maioli, P.; Crut, A.; Burgin, J.; Langot, P.; Pellarin, M.; Sánchez-Iglesias, A.; Rodríguez-González, B.; Liz-Marzán, L. M.; Del Fatti, N.; et al. Ultrafast Acoustic Vibrations of Bimetallic Nanoparticles. *J. Phys. Chem. C* **2015**, *119* (3), 1591–1599. <https://doi.org/10.1021/jp511070h>.
- (37) Kirakosyan, A. S.; Shahbazyan, T. V. Vibrational Modes of Metal Nanoshells and Bimetallic Core-Shell Nanoparticles. *J. Chem. Phys.* **2008**, *129* (3).  
<https://doi.org/10.1063/1.2953450>.
- (38) Hodak, J. H.; Henglein, A.; Hartland, G. V. Photophysics of Nanometer Sized Metal Particles: Electron–Phonon Coupling and Coherent Excitation of Breathing Vibrational Modes. *J. Phys. Chem. B* **2000**, *104* (43), 9954–9965.  
<https://doi.org/10.1021/jp002256x>.
- (39) Mongin, D.; Juvé, V.; Maioli, P.; Crut, A.; Del Fatti, N.; Vallée, F.; Sánchez-Iglesias, A.; Pastoriza-Santos, I.; Liz-Marzán, L. M. Acoustic Vibrations of Metal-Dielectric Core–Shell Nanoparticles. *Nano Lett.* **2011**, *11* (7), 3016–3021.  
<https://doi.org/10.1021/nl201672k>.
- (40) Lee, E. M. Y.; Mork, A. J.; Willard, A. P.; Tisdale, W. A. Including Surface Ligand Effects in Continuum Elastic Models of Nanocrystal Vibrations. *J. Chem. Phys.* **2017**, *147* (4), 044711. <https://doi.org/10.1063/1.4995439>.
- (41) Pelton, M.; Sader, J. E.; Burgin, J.; Liu, M.; Guyot-Sionnest, P.; Gosztola, D. Damping of Acoustic Vibrations in Gold Nanoparticles. *Nat. Nanotechnol.* **2009**, *4* (8),


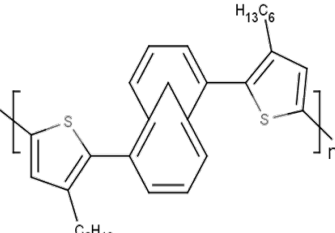
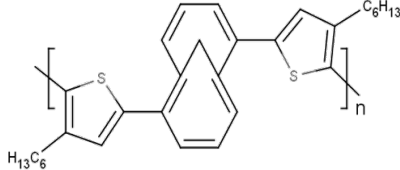
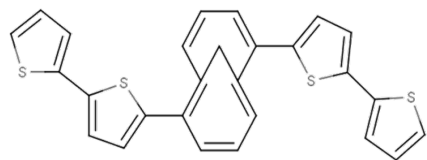
- 492–495. <https://doi.org/10.1038/nnano.2009.192>.
- (42) Burg, T. P.; Godin, M.; Knudsen, S. M.; Shen, W.; Carlson, G.; Foster, J. S.; Babcock, K.; Manalis, S. R. Weighing of Biomolecules, Single Cells and Single Nanoparticles in Fluid. *Nature* **2007**, *446* (7139), 1066–1069. <https://doi.org/10.1038/nature05741>.
- (43) Jensen, K.; Kim, K.; Zettl, A. An Atomic-Resolution Nanomechanical Mass Sensor. *Nat. Nanotechnol.* **2008**, *3* (9), 533–537. <https://doi.org/10.1038/nnano.2008.200>.
- (44) McClain, M. J.; Schlather, A. E.; Ringe, E.; King, N. S.; Liu, L.; Manjavacas, A.; Knight, M. W.; Kumar, I.; Whitmire, K. H.; Everitt, H. O.; et al. Aluminum Nanocrystals. *Nano Lett.* **2015**, *15* (4), 2751–2755. <https://doi.org/10.1021/acs.nanolett.5b00614>.
- (45) Lu, S.; Yu, H.; Gottheim, S.; Gao, H.; DeSantis, C. J.; Clark, B. D.; Yang, J.; Jacobson, C. R.; Lu, Z.; Nordlander, P.; et al. Polymer-Directed Growth of Plasmonic Aluminum Nanocrystals. *J. Am. Chem. Soc.* **2018**, *140* (45), 15412–15418. <https://doi.org/10.1021/jacs.8b08937>.
- (46) Lamb, H. On the Vibrations of an Elastic Sphere. *Proc. Lond. Math. Soc.* **1881**, *s1-13* (1), 189–212. <https://doi.org/10.1112/plms/s1-13.1.189>.
- (47) Firmansyah, D. A.; Sullivan, K.; Lee, K.-S.; Kim, Y. H.; Zahaf, R.; Zachariah, M. R.; Lee, D. Microstructural Behavior of the Alumina Shell and Aluminum Core Before and After Melting of Aluminum Nanoparticles. *J. Phys. Chem. C* **2012**, *116* (1), 404–411. <https://doi.org/10.1021/jp2095483>.
- (48) Esmaily, A. S.; Mills, S.; Coey, J. M. D. Exceptional Room-Temperature Plasticity in Amorphous Alumina Nanotubes Fabricated by Magnetic Hard Anodisation. *Nanoscale* **2017**, *9* (16), 5205–5211. <https://doi.org/10.1039/C7NR00095B>.
- (49) Molloy, M. S.; Snyder, J. A.; Bragg, A. E. Structural and Solvent Control of Nonadiabatic Photochemical Bond Formation: Photocyclization of o-Terphenyl in Solution. *J. Phys. Chem. A* **2014**, *118* (22), 3913–3925. <https://doi.org/10.1021/jp501988g>.
- (50) Katayama, T.; Setoura, K.; Werner, D.; Miyasaka, H.; Hashimoto, S. Picosecond-to-Nanosecond Dynamics of Plasmonic Nanobubbles from Pump–Probe Spectral Measurements of Aqueous Colloidal Gold Nanoparticles. *Langmuir* **2014**, *30* (31), 9504–9513. <https://doi.org/10.1021/la500663x>.
- (51) Ziegler, T.; Hendrich, C.; Hubenthal, F.; Vartanyan, T.; Träger, F. Dephasing Times of Surface Plasmon Excitation in Au Nanoparticles Determined by Persistent Spectral Hole Burning. *Chem. Phys. Lett.* **2004**, *386* (4), 319–324. <https://doi.org/10.1016/j.cplett.2004.01.001>.
- (52) Zhao, T.; Jiang, X.-F.; Gao, N.; Li, S.; Zhou, N.; Ma, R.; Xu, Q.-H. Solvent-Dependent Two-Photon Photoluminescence and Excitation Dynamics of Gold Nanorods. *J. Phys. Chem. B* **2013**, *117* (49), 15576–15583. <https://doi.org/10.1021/jp405929w>.

# Chapter 5

## Exciton Diffusion in Poly(thiophene- methanoannulene) Characterized by Singlet- Singlet Annihilation

### 5.0 INTRODUCTION

Another component of this thesis focuses on the photophysics of a novel polymer, poly(thiophene- 1,6-methano (10)annulene- thiophene) (PTMT). This polymer was originally studied<sup>1</sup> in our lab as part of a broader study interrogating photophysical properties of a set of four TMT polymers and oligomers with very similar structures shown in Figure 5.1 differentiated by the position of solubilizing alkyl groups (the so-called “tail”); these include no-tail PTMT (NT-PTMT), tail-in PTMT (TI-PTMT), tail-out PTMT (TO-PTMT) and the oligomer TTMTT. These polymers exhibit amorphous thin-film morphology but maintain reasonably high hole mobility  $\sim 10^{-4} \text{ cm}^2 \text{ V}^{-1} \text{ s}^{-1}$  when used as semiconducting layers in organic field-effect transistor (OFET) devices. This implies they may be of interest in the development of organic optoelectronics.<sup>2</sup> The material herein will focus specifically on the TI-PTMT polymer because it was previously found to exhibit ultrafast depolarization of absorption transitions from the lowest excited singlet state after photoexcitation, implying the existence of fast energy transfer mechanisms.

a) NT-PTMT	
b) TI-PTMT	
c) TO-PTMT	
d) TMTT Oligomer	

**Table 5.1:** Thiophene-methanoannulene structures; this chapter focuses on exciton diffusion in TI-PTMT.

Singlet excitons in organic materials are coulombically bound electron-hole pairs which cannot inherently generate photocurrent. However, electron donor/acceptor heterojunctions are used to generate charge carriers where excitons are dissociated if the energy difference between the lowest occupied molecular orbital (LUMO) of the donor and highest occupied molecular orbital (HOMO) of the acceptor is enough to overcome the coulombic attraction.<sup>3</sup> In order for these charge carriers to be harvested for photocurrent generation excitons need to diffuse to the interface between donor and acceptor materials before they relax back to the ground state. As such exciton diffusion length in organic



photoactive polymers is of great importance and the focus of a great deal of research in organic photovoltaic materials. The diffusion length is given by Equation 5.1 below where  $D$  is the diffusion coefficient and  $\tau$  is the exciton lifetime.

$$L_D = \sqrt{D\tau} \quad 5.1$$

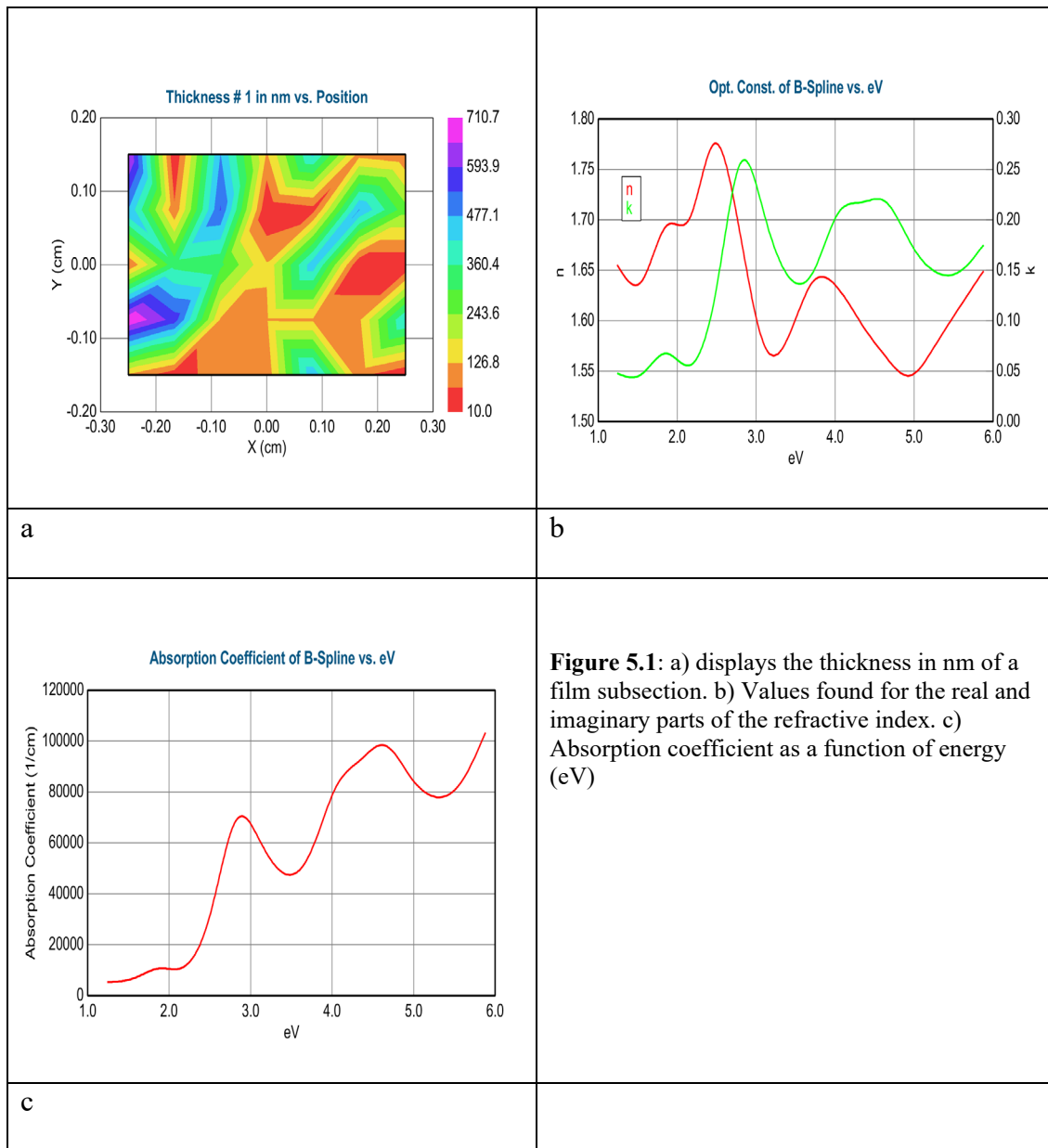
Interchain interactions can have profound effects on the optoelectronic properties of conjugated polymers, and notably the diffusion of excitons and charges. P3HT is perhaps the best characterized polymer photophysically. P3HT exhibits two microstructures within its films: 1) ordered semi-crystalline regions which are lamellar-stacked or H-aggregated strands and 2) amorphous regions lacking interchain order. The crystalline regions create networks that may facilitate energy migration and charge transport that are beneficial for photovoltaic applications but at the same time strong interchain interactions lead to the increased probability of exciton annihilation or other quenching processes. Amorphous domains in the film result in decreased effective conjugation limiting the conductive properties and decreasing diffusion length making the conversion to photocurrent less efficient. An interesting strategy to increase charge mobility is to use a combination of planar and non-planar conjugated building blocks to create an intrinsically non-planar conjugated polymer backbone that at the same time results in a relatively amorphous film morphology. The resultant microstructure is expected to inhibit extensive interchain interactions without compromising electron delocalization along polymer strands. PTMT structures possess such structural characteristics, and the goal of the work described here is to determine if these unique structures can facilitate rapid

energy diffusion through an amorphous material structure.

A common spectroscopic technique to observe diffusion dynamics in conjugated polymers is to characterize self-quenching via singlet-singlet annihilation (SSA)<sup>4</sup> which is well known to occur in polymers such as poly(3-hexylthiophene-2,5-diyl) or P3HT.<sup>3,5</sup> SSA is a biexciton interaction, whereby two singlet excitons “combine” to make a single highly excited state  $S_N$  through the net reaction  $S_1 + S_1 \rightarrow S_N + S_0$ ; the highly excited state  $S_N$  subsequently deactivates nonradiatively to  $S_1$ , resulting in an effective quenching efficiency per encounter of 50%. As two singlets can be expected to encounter each other diffusively, it is possible to use SSA to determine the exciton diffusion rate. Relatively high excitation fluences are typically used in experiments to increase exciton densities to induce SSA; at these densities’ exciton decay becomes much more rapid at shorter times but at longer times the intrinsic lifetime of the exciton remains unaffected. The faster decay at short times has been found to be intensity dependent that is attributed to an increased rate of annihilation. We initially conducted intensity dependent experiments with aggregated PTMT nanoparticles that exhibit similar behaviors as polymer films but which can be studied in solution; however, unlike films, it was not possible to determine the precise exciton densities of dispersed NP’s in solution so a thin film of PTMT was created for more accurate determinations. The details of calculating the diffusion length and SSA rate from these experiments will be discussed in this chapter.

## 5.1 EXPERIMENTAL METHODS

### 5.1.1 Determination of Basic Parameters



A thin film was created by drop-casting a solution of TI-PTMT onto a window and the

absorption coefficient, refractive index and film thickness were found using ellipsometry in a Woollam M-2000 ellipsometer. Figure 5.2a and 5.2b show the film thickness vs position and the optical constants  $n$  (refractive index) and  $k$  (extinction coefficient) with respect to energy.

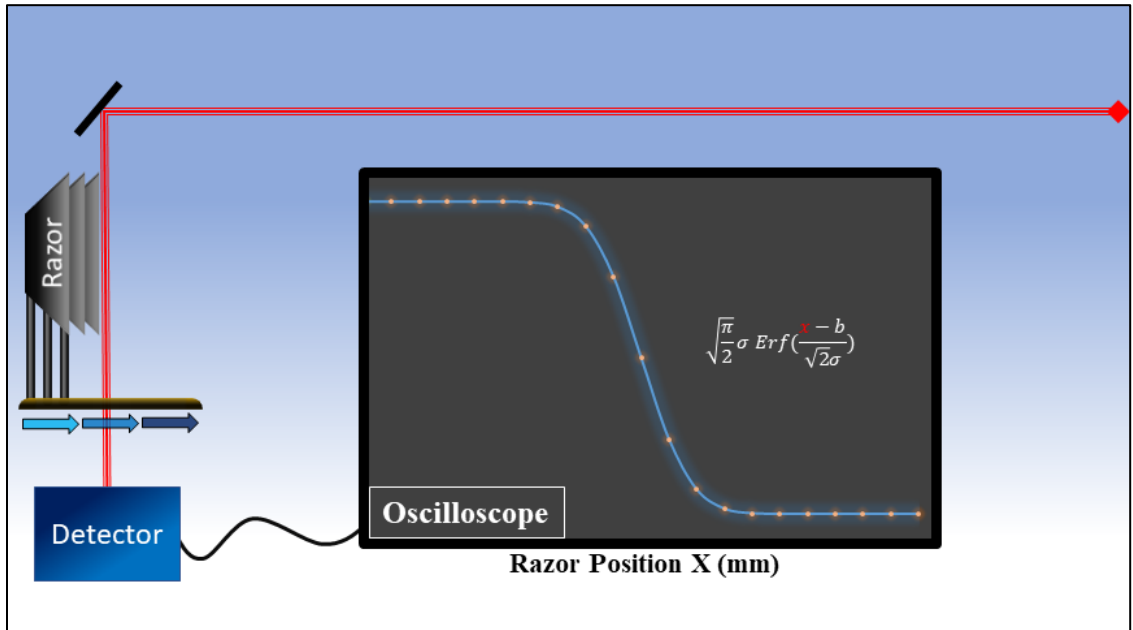
The optical density was found by measuring the steady-state absorption spectrum of the film in a Perkin Elmer, Lambda 2 UV/Vis spectrometer (5.2c). It was not possible to utilize a technique that would produce a more uniform layer, such as spin coating, due to the polymer's sparing solubility in solvents known to produce high quality films.

Ultrafast broadband pump-probe experiments were conducted with polymer excitation at 400 and 500 nm. At high excitation fluences the sample was found to degrade over a 5-15 min period if the focusing conditions of the beam were too intense. Thus, great care had to be taken to ensure the lowest energy densities possible to maintain polymer integrity; unfortunately, this also restricted the range of possible excitation fluences due to low signal amplitudes  $\Delta OD < 0.005$ .

### ***5.1.2 Laser Fluence Determinations.***

In order to calculate accurate laser fluences, precise measurements of the beam diameter and pulse energy were required. Measurement of the first was accomplished using a razor blade mounted vertically on a spring-loaded stage controlled by a Thor-Labs TDC001 T-Cube DC Servo Controller. The blade was slowly swept perpendicular to the beam path, resulting in spatial attenuation of the beam; the beam attenuation was measured with a photo-diode detector connected to an oscilloscope (Figure 5.2). The position of the razor with respect to beam intensity was then plotted and fit to an error function (erf); the

derivative of the fitted error function gives the gaussian profile of the laser pulse to a good approximation. This was repeated for both the pump beam as well as the white light probe beam.



**Figure 5.2:** Schematic diagram of method used to find the beam width for calculation of the laser fluence.

The integral of a two-dimensional gaussian gives Equation 5.2.

$$P = 2A\pi\sigma^2 \quad 5.2$$

Where  $\sigma$  is a measure of the beam waist in centimeters and calculated from the integration of the error function,  $P$  is the power in J/s and by using dimensional analysis it is straight forward to see that  $A$  must have units of J/cm<sup>2</sup> and corresponds with the laser fluence. The power  $P$  was measured with a power meter immediately before the sample. In order to prevent sample degradation, the pump beams were left unfocused with  $\sigma_{pu} \sim 0.31 / r \sim 1.75$

mm while the probe beam was found to have  $\sigma_{pr} \sim 48 \text{ } \mu\text{m} / r \sim 127 \text{ } \mu\text{m}$ . The pump beam energy density was found to be  $261.6 \text{ } \mu\text{J}/\text{cm}^2$  for the 400 nm experiment 496.8 or  $248.4 \text{ } \mu\text{J}/\text{cm}^2$  for the 500 nm experiments. The lower value was obtained after placing a neutral density filter OD = 0.3 (~50%) in the path of the pump.

## 5.2 MODELING PROCEDURES

### 5.2.1 Singlet-singlet annihilation model

The rate Equation for singlet exciton decay used in these experiments was taken from previously published work by Tamai et. al.<sup>3</sup> and is given by Equation 5.3.

$$\frac{dN(t)}{dt} = -\frac{N(t)}{\tau} - \frac{1}{2}\gamma(t)N(t)^2 \quad 5.3$$

Here  $N(t)$  is the exciton density at some delay time  $t$  after the pump pulse reaches the sample,  $\gamma(t)$  is the bimolecular decay rate coefficient for SSA and  $\tau$  is the intrinsic exciton decay lifetime. The integrated rate law is solved as

$$N(t) = \frac{N_0 \exp(-t/\tau)}{1 + \frac{1}{2}N_0 \int_0^t \gamma(t') \exp(-t'/\tau) dt'} \quad 5.4$$

$N_0$  is the initial exciton density after optical pumping while the annihilation rate coefficient  $\gamma(t)$  can be given in three dimensions and is given by Equation 5.5. The form of  $\gamma(t)$  depends on the dimensionality of the system, however the 1D and 2D cases were not examined here.

$$\gamma(t)_{3D} = 8\pi DR \left( 1 + \frac{R}{\sqrt{2\pi Dt}} \right) \quad 5.5$$

D is the diffusion coefficient with units of cm<sup>2</sup>/s and R is the interaction radius in units of cm; the latter represents the separation at which SSA occurs. This function  $\gamma(t)$  can be used to solve Equation 5.3, resulting in Equations 5.6 and 5.7. The parameter  $a$  is a scaling factor necessary to scale fits to data measured in  $\Delta OD$  which is proportional to  $N(t)$ .

$$N(t) = \frac{a \exp(-t/\tau)}{1 + N_0 F(t)} \quad 5.6$$

$$F(t) = 4\pi DR\tau[1 - \exp(-t/\tau)] + 4\pi R^2 \sqrt{D\tau/2} \operatorname{erf}(\sqrt{t/\tau}) \quad 5.7$$

Details about this procedure can be found at great length in the literature.<sup>3,6,7</sup> Experimental data were modeled using Equations 5.6 and 5.7.

### 5.2.2 Estimation of Initial Exciton Density ( $N_0$ )

In order to estimate  $N_0$  one must consider the overlap of the pump and probe beams. By manually steering the pump beam overlap to the area with highest  $\Delta OD$  we can assume that the probe beam is at or very near the maximum of the pump beam envelope. Using the fluence “A” calculated earlier, R the probe spot radius and Equation 5.7 the average exciton density  $N_{\text{photon}}$  is found.

$$N_{\text{photon}} = \frac{1}{\pi R^2} \int_0^R \int_0^{2\pi} A r \exp(-r^2/2\sigma^2) dr d\theta = \frac{2A\sigma^2}{R^2} [1 - \exp(-R^2/2\sigma^2)] \quad 5.7$$

Using the Beer-Lambert Law the initial exciton density can be calculated

$$N_0 = \frac{N_{\text{photon}}(1 - 10^{-OD})}{l} \quad 5.8$$

Where  $l$  is the thickness of the film found from the ellipsometry data. Values found for  $N_0$ ,  $N_{\text{photon}}$ , and  $l$  are listed in Table 5.1 Below.

	$N_0$ (cm <sup>-3</sup> )	$N_{\text{photon}}$ (cm <sup>-2</sup> )	$l$ (nm)
$\lambda_p = 400$ nm	$1.19 \times 10^{19}$	$5.23 \times 10^{14}$	413
$\lambda_p = 500$ nm	$1.98 \times 10^{19}$	$1.20 \times 10^{15}$	413
$\lambda_p = 500$ nm (50%)	$9.91 \times 10^{18}$	$5.98 \times 10^{14}$	413

**Table 5.2:** Calculated values of Initial exciton density ( $N_0$ ), photon density ( $N_{\text{photon}}$ ), and effective path length ( $l$ ).

### 5.2.3 Transient Absorption Experiment

Three data sets were examined with pump wavelengths at 400 nm and 500 nm, with a third experiment utilizing the 500 nm pump but including a neutral density filter of OD = 0.3 placed in the pump beam to decrease its intensity by 50%. Transient absorption was conducted on all of these samples using a detection range in the NIR (800 – 1100 nm). This detection range was selected to avoid any contamination by the TA features that appear in the visible absorption spectrum. Kinetic traces were calculated by averaging across a range of wavelengths (900 – 1000 nm) at each time delay. These polymers are well known to possess a triplet absorption that can be observed across the visible and NIR ranges however the triplet persists long after the initial relaxation, on the order of a nanosecond. In order to account for this signal, the intensity at the 5 latest time delays after 1000 ps were averaged and subtracted from the kinetic traces. The remaining time-



dependent signal therefore only reflects the population of singlet excitons that decays by SSA or on the natural exciton decay lifetime.

### 5.3 RESULTS AND DISCUSSION

Since PTMT has not been studied previously the interaction radius of this polymer is not known, however it's properties should be comparable to that of P3HT. For the purposes of fitting the experimental data a series of 3 interaction radii (1-3 nm) which correspond to

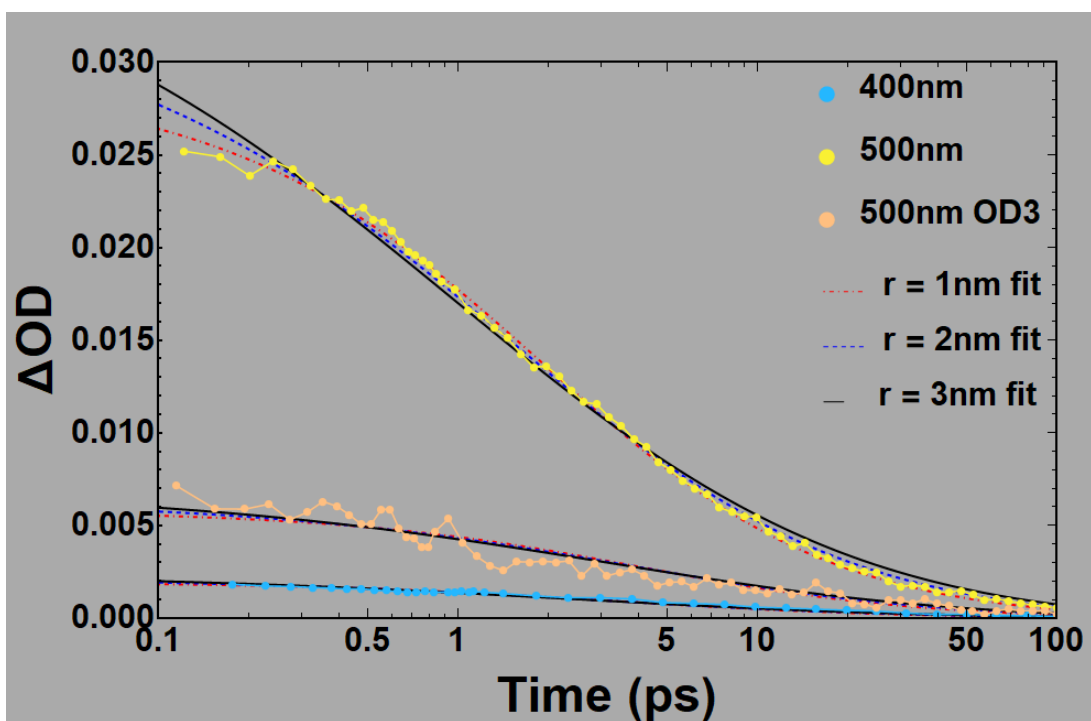


Figure 5.3: Kinetic traces of exciton decay in PTMT

the range of radii found for P3HT<sup>5</sup> were chosen and used as parameters for fitting the experimental data. The intrinsic exciton lifetime of PTMT was found<sup>1</sup> previously to be  $\tau = 153$  ps and this value was also constrained when fitting experimental data in this study.

Examination of the fits shows that for the sample pumped at 400 nm and 500 nm with the intensity modulated by a ND filter OD = 0.3 (50% reduction intensity) all of the fits are in reasonable agreement. For the 500 nm pump data with high intensity, as the interaction radius is increased from 1 to 3 the fits become noticeably worse. This is likely a reflection on the fact that a large R results in a smaller value of D to account for the initial population decay by SSA; the smaller value of D at longer times results in poorer agreement with slower phases of diffusive SSA.

r (nm)	D (cm <sup>2</sup> s <sup>-1</sup> ) x10 <sup>-3</sup>	L <sub>D</sub> (nm)	τ (ps)
1	5.05	8.7	153
2	1.7	5.17	153
3	0.8	3.34	153

**Table 5.3:** Calculated diffusion constant and length for TI-PTMT from varying interaction radius and fixed exciton lifetime

Sample	D (cm <sup>2</sup> s <sup>-1</sup> ) x10 <sup>-3</sup>	L <sub>D</sub> (nm)	Dimension
RR-P3HT-H	7.9	20	1D
RR-P3HT-L	3.3	14	1D
RRa-P3HT	0.46	4.8	3D

**Table 5.4:** Values taken from the literature of the diffusion constant and diffusion length for the polymer P3HT<sup>3</sup>

Table 5.3 presents the values for the diffusion constant found at the three different interaction radii. The values can be compared to those found in the literature<sup>3</sup> for P3HT that are shown in Table 5.4. Across all interaction radii the diffusion coefficient for TI-

PTMT is larger than that of the amorphous polymer regioregular (RR-P3HT) and regiorandom P3HT (RRa-P3HT); indeed, even at the longest interaction radius of 3 nm PTMT has a value of  $0.8 \times 10^{-3} \text{ cm}^2 \text{ s}^{-1}$  which is very close to RRa-P3HT ( $0.46 \times 10^{-3} \text{ cm}^2 \text{ s}^{-1}$ ). At the shortest interaction radius of 1 nm the diffusion coefficient has a value of  $5.05 \times 10^{-3} \text{ cm}^2 \text{ s}^{-1}$  which is comparable to that of highly crystalline regioregular P3HT ( $7.9 \times 10^{-3} \text{ cm}^2 \text{ s}^{-1}$ ).

#### **5.4 CONCLUSION**

This study demonstrated that the conjugated amorphous polymer TI-PTMT may possess beneficial energy transfer characteristics, despite exhibiting an amorphous morphology. Despite lacking a crystalline nature, the diffusion coefficient was found to be greater than that of RRa-P3HT across a range of likely interaction radii and approaching that of crystalline RR-P3HT. Notably, the relatively large diffusion coefficient of TI - PTMT is modulated by the relatively short exciton lifetime, resulting in a net shorter diffusion length compared to crystalline RR-P3HT, but still somewhat longer than that observed for RRa-P3HT. This limitation could be overcome by striking a balance between nonplanar structures that support amorphous morphologies with intrinsically continuous conjugation pathways per strand and the impact of nonplanarity on spin-orbit coupling and therefore intersystem crossing that reduces the exciton lifetime. Further study of this class of polymer may reveal its potential use in photoactive devices without the interference of multiple structure domains that plague P3HT.

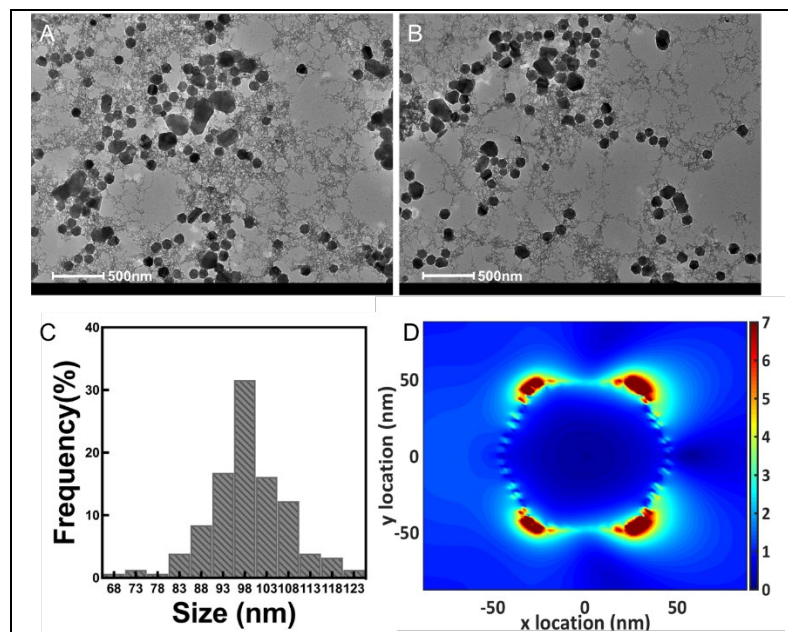
## 5.5 REFERENCES

- (1) Magnanelli, T. J. *Spectroscopic Probes of Charge Separation, Energy Transfer and their Dependencies on Local Structure in Assembled Organic Materials*. PhD Thesis, Johns Hopkins University, Baltimore, MD. 2017
- (2) Streifel, B. C.; Peart, P. A.; Martínez Hardigree, J. F.; Katz, H. E.; Tovar, J. D. Torsional Influences within Disordered Organic Electronic Materials Based upon Non-Benzenoid 1,6-Methano[10]Annulene Rings. *Macromolecules* **2012**, *45* (18), 7339–7349. <https://doi.org/10.1021/ma301408w>.
- (3) Tamai, Y.; Ohkita, H.; Bente, H.; Ito, S. Exciton Diffusion in Conjugated Polymers: From Fundamental Understanding to Improvement in Photovoltaic Conversion Efficiency. *J. Phys. Chem. Lett.* **2015**, *6* (17), 3417–3428. <https://doi.org/10.1021/acs.jpcllett.5b01147>.
- (4) Mosses, J.; Syme, C. D.; Wynne, K. Order Parameter of the Liquid–Liquid Transition in a Molecular Liquid. *J. Phys. Chem. Lett.* **2015**, *6* (1), 38–43. <https://doi.org/10.1021/jz5022763>.
- (5) Tamai, Y.; Matsuura, Y.; Ohkita, H.; Bente, H.; Ito, S. One-Dimensional Singlet Exciton Diffusion in Poly(3-Hexylthiophene) Crystalline Domains. *J. Phys. Chem. Lett.* **2014**, *5* (2), 399–403. <https://doi.org/10.1021/jz402299a>.
- (6) King, S. M.; Dai, D.; Rothe, C.; Monkman, A. P. Exciton Annihilation in a Polyfluorene: Low Threshold for Singlet-Singlet Annihilation and the Absence of Singlet-Triplet Annihilation. *Phys. Rev. B* **2007**, *76* (8), 085204. <https://doi.org/10.1103/PhysRevB.76.085204>.
- (7) Dogariu, A.; Vacar, D.; Heeger, A. J. Picosecond Time-Resolved Spectroscopy of the Excited State in a Soluble Derivative of Poly(Phenylene Vinylene): Origin of the Bimolecular Decay. *Phys. Rev. B* **1998**, *58* (16), 10218–10224. <https://doi.org/10.1103/PhysRevB.58.10218>.

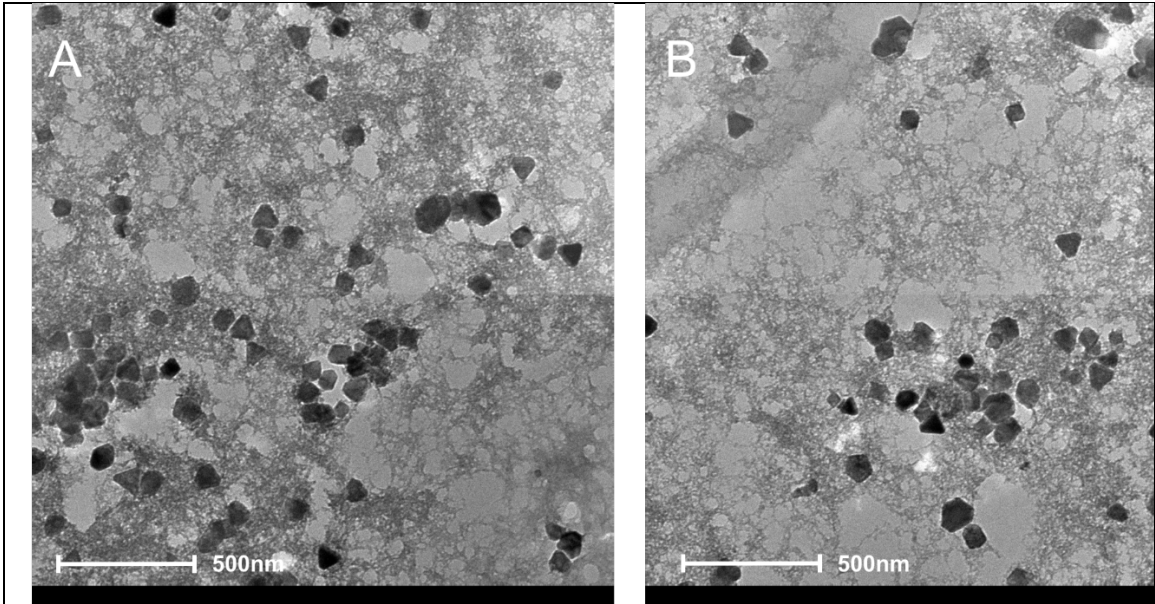
# Appendix I

## Supporting Information Chapter 3:

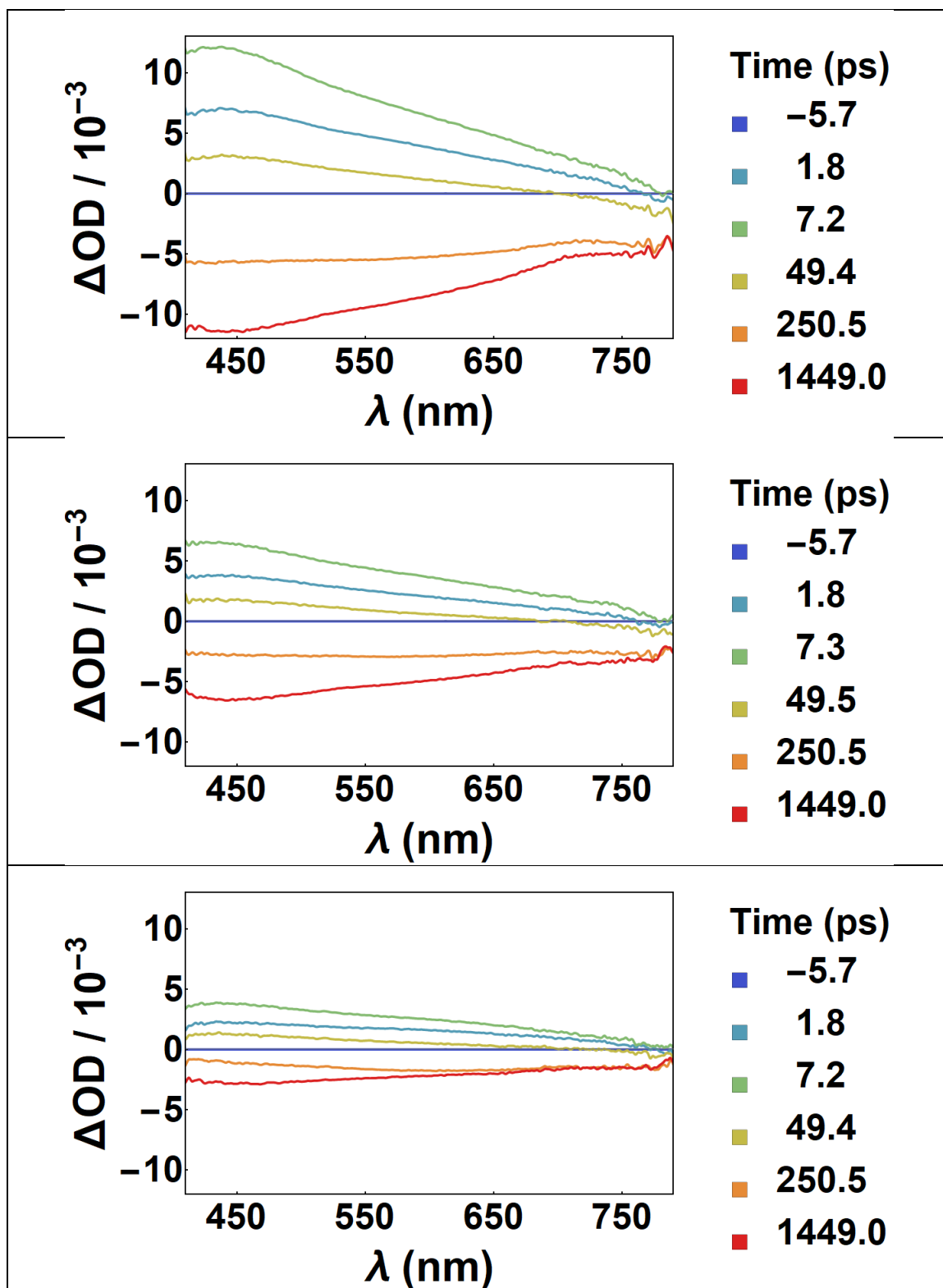
### Dynamics of Energy Transfer in Large Plasmonic Aluminum Nanoparticles



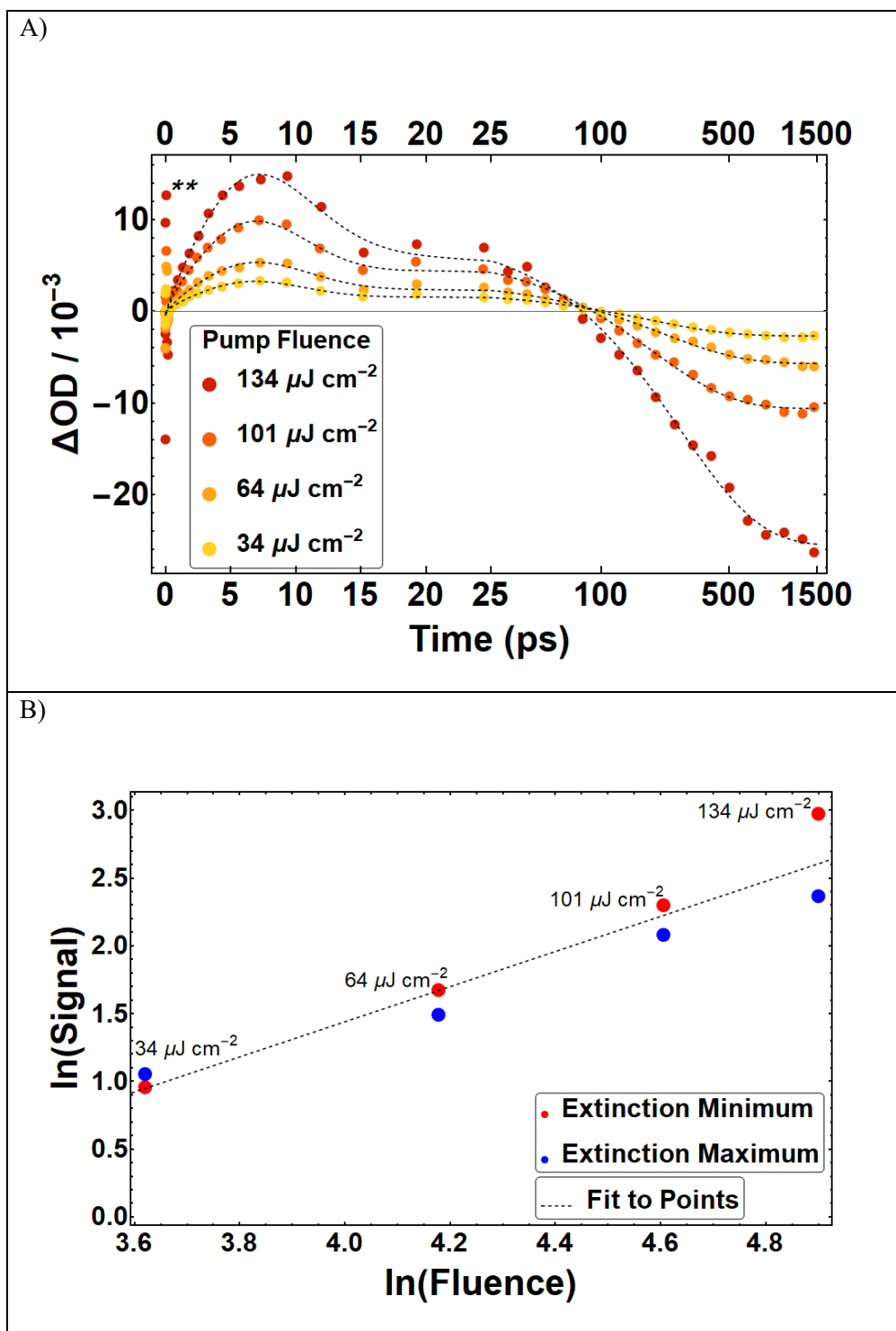
**Figure A1.1.** TEM images of aluminum NPs in (A), (B) and Figure 1A, were used to obtain the histogram (C) of the synthesized aluminum nanoparticle size. This analysis yields a size distribution with an average particle diameter of  $98 \pm 12$  nm. (D) FDTD-calculated spatial electromagnetic field profile for a 93 nm-diameter aluminum NP at the quadrupole resonance wavelength of 269 nm (color scale in a.u.).



**Figure A1.2.** TEM images of aluminum nanoparticles before (A) and after (B) prolonged exposure to a 400 nm excitation source show no observable changes in nanoparticle morphology.

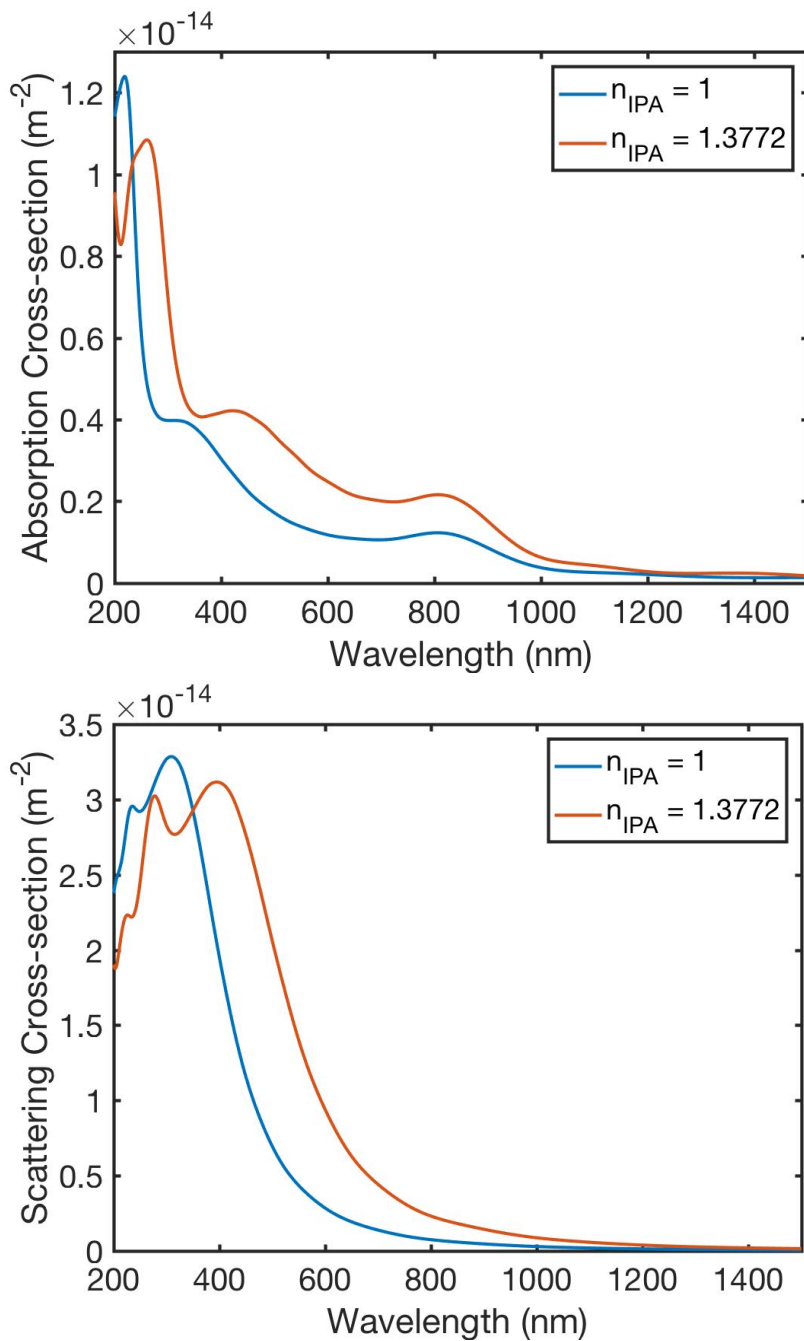


**Figure A1.3:** Fluence dependent transient absorption data conducted at  $101 \mu\text{J cm}^{-2}$  (Top),  $64 \mu\text{J cm}^{-2}$  (Middle), and  $34 \mu\text{J cm}^{-2}$  (Bottom). Similar spectral responses were observed at all fluences with intensity having linear dependence on pump fluence Shown in Figure A1.4B.



**Figure A1.4.** (A) Time-dependent traces (415-500 nm) at different pump fluences ranging from  $134 \mu\text{J cm}^{-2}$  (red) to  $34 \mu\text{J cm}^{-2}$  (yellow); fitting models described in the text are overlaid as dashed black lines. (B) Fluence dependence of max positive and negative extinction obtained in TAS measurements; fit reveals closely linear relationship between signal and fluence (slope = 1.29, see main text).





**Figure A1.5:** FDTD simulations of (top) absorption and (bottom) scattering cross sections of Al nanoparticle in IPA at different refractive indices (and corresponding dielectric constants). These comparisons reveal that the scattering contribution dominates absorption by an order of magnitude in most regions. Furthermore, local solvent heating (which generally induces reduction in refractive index and dielectric constants) can be expected to result in a net negative change in spectral scattering profile.

	$\tau_2$	$\tau_1$	$\tau_R$	$\phi$	$a_1$	$a_2$	$a_3$	$\gamma$	$c$
415- 500 nm	272 ps	0.91 ps	33 ps	4.25	1.95	34.0	15.4	0.09	-27.5
825- 900 nm	206 ps	0.3 ps	22 ps	3.5	2.12	5.03	1.51	0.09	-12.9
1000- 1125 nm	244 ps	3.5 ps	22 ps	4	0.3	4.05	1.38	0.09	-6.85

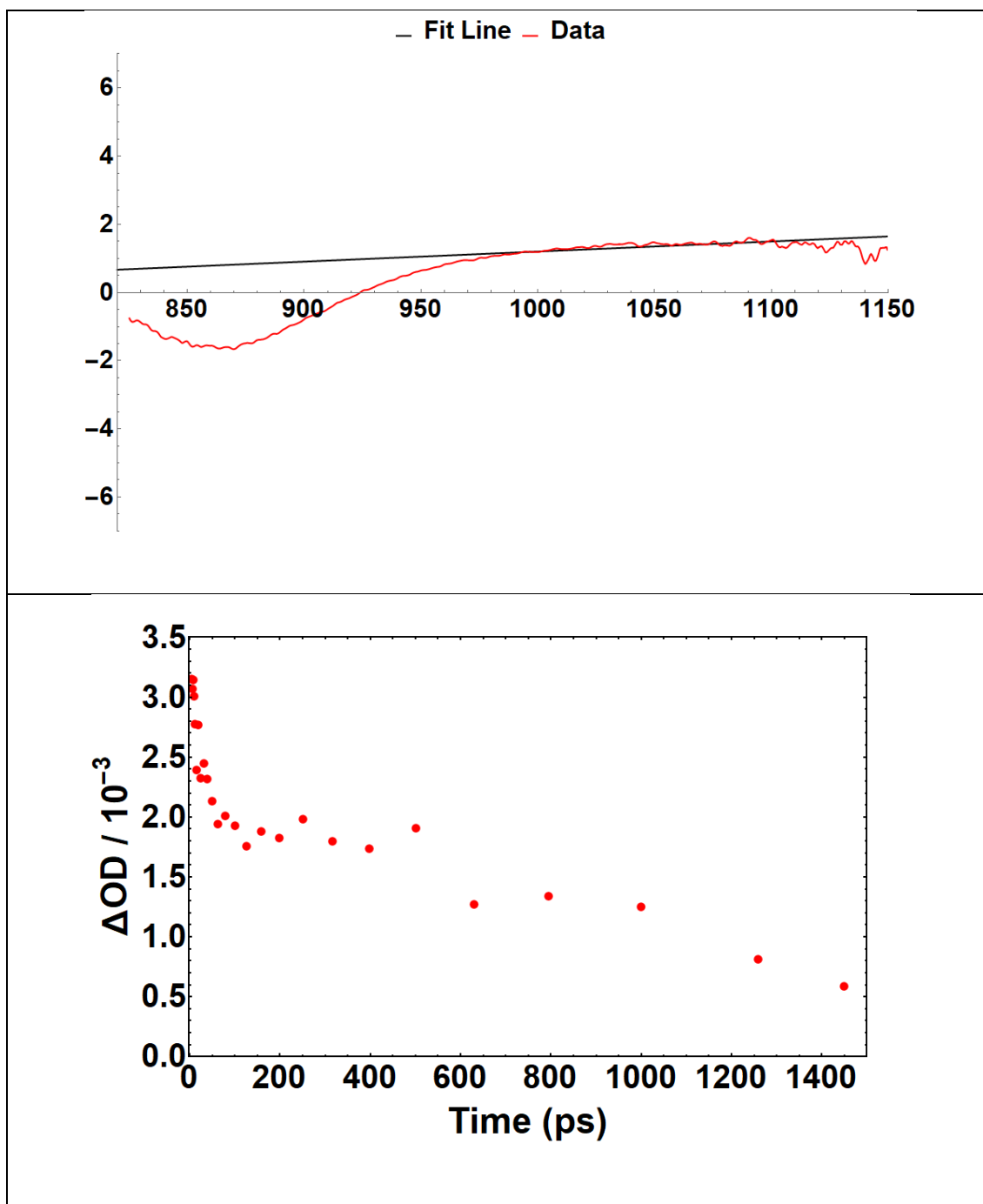
**Table A1.1:** Parameters for fits shown in Figure 3A in the text.

	$\tau_2$	$\tau_1$	$\tau_R$	$\varphi$	$a_1$	$a_2$	$a_3$	$\gamma$	$c$
$134 \mu\text{J cm}^{-2}$	272 ps	0.91 ps	33 ps	4.25	1.95	34.0	15.4	0.09	-27.5
$101 \mu\text{J cm}^{-2}$	191 ps	0.7 ps	25 ps	4	2.29	16.9	7.02	0.09	-12.9
$64 \mu\text{J cm}^{-2}$	216 ps	0.8 ps	27 ps	3.5	1.12	8.97	4.22	0.09	-6.85
$34 \mu\text{J cm}^{-2}$	183 ps	0.7 ps	25 ps	4	0.76	4.79	2.35	0.09	-3.46

**Table A1.2:** Parameters for fits shown in Figure A1.4A.

	$134 \mu\text{J cm}^{-2}$	$101 \mu\text{J cm}^{-2}$	$64 \mu\text{J cm}^{-2}$	$34 \mu\text{J cm}^{-2}$
$\tau_R$	14.0 ps	13.8 ps	13.7 ps	13.3 ps

**Table A1.3:** Oscillation period calculated from the truncated data sets 5-100 ps shown in Figure 3B in the text.



**Figure A1.6:** Crude isolation of interband bleach contribution. (Top) Linear trend lines were calculated for NIR spectra obtained at each delay using points at 1000 nm and 1100 nm. The value of the trend line at the wavelength where the bleach maximum occurred (869 nm) was subtracted from measured value at this wavelength. The difference is plotted in the bottom panel. Although this method is a crude approximation for the shape of the scattering contributions in this wavelength range, this analysis shows that the interband transition recovers roughly on the timescale of thermal energy transport.

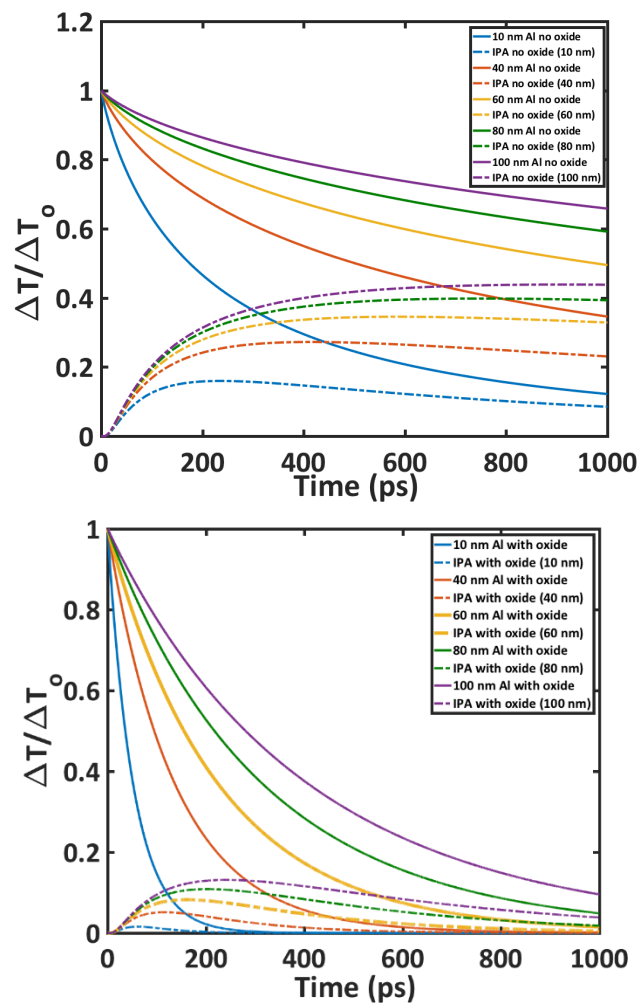
## Two Interface Model

Our model uses the following equations, adapted from the model in Reference 1,<sup>1</sup> for the temperature dynamics of the aluminum NP core ( $p$ ), the oxide shell ( $o$ ), and the solvent medium ( $m$ ): where  $\Delta T_0$  is the initial temperature increase of the nanostructure after optical pump excitation,  $c$  is the heat capacity per unit volume,  $G$  is the interface thermal conductance,  $\Lambda$  is the thermal conductivity,  $\kappa_1 = \frac{\Lambda_o}{c_o}$ ,  $\kappa_2 = \frac{\Lambda_m}{c_m}$ ,  $k_1 = \frac{3c_o}{c_p}$ ,  $k_2 = \frac{3c_m}{c_o}$ ,  $g_1 = \frac{G_1}{\Lambda_o}$ , and  $g_2 = G_2/\Lambda_m$ . The numerical subscript refers to the interface investigated ( $p$  - nanoparticle,  $o$  - oxide and  $m$  - medium), and interface 1 refers to the aluminum/aluminum oxide interface while interface 2 refers to the aluminum oxide/isopropanol.

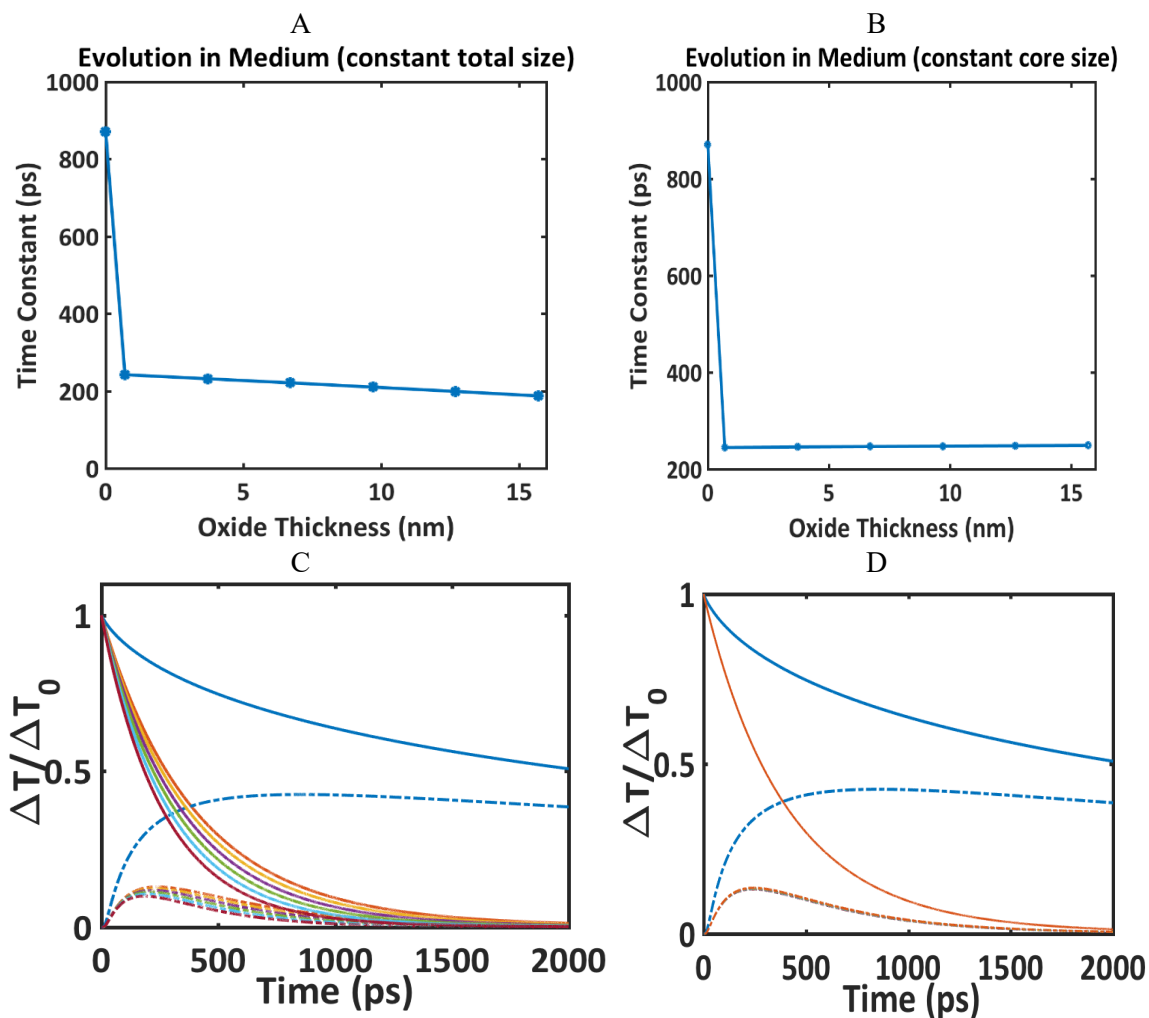
$$\Delta T_p(t) = \frac{2}{\pi} k_1 (R g_1)^2 \Delta T_0 \int_0^{+\infty} \frac{u^2 e^{-\kappa_1 u^2 t / R^2}}{(u^2(1 + R g_1) - k_1 R g_1)^2 + (u^3 - k_1 R g_1 u)^2} du$$

$$\Delta T_o(t) = \Delta T_0 \frac{2R}{\pi r_o} k_1 (R g_1)^2 \int_0^{+\infty} u^2 e^{-\kappa_1 u^2 t / R^2} \frac{u \left(1 - \frac{u^2}{k_1 R g_1}\right) \cos\left(\frac{u(r_o - R)}{R}\right) + \left(1 - \frac{u^2(1 + R g_1)}{k_1 R g_1}\right) \sin\left(\frac{u(r_o - R)}{R}\right)}{(u^2(1 + R g_1) - k_1 R g_1)^2 + (u^3 - k_1 R g_1 u)^2} du$$

$$\Delta T_m(t) = \Delta T_0 \frac{2r_o}{\pi r} k_2 (r_o g_2)^2 \frac{\Delta T_p}{\Delta T_0} \int_0^{+\infty} u^2 e^{-\kappa_2 u^2 t / r_o^2} \frac{u \left(1 - \frac{u^2}{k_2 r_o g_2}\right) \cos\left(\frac{u(r - r_o)}{r_o}\right) + \left(1 - \frac{u^2(1 + r_o g_2)}{k_2 r_o g_2}\right) \sin\left(\frac{u(r - r_o)}{r_o}\right)}{(u^2(1 + r_o g_2) - k_2 r_o g_2)^2 + (u^3 - k_2 r_o g_2 u)^2} du$$



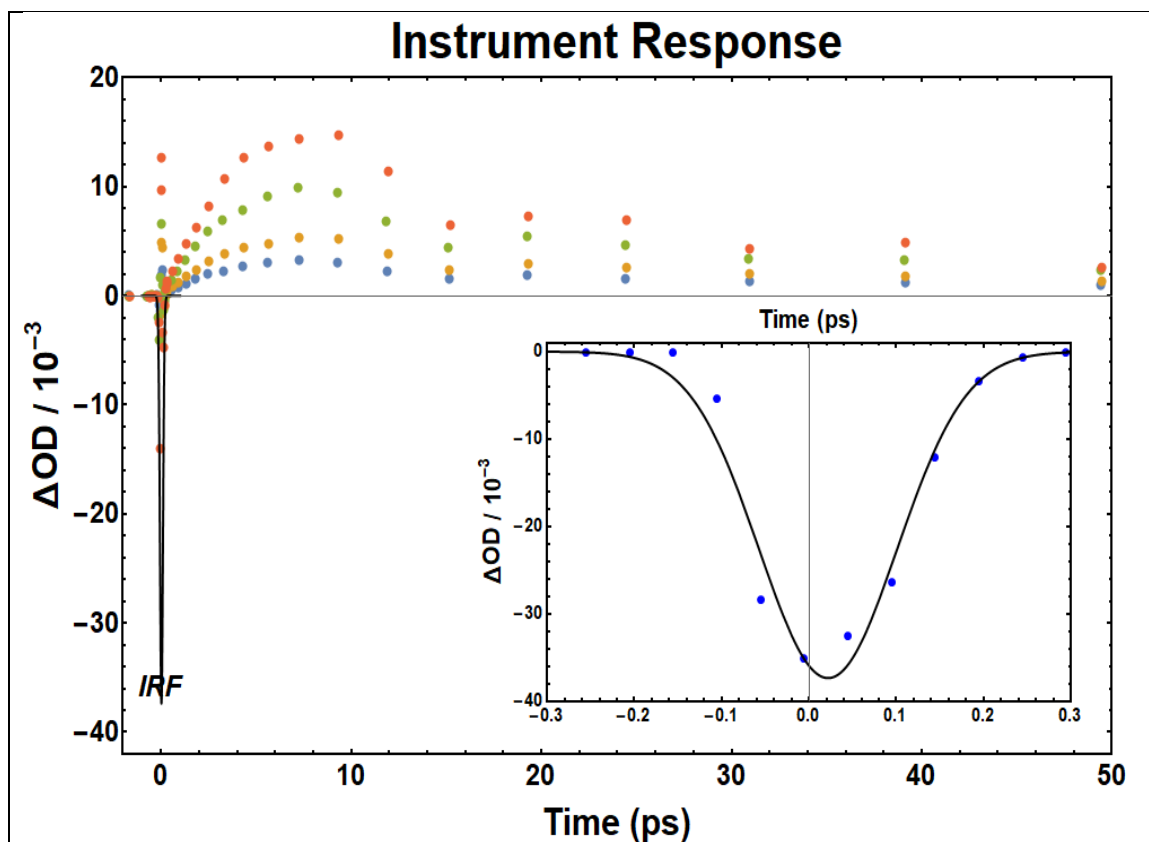
**Figure A1.7.** Normalized calculated temperature evolutions at the surface of varying sizes of aluminum nanoparticles (10 nm to 100 nm in diameter) and 3 nm into the surrounding medium: (Top) without the presence of an oxide layer, and (Bottom) with the presence of an oxide layer.



**Figure A1.8:** Temperature evolution time constant ( $1/e$ ) 3 nm into the solvent medium as a function of oxide thickness in the case of: (a) constant total nanoparticle size (the metal core diameter decreases with increasing oxide thickness) and (b) constant metal core size (the total size of the nanoparticle increases with increasing oxide thickness). Associated spectra for (a) and (b) are plotted in (c) and (d), respectively. Solid lines are for temperature evolution in the particles, and dashed lines are for temperature evolution in the solvent medium. The blue, orange, yellow, purple, green, cyan, and red spectra correspond to 0, 0.5 nm, 3.5 nm, 6.5 nm, 9.5 nm, 12.5 nm, and 15.5 nm oxide thicknesses respectively. These results indicate that changing the size of the aluminum metal core has a much greater influence on thermal energy transfer to the medium than changing the oxide thickness itself beyond a drastic decrease in the time constant after introduction of an oxide layer.

Although the thermal conductivities are different ( $205 \text{ Wm}^{-1}\text{K}^{-1}$  for Al vs.  $30 \text{ Wm}^{-1}\text{K}^{-1}$  for AlOx), the heat capacities of aluminum metal and aluminum oxide are fairly similar ( $2.43 \times 10^6 \text{ Jm}^{-1} \text{ K}^{-1}$  for Al vs.  $3.48 \times 10^6 \text{ Jm}^{-1} \text{ K}^{-1}$  for AlOx). The temperature evolution in the two-interface model depends more strongly on the interface properties than the size variation of the associated layers. In this case specifically, the oxide layer's primary role is to act as a heat sink in facilitating the heat transfer from the core material. As a result, the addition of an intermediary oxide layer drastically changes the temperature time constant in the solvent, and subsequent increases in the oxide layer thickness have a minimal effect when compared to the core aluminum thickness due to the much lower thermal conductivity of the aluminum oxide material (almost ten-fold lower than in the aluminum metal).





**Figure A1.9.** Solvent coherences during the pump-probe overlap were used to determine the instrument response function. The inset displays the calculated IRF Gaussian obtained by fitting the solvent coherences at time zero. The full width half max was calculated to be 262 fs.

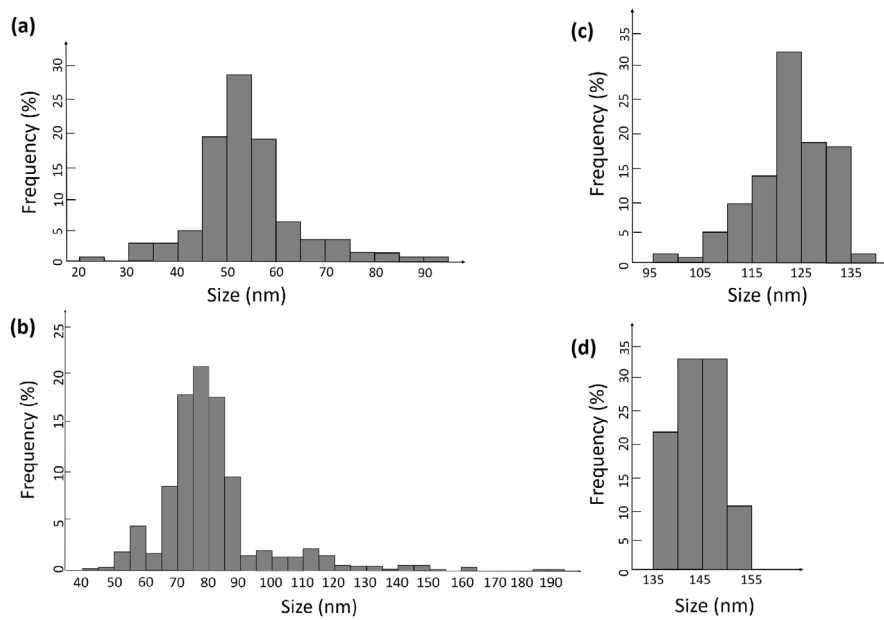
## REFERENCES

- (1) Stoll, T.; Maioli, P.; Crut, A.; Rodal-Cedeira, S.; Pastoriza-Santos, I.; Vallée, F.; Del Fatti, N. Time-Resolved Investigations of the Cooling Dynamics of Metal Nanoparticles: Impact of Environment. *J. Phys. Chem. C* 2015, 119 (22), 12757–12764

## Appendix II

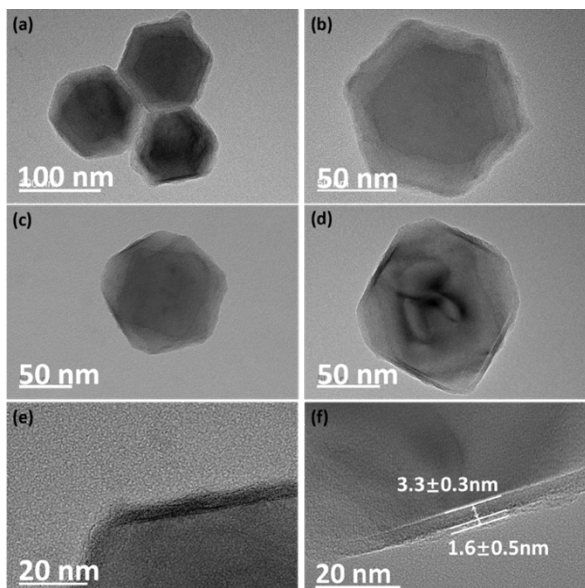
# Size and surface-dependent photoresponses of solution-processed aluminum nanoparticles

### A2.1 Particles size histograms

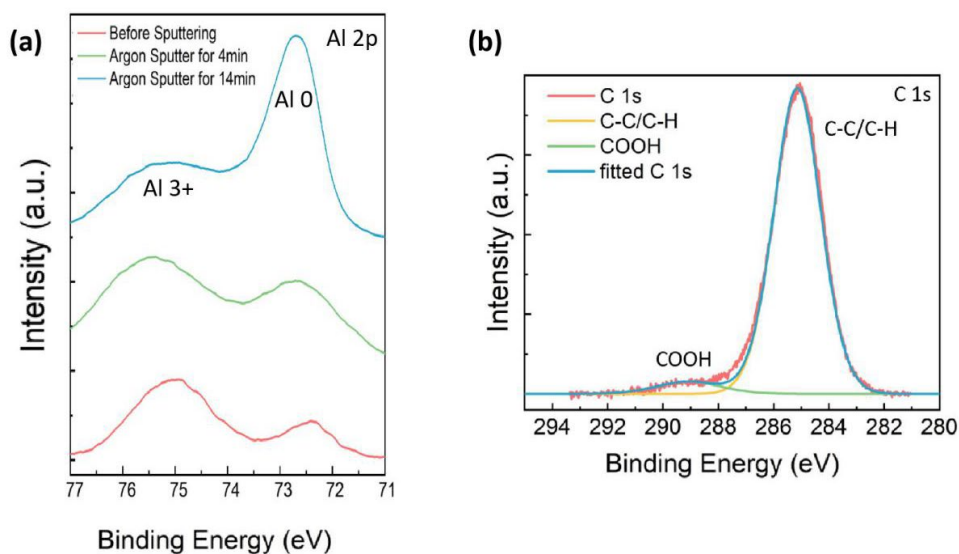


**Figure A2.1.** Histograms of aluminum nanoparticle (Al NP) diameters based on analysis of transmission electron microscope images of different NP ensembles. The particles have average diameters of (a)  $54 \pm 11$  nm, (b)  $85 \pm 21$  nm, (c)  $121 \pm 8.4$  nm, and (d)  $144 \pm 4.3$  nm (d).

## 2.) Surface characterization of Al nanoparticles



**Figure A2.2.** (a)-(f) Additional high resolution transmission electron microscopy (HRTEM) images of Al NPs. The oxide and organic ligand shells are visible in all images, although their thickness is obscured by faceting in (a)-(c). A thickness measurement is displayed in (f). Further characterization of oxide thickness and ligand surface coverage is provided below.



**Figure A2.3:** X-ray photoelectron spectroscopy (XPS) measurements of (a) the  $\text{Al}^0$  2p and  $\text{Al}^{3+}$  2p states before and after argon sputtering of the surface as indicated in the legend and (b) the C 1s region (red) of the Al NPs prior to sputtering and fits (yellow, green, blue) as indicated in the legend. The presence of the  $\text{Al}^{3+}$  2p peak in the XPS spectrum indicates the presence of an oxide shell on the Al NPs, and the thickness of the shell was determined to be  $3.1 \pm 10\%$  nm as described in the text below. The intensity ratio between the carboxylate-associated shoulder in (b) and the aliphatic C 1s feature is consistent with surface-bound oleate.

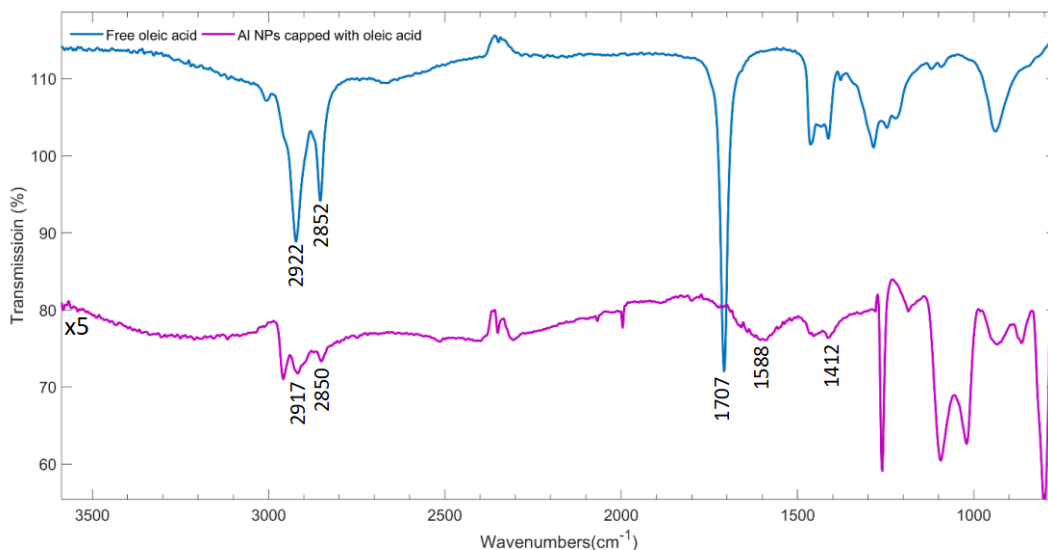
X-ray photoelectron spectroscopy (XPS) measurements were conducted on the Al NPs to investigate their composition (Figure A2.3). The Al 2p spectra shown in Figure A2.3 (a) clearly contains features associated with both Al ( $\text{Al}^0$ ) and Al oxide ( $\text{Al}^{3+}$ ) at binding energies of 72.7 eV and 75.1 eV,<sup>1,2</sup> respectively. Sputtering of the sample was conducted to confirm a metallic Al core existed. As the sputtering time increases, the relative intensity of the  $\text{Al}^0$  peak increases, corresponding to the removal of the oxide layer, the oxide layer thickness was calculated to be approximately  $3.1 \pm 10\%$  nm using established methods,<sup>3</sup> consistent with that estimated from the HRTEM measurement in Figure A2.2 (f).

XPS spectra collected in the C 1s region (Figure A2.3 (b)) of the Al NPs prior to sputtering reveal a small shoulder (next to a dominant peak) whose peak position (289 eV) is consistent with a carboxylate group.<sup>4</sup> The 5.3% intensity ratio between this shoulder and the dominant C 1s feature is consistent stoichiometrically with surface-bound oleic acid ( $\text{C}_{17}\text{H}_{33}\text{COOH}$ ) and the absence of any other organics at the surface.

We also utilized Fourier transform infrared (FTIR) spectroscopy and nuclear magnetic resonance ( $^1\text{H}$  NMR) measurements to further characterize the chemical state of the oleic acid/oleate ligand (i.e. bound or unbound carboxylate). FTIR spectra obtained with our oleate capped aluminum nanoparticles as well as free oleic acid are shown in Figure A2.4. The FTIR spectra indicate modifications to stretching vibrations consistent with the oleate being bound to the surface of the aluminum nanoparticles: the spectrum of the nanoparticles shows two peaks for the  $\text{CH}_2$  symmetric and asymmetric stretches of oleic acid that are slightly lower in energy relative to the free oleic acid stretches, as has been observed previously for surface bound oleate ligands.<sup>5,6</sup> More significantly, the strong

C=O stretching feature observed for free oleic acid at  $1707\text{ cm}^{-1}$  does not appear in spectra measured with our Al nanoparticles; instead, we observe two broad features at lower frequencies ( $1588$  and  $1412\text{ cm}^{-1}$ ) that correspond with the COO- symmetric and asymmetric stretches of oleate bound to the nanoparticle sample, as has been observed previously. Table A2.1 summarizes the frequencies for these features.

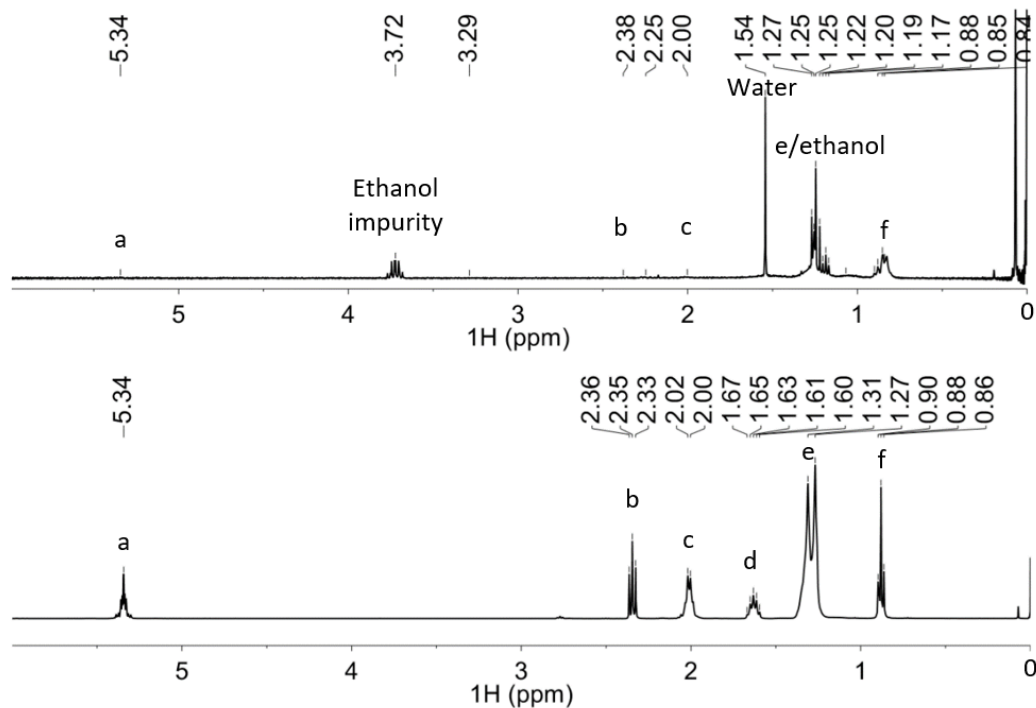
**Figure A2.4.** FTIR spectra of free oleic acid (blue) and oleic-acid-capped aluminum nanoparticles (pink) cast from IPA, multiplied by 5 and offset for comparison of vibrational features.



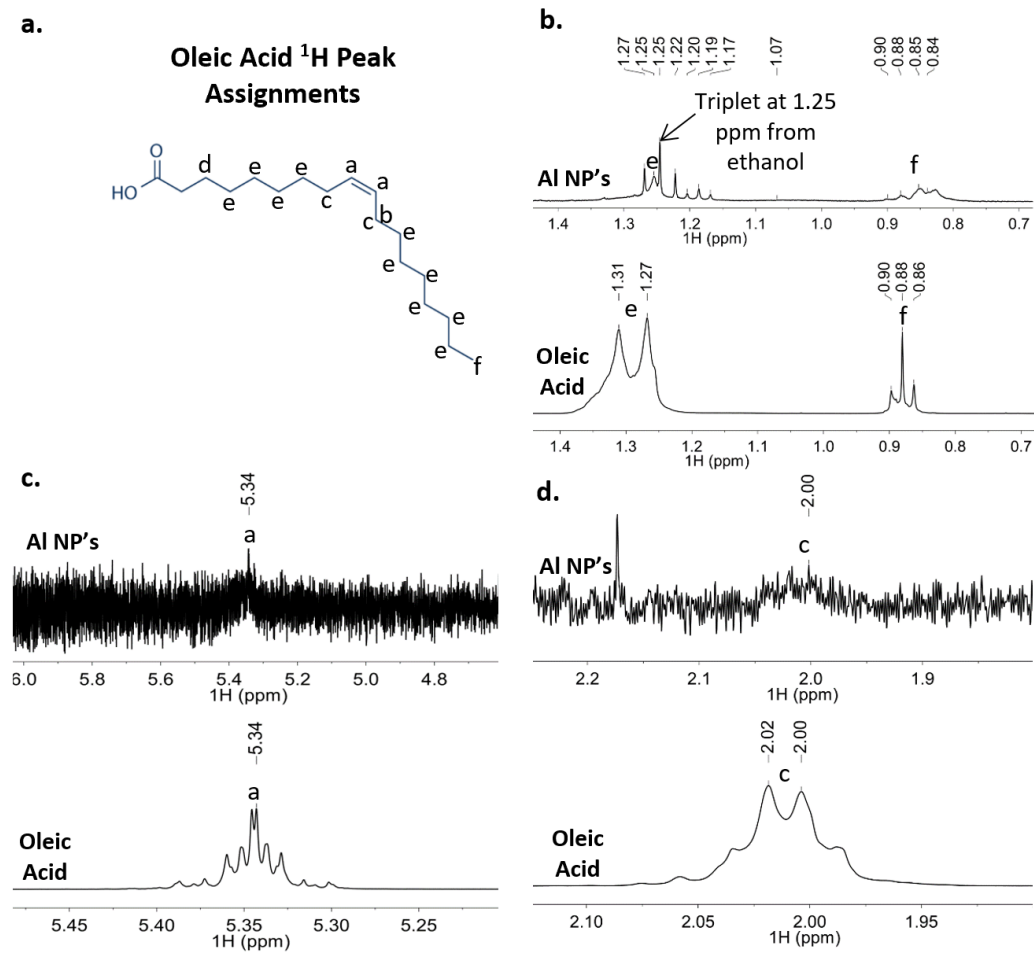
**Table A2.1.** Critical FTIR peak assignments.

	<b>CH<sub>2</sub> Symmetric Stretch</b>	<b>CH<sub>2</sub> Asymmetric Stretch</b>	<b>C=O stretch</b>	<b>COO- Symmetric Stretch</b>	<b>COO- Asymmetric Stretch</b>
<b>Oleic Acid</b>	$2852\text{ cm}^{-1}$	$2922\text{ cm}^{-1}$	$1707\text{ cm}^{-1}$	N/A	N/A
<b>Al NP</b>	$2850\text{ cm}^{-1}$	$2917\text{ cm}^{-1}$	N/A	$1412\text{ cm}^{-1}$	$1588\text{ cm}^{-1}$

$^1\text{H}$  NMR spectra were collected for ligand-capped aluminum nanoparticles and free oleic acid suspended/dissolved in deuterated chloroform. Full spectra for each sample are presented in Figure A2.5. Figure A2.6 (a) provides labels for hydrogen sites; Figures A2.6 (b-d) illustrate spectral differences for free vs. particle-bound oleate for specific hydrogen sites. The spectrum of the nanoparticles shows characteristic peaks of oleate bound to the surface of nanoparticles. The peaks for hydrogens “e” and “f” are the most resolved but are broadened and are shifted slightly downfield (Figure A2.6 (b)), a trend previously observed in the literature.<sup>7</sup> The peaks associated with hydrogens closer to the surface-bound carboxylate group (e.g. the “a” and “c” sites around the carbon double bond, Figures A2.6 (c-d)) are also broadened and either barely visible or not present due to their proximity to the nanoparticles which rotate slowly on the timescale of the measurement.<sup>8</sup> Table A2.2 summarizes the positions of features from NMR spectra.



**Figure A2.5.** Full  $^1\text{H}$  NMR of (a) aluminum nanoparticles capped with oleate ligand and (b) free oleic acid with peak assignments (c.f. Figure A2.6 (a)).



**Figure A2.6.** (a) Structure of oleic acid with  $^1\text{H}$  peak assignments and (b, c, d) highlighted regions of aluminum nanoparticle and free oleic acid  $^1\text{H}$  NMR spectra.

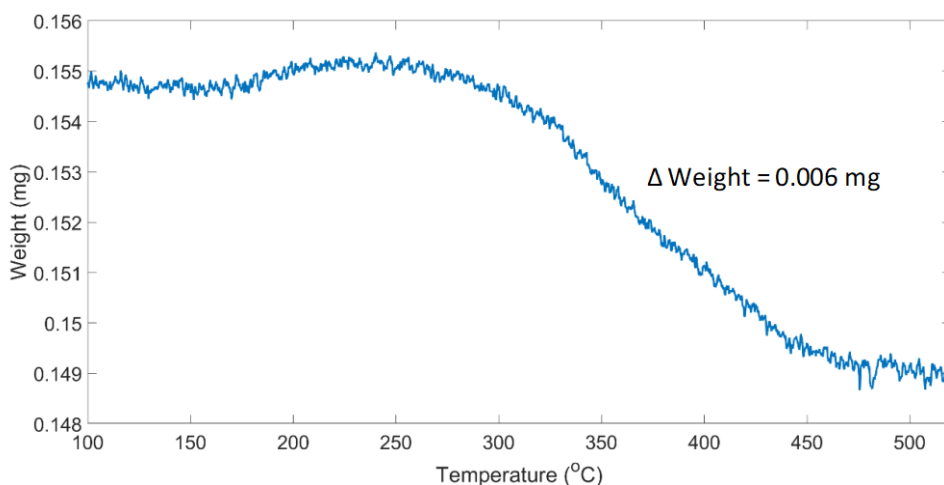


**Table A2.2.** <sup>1</sup>H NMR peak assignments.

Peak	H's	Oleic Acid		Al NP's	
		Center (ppm)	Type	Center (ppm)	Type
a	2	5.34	multiplet	5.34	broad singlet
b	2	2.35	triplet	2.38	broad singlet
c	4	2.01	multiplet	2.00	broad singlet
d	2	1.63	multiplet	n/a	n/a
e	20	1.29	multiplet	1.25	broad singlet
f	3	0.88	triplet	0.85	triplet

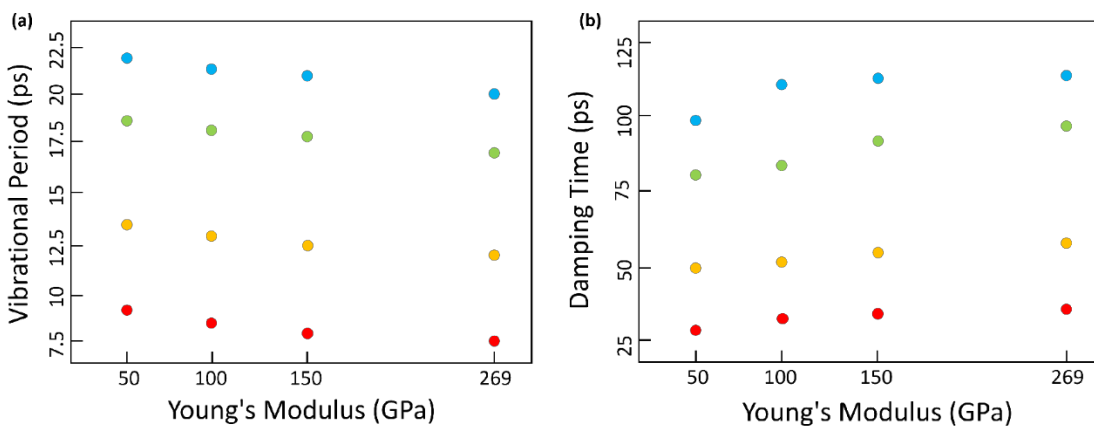
Finally, thermogravimetric analysis (TGA) was conducted using a TA Instruments SDT Q600 under flowing Ar at a heating rate of 5.0 °C min<sup>-1</sup> to estimate the surface coverage of oleate ligand on aluminum nanoparticles with an average diameter of 125 nm (3-nm oxide shell) suspended in isopropanol. An isothermal step was included at 82 °C for a duration of 30 min. We observe a significant weight loss between 80 and 100 °C due to the evaporation of the isopropanol solvent. Between 300 and 500 °C there is a 0.006 mg weight loss which we attribute to the decomposition of oleate bound to the surface of the nanoparticles, as shown in Figure A2.7. This result is consistent with previous TGA studies that show weight loss between 300 and 500 °C due to the decomposition of oleate strongly bound to the surface of Fe<sub>3</sub>O<sub>4</sub> MNPs.<sup>9,10</sup> Notably, weight loss from evaporation/decomposition of free oleic acid has been shown to occur at much lower temperatures, between 200 and 250 °C,<sup>9,10</sup> and is not seen here (consistent with FTIR and NMR analyses). Using the terminal mass of 0.149 mg, average particle diameter of 125 nm, oxide shell thickness of 3 nm, and the bulk densities of aluminum ( $\rho = 2.7 \text{ g/cm}^3$ ) and aluminum oxide ( $\rho = 3.2 \text{ g/cm}^3$ ) for the particle core and oxide shell, we calculated the total particle surface area for the sample. The surface area and mass loss from surface

bound oleate were used to determine the ligand number density on the surface. From this data we estimate that there are 5 oleate ligands per  $\text{nm}^2$  bound to the surface of our nanoparticles. This is consistent with results from previous studies of aluminum oxide particles with high densities of surfactant ligands (3.9-6.3 molecules/ $\text{nm}^2$ ).<sup>11</sup>



**Figure A2.7.** Thermogravimetric analysis (TGA) of oleate bound to Al nanoparticle surfaces used to determine surface coverage of  $\sim 5$  oleate ligands per  $\text{nm}^2$ . See text for details.

### 3.) Vibrational period and dephasing timescale with simulated surface properties



**Figure A2.8.** (a) Vibrational periods and (b) damping times calculated using finite element methods for single Al NPs with diameters of 54 nm (red), 85 nm (yellow), 121 nm (green), and 144 nm (blue) as a

function of the Young's modulus of a 4 nm oxide shell layer which is varied between 50 GPa and 269 GPa.

#### 4.) Fitting parameter errors

**Table A2.3.** Standard errors associated with each fitting timescale. ( $T_1$  was fixed to simulated value as described in the text due to sample polydispersity for 85-nm particles.)

	$\tau_p$	$\tau_r$	$\tau_d$	$T_1$
54 nm	0.38	0.69	6.71	0.91
85 nm	0.29	0.20	13.5	-
121 nm	0.22	0.53	53.3	11.7
144 nm	0.23	0.53	37.6	20.0

## 5.) References

- (1) Sarapatka, T. J. Palladium-Induced Charge Transports with Palladium/Alumina/Aluminum Interface Formation. *J. Phys. Chem.* **1993**, *97*, 11274–11277.
- (2) Kim, Y.-C.; Park, H.-H.; Chun, J. S.; Lee, W.-J. Compositional and Structural Analysis of Aluminum Oxide Films Prepared by Plasma-Enhanced Chemical Vapor Deposition. *Thin Solid Films* **1994**, *237*, 57–65.
- (3) Alexander, M. R.; Thompson, G. E.; Zhou, X.; Beamson, G.; Fairley, N. Quantification of Oxide Film Thickness at the Surface of Aluminium Using XPS. *Surf. Interface Anal.* **2002**, *34*, 485–489.
- (4) Popat, K.C., Sharma, S. and Desai, T.A. Quantitative XPS analysis of PEG-modified silicon surfaces. *J. Phys. Chem. B.* **2004**, *108*, 5185-5188.
- (5) Premaratne, W. a. P. J.; Priyadarshana, W. M. G. I.; Gunawardena, S. H. P.; Alwis, A. A. P. D. Synthesis of Nanosilica from Paddy Husk Ash and Their Surface Functionalization. *Journal of Science of the University of Kelaniya Sri Lanka* **2014**, *8*, 33–48.
- (6) Cai, J.; Miao, Y. Q.; Yu, B. Z.; Ma, P.; Li, L.; Fan, H. M. Large-Scale, Facile Transfer of Oleic Acid-Stabilized Iron Oxide Nanoparticles to the Aqueous Phase for Biological Applications. *Langmuir* **2017**, *33*, 1662–1669.
- (7) Zemke, J. M.; Franz, J. A Biphasic Ligand Exchange Reaction on CdSe Nanoparticles: Introducing Undergraduates to Functionalizing Nanoparticles for Solar Cells. *J. Chem. Educ.* **2016**, *93*, 747–752. <https://doi.org/10.1021/acs.jchemed.5b00847>.
- (8) Moody, I. S.; Stonas, A. R.; Lonergan, M. C. PbS Nanocrystals Functionalized with a Short-Chain, Ionic, Dithiol Ligand. *J. Phys. Chem. C* **2008**, *112*, 19383–19389.
- (9) Lai, C. W.; Low, F. W.; Tai, M. F.; Abdul Hamid, S. B. Iron Oxide Nanoparticles Decorated Oleic Acid for High Colloidal Stability. *Adv. Polym. Tech.* **2018**, *37*, 1712–1721.
- (10) Ayyappan, S.; Gnanaprakash, G.; Panneerselvam, G.; Antony, M. P.; Philip, J. Effect of Surfactant Monolayer on Reduction of Fe<sub>3</sub>O<sub>4</sub> Nanoparticles under Vacuum. *J. Phys. Chem. C* **2008**, *112*, 18376–18383.
- (11) Portilla, L.; Halik, M. Smoothly Tunable Surface Properties of Aluminum Oxide Core–Shell Nanoparticles By A Mixed-Ligand Approach. *ACS Appl. Mater. Interfaces* **2014**, *6*, 5977–5982.

# Appendix III

## Curriculum Vitae

### **Kenneth James Smith**

105 W. 39<sup>th</sup> St. Apt 408, Baltimore, MD 21210 • (415) 200-6674  
[kensmith415@gmail.com](mailto:kensmith415@gmail.com) • <https://orcid.org/0000-0001-5497-7069>

### **Professional Summary**

Ph.D. Candidate at Johns Hopkins University with 6 years' experience in ultrafast spectroscopy studying relaxation and energy transfer in plasmonic materials. In addition to my work at JHU, I have previously worked extensively with time of flight photoionization mass spectrometry (TOF-MS) at the advanced light source (ALS) as well as high resolution magic angle spinning (HRMAS) NMR at USCF. Combined 10+ years of research experience.

### **Education**

<b>Ph.D. Chemistry</b> , Johns Hopkins University, Baltimore MD Advisor: Art Bragg	2013 – 2020
<b>M.S. Chemistry</b> , University of San Francisco, San Francisco CA Advisor: Giovanni Meloni	2011 – 2013
<b>B.S. Chemistry</b> , University of California Davis, Davis CA	2004 – 2008

### **Skills**

- Technical expertise and understanding of:
  - Steady state and time resolved spectroscopy techniques, fluorescence, photoionization mass spectrometry, NMR, MRI/MRS, electronic structure calculations
- Technical expertise and understanding of:
  - Ultrafast laser systems/equipment: laser oscillator, non-linear optics, regenerative amplifier, optical parametric amplifier (OPA), BBO doubling crystals, general maintenance/re-optimization of optical beam paths within oscillator and amplifier as well as optical configurations on the laser table
  - Ultra-high vacuum gas phase equipment and experiments
  - Air free sample preparatory techniques like freeze pump thaw and the use of a Schlenk line
- High level of proficiency with many software packages:
  - Mathematica, Igor Pro, Gaussian, Matlab, LabView, Microsoft Office, ChemDraw
- Demonstrated experience with complex data analysis and modeling
- Experience in chemical synthesis
- High level of written and oral communication skills
- Experienced in working collaboratively with diverse groups of people

### **Research Experience**

**Johns Hopkins University**, Department of Chemistry

2013 – Present

**Ph.D Candidate**

- Oversaw new research project in the Bragg lab interrogating the photophysics of plasmonic nanoparticles (NP's) for possible application in plasmon-enhanced photocatalysis. An emphasis was placed on studying aluminum nanoparticles, which are of considerable interest given Al's relative earth abundance compared to noble metals.
- Developed experimental protocols and conducted various ultrafast spectroscopic measurements to study nanoparticle photo physics in solutions and films. Extensive wavelength and fluence dependent studies were conducted on aluminum NP's, gold NP's, Au@TiO<sub>2</sub> core shell NP's, and Au-TiO<sub>2</sub> thin films in order to probe fundamental relaxation and energy transfer dynamics.
- Processed and analyzed large sets of experimental data using custom written scripts/protocols in the programming platforms Mathematica and Matlab that utilized non-linear least squares fitting routines to accurately fit data to kinetic models. Various methods were used to find proper kinetic models such as global analysis, principle component analysis and singular value decomposition; statistical analysis was used to determine proper error values where possible.
- Collaborated with Susanna Thon's engineering lab in synthesizing, conducting experiments, and writing manuscripts on the photophysics of aluminum NP's
- Synthesized Au NP's, Au@TiO<sub>2</sub> core shell NP's and a viologen derived electron accepting ligand

**University of San Francisco**, Department of Chemistry

2011 – 2013

**M.S. Graduate Student**

- Studied radical combustion chemistry of potential biofuels through the use of time of flight photoionization mass spectrometry (TOF-MS) at the advanced light source (ALS), in conjunction with Sandia National Labs
  - Primary project focused on the interrogation of the potential biofuel 2,5-dimethylfuran with the CH<sup>\*</sup>[X<sup>2</sup>II] (methylidyne) radical which is common in many combustion reactions. Used multiplexed photoionization mass spectrometry coupled to tunable VUV synchrotron radiation at the ALS chemical kinetics beamline.
- Compiled and analyzed large data sets in Igor Pro where photoionization efficiency and kinetic plots were created to identify stable/radical and primary/secondary products of the reaction to elucidate reaction pathways
- Extensive *ab initio* electronic structure calculations were conducted using Gaussian 09 and Gaussview 5.0 on reaction products and intermediates in order to find enthalpically favored pathways as well as simulate PIE curves
- Used Photoelectron Photoion Coincidence Spectroscopy (PEPICO) to characterize the ionization behavior of 2,5-dimethylfuran (DMF)

**University of California San Francisco**, Department of Radiology

2008 – 2011

**Staff Research Associate II**

- Study coordinator and lead researcher for a \$1.2 million 5-year NIH RO1 clinical imaging grant using a combination of magnetic resonance imaging, magnetic resonance spectroscopy (MRI/MRS) and High-Resolution Magic Angle Spinning (HRMAS) NMR to study the cellular metabolism in low grade malignant astrocytoma and oligodendroglioma brain tumors.
- Responsible for patient accrual, organizing and preparing NIH progress reports, maintaining accurate participation and billing summaries, training new hires or

interns, collecting biopsies/samples during surgery, as well as administering the clinical pre-surgical MRI/MRS with subsequent analysis of *ex vivo/in vivo* and immunohistochemistry data

- Acted as lab manager of BSL2 Tissue Laboratory, maintaining inventory, safety inspections, ordering supplies, coordinating weekly user meetings and resolving any possible safety or OSHA violations
- Spearheaded development of pre-clinical MRI/MRS/HRMAS protocols, standardized experimental procedures and data analysis for a new project grant awarded after publication of the results from the primary RO1 grant

University of California Davis, Center for Health and the Environment (CHE)  
– 2008

2006

### Student Researcher II

- Developed protocol to quantify naphthalene-glutathione conjugate isomers using HPLC, UV-Vis and fluorescence for use as a standard to determine their concentration in mouse lungs subjected to smoke inhalation

### Publications

- Smith, K.; Cheng, Y.; Arinze, E.; Thon, S.; Bragg, A.; Size-dependent Photoresponses of Solution-Processed Aluminum Nanoparticles. (*Submitted to ACS Photonics*)
- Magnanelli, T.; Smith, K.; Yu, W.; Bragg, A.; Energy Transfer in Nonplanar Thiophene-Methanoannulene Polymers. (*Planned for JPCC*)
- Carrasco, E.; Smith, K.; Meloni, G.\* Synchrotron Photoionization Study of Furan and 2-Methylfuran Reactions with Methylidyne Radical (CH) at 298K. *J. Phys. Chem. A.*, **2018**, 122, 1, 280-291.
- Smith, K.; Cheng, Y.; Arinze, E.; Kim, N.; Bragg, A.\*; Thon, S.\*; Dynamics of Energy Transfer in Large Plasmonic Aluminum Nanoparticles. *ACS Photonics*, **2018** 5 (3), 805-813.
- Smith, K.; Meloni, G.\*; Influence of Various Functional Groups on the Relative Stability of Alkylperoxy triplet cations: A Theoretical Study. *Chem. Phys. Let.* **2015**, 631-632, 34-41.
- Reed, G.; von Morze, C.; Bok, R.; Koelsch, B.; Van Criekinge, M.; Smith, K.; Shang, H.; Larson, P.; Kurhanewicz, J.\* High Resolution <sup>13</sup>C MRI with Hyperpolarized Urea: In Vivo T<sub>2</sub> Mapping and <sup>15</sup>N Labeling Effects. *IEEE Transactions on Medical Imaging*, **2014**, 33, 362-371
- Reed, G.; von Morze, C.; Bok, R.; Koelsch, B.; Smith, K.; van Criekinge, M.; Larson, P.; Kurhanewicz, J.\*; Vigneron, D.\* WE-C-116-02: High Resolution C-13 MRI with Hyperpolarized [<sup>13</sup>C <sup>15</sup>N] Urea. *Med. Phys.* **2013**, 40, 484-484.
- Khayal, I.; Vandenberg, S.; Smith, K.; Cloyd, C.; Chang, S.; Chang, S.; Nelson, S.\*; McKnight, T.\* MRI Apparent Diffusion Coefficient Reflects Histopathologic Subtype, Axonal Disruption, and Tumor Fraction in Diffuse-type Grade II Gliomas. *Neuro Oncology*. **2011**, **13**(11), 1192-1201.
- McKnight, T.\*; Smith K.; Chu P.; Chiu, K.; Cloyd, C.; Chang, S.; Phillips, J.; Berger, M.\* Choline Metabolism, Proliferation, and Angiogenesis in Non-Enhancing Grades 2 and 3 Astrocytoma. *JMRI*. **2011**, **33**(4), 808-816.

### Teaching Experience

- **Lab TA:** Received high marks on TA evaluations from students and professors
  - General chemistry lab TA for 3 years (2 years at USF and 1 year at JHU)
  - Physical chemistry lab TA for 2 years at JHU